UNIVERSITY OF SOUTHAMPTON

Faculty of Engineering, Science and Mathematics

Optoelectronics Research Centre

Precise Intensity and Phase Characterisation of Optical Telecommunication Signals

A thesis submitted for the degree of Doctor of Philosophy

by

Michaël Alberic Freddy Roelens

July 2006

UNIVERSITY OF SOUTHAMPTON

ABSTRACT

FACULTY OF ENGINEERING, SCIENCE AND MATHEMATICS
OPTOELECTRONICS RESEARCH CENTRE

Doctor of Philosophy

Precise Intensity and Phase Characterisation of Optical Telecommunication Signals

by Michaël Alberic Freddy Roelens

In this thesis, the accurate characterisation of a range of high speed optical telecommunication signals is presented. The main technique used to determine both the intensity and the phase profiles of these signals is based on spectrograms, and various developments and extensions of this method are presented.

Firstly, the linear spectrogram method, in which the spectrogram is created by gating the optical signal with an electro-absorption modulator, is experimentally compared to the more prevalent technique of frequency resolved optical gating (FROG). The detailed comparison for three different pulses shows that the linear spectrogram method is advantageous for telecommunication signals.

Pulses from a gain switched laser diode are accurately characterised, and the linear spectrograms reveal new insight into how the pulse develops. It is found that the wavelength of the optical seed signal, from which the pulse develops, has a strong impact on the pulse quality, and its exact influence is illustrated. The complete information gained from the spectrograms makes it possible to design a matched fibre Bragg grating to improve the quality of pulses generated by gain switching a 1550nm semiconductor laser diode. The spectrogram technique is also adapted to and used for characterising pulses in the 1060nm region.

For the first time, the quality of fibre Bragg gratings for use in pulse shaping applications is directly assessed by spectrographically measuring the waveforms they reflect. Both parabolic and rectangular shaped pulses are investigated, as well as various phase encoding gratings for use in optical code division multiple access systems. By further investigating the pulses reflected from temperature tunable fibre Bragg gratings, we have measured the spatial refractive index distribution that can be induced in such gratings.

The linear spectrogram technique is also applied to high capacity transmission systems. We show that it can be extended to characterise several wavelength division multiplexed channels simultaneously. The measured intensity profiles after transmission in a recirculating loop shows that we can monitor dispersive and nonlinear impairments on the pulses.

Finally, data modulated pulses in a 40 Gbit/s system are characterised before and after propagation in an installed fibre link, and excellent agreement is found between the information retrieved from the spectrogram method, independent intensity measurements and theoretical expectations.

Hit kom jag,
vet ej varför,
stum och blind,
ej varifrån,
som regnet mot min kind.

Och jag försvinner,
vet ej varthän,
som vid mitt tält en öknens virvelvind.

Into this Universe, and why not knowing,
Nor whence, like Water willy-nilly flowing:
And out of it, as Wind along the Waste,
I know not whither, willy-nilly blowing.

–from Omar Khayyam, Edward FitzGerald

Contents

List of Figures

Declaration of Authorship

I, Michaël Alberic Freddy Roelens, declare that the thesis entitled *Precise Intensity and Phase Characterisation of Optical Telecommunication Signals* and the work presented in it are my own. I confirm that:

- this work was done wholly while in candidature for a research degree at this University;
- where any part of this thesis has previously been submitted for a degree or any other qualification at this University or any other institution, this has been clearly stated;
- where I have consulted the published work of others, this is always clearly attributed;
- where I have quoted from the work of others, the source is always given. With the exception of such quotations, this thesis is entirely my own work;
- I have acknowledged all main sources of help;
- where the thesis is based on work done by myself jointly with others, I have made clear exactly what was done by others and what I have contributed myself;
- parts of this work have been published, see *List of Publications*.

Michaël A. F. Roelens

June 2006

To the loving memory of my father

Acknowledgements

It has been good. Definitely. I have enjoyed it, and very much so. Not just my Ph.D., and my stay in Southampton, but so many other things too. It is probably impossible to sum up all that have made the whole experience so much more than worthwhile, but I would like to take the opportunity to thank a few people to whom I feel especially indebted.

Top scorer, without doubt, is my supervisor, Professor David Richardson. Every time I knocked on his door for a brief update, or a bit of advice, he found the time to give me very useful feedback. I feel very fortunate to have been guided and encouraged by such a great person.

I have also enjoyed working with Dr. Periklis Petropoulos. I am grateful especially the great support in the whole e-Photon/ONe project, and the valuable discussions from time to time. Also a big thank you to Dr. Benn Thomsen, who has introduced me to so many different experiments during the start of my Ph.D., that I have been able to work pretty much independently ever since he gave up commuting every day down to Southampton.

I have always found it very rewarding to work with Marco Forzati and Dr. Anders Berntson, from Acreo AB, and the few times I had the possibility to collaborate with them during my Ph.D. have certainly confirmed this. I am very grateful for their support and confidence in me on these occasions.

I am thankful as well for the many gratings Dr. Morten Ibsen has provided us with, and the fruitful discussions. I feel privileged to have worked with Taichi Kogure, especially for the development of the Q-factor measurement system. And even though the collaboration with Dr. Christophe Kazmierski, from Alcatel-Thales, was rather brief, I have learned a lot, so I would like to thank him for this.

It has been great to have had Dr. Anoma McCoy, Paulo Almeida, Francesca Parmigiani and Chun Tian as colleagues in the lab. The many conversations, practical help, their interest in all sorts of pulse shapes, and above all friendliness are much more than what I could have hoped for. I have really enjoyed getting to know you as colleagues and friends. It has been a pleasure as well to get to know the next generation in our lab, Trina Ng and Lionel Provost. It feels good to know that a few things I have done during my Ph.D. might actually be of direct use to them. I am also grateful for the brief collaborations with Khu Tri Vu, Pascal Dupriez Christophe Codemard and Zhaowei Zhang.

I would like to thank Mrs. Eveline Smith, for all the administrative work, and some 'native language' conversations. Simon Butler and Timothy McIntyre have also helped a lot with the neat construction of many pieces of equipment.

It has been great to be able to work in such a diverse and exciting environment as the ORC. Many friends and people I got to know here have made my stay in Southampton more pleasant. A special thanks to fellow paragliding pilots, especially Michael Yarrow, and the people from the Athletic Union for supporting this crazy, little paragliding club.

Finally, the ever lasting trust and confidence from my mother and brothers, Laurens and Frederik, have been of immense value during my whole Ph.D. I really appreciate their support throughout this adventure.

– Michaël

Abbreviations

APRZ alternating phase return to zero

ASE amplification of spontaneous emission

AWG arrayed waveguide grating

BER bit error rate

CDMA code division multiple access

CSRZ carrier suppressed return to zero

CW continuous wave

DCF dispersion compensating fibre

DFB distributed feedback

DS direct-sequence

EAM electro-absorption modulator

EDFA erbium doped fibre amplifier

ER extinction ratio

FBG fibre Bragg grating

FROG frequency resolved optical gating

FWHM full width at half maximum

FWM four wave mixing

GRENOUILLE GRating-Eliminated No-nonsense Observation of Ultrashort Incident Laser Light E-fields

GS gain switched

MZM Mach-Zehnder modulator

NLSE nonlinear Schrödinger equation

NRZ non-return to zero

OCDMA optical code division multiple access

OSA optical spectrum analyser

PCGP principal components generalised projection

PM polarisation maintaining

PRBS pseudo random bit sequence

RZ return to zero

SHG second harmonic generation

SSMF standard single mode fibre

SMSR side mode suppression ratio

SPIDER Spectral phase interferometry for direct electric-field reconstruction

SSFBG superstructured fibre Bragg grating

TDM time domain multiplexing

WDM wavelength division multiplexing

Chapter 1

Introduction

At every conference on optical communications, there seems to be at least one talk with that typical graph showing the exponentially exploding demand for bandwidth [1, 2, 3]. Whilst the future evolution of these curves will probably always be a point of discussion, it is clear that the total signal capacity of a standard single mode fibre has not yet been completely unlocked. At the same time though, there is an increasing interest in trying to utilise the bandwidth provided by the fibre more flexibly, as the point where the optical signal is converted into an electrical one is moving ever closer to the end user.

It leaves no doubt that the requirements on the quality of the optical signals used for reaching these ultra-high capacity networks are progressively more stringent. Whilst electronic compensation techniques and forward error correction methods can relieve some of these requirements – often in a cheaper way than what is possible with only optical processing – it is necessary to fully understand the optical signal and how it is affected through propagation over the fibre in order to make the most of the available capacity.

New ways of modulating and encoding the data onto the optical carrier signals have meant a more thorough investigation into the possibilities offered by combining phase and intensity modulation. At the same time, research in the complete characterisation of the signals has surged. Simple electronic intensity measurements are no longer sufficient to assess the properties of current optical telecommunications signals.

Frequency-resolved optical gating (FROG) is arguably the most renowned complete characterisation technique that has slowly moved into the field of optical communications [4]. However, it has its drawbacks, as will be indicated further on in this thesis. Whilst my initial Ph.D. work involved the implementation of ultra-high bit rate systems with speeds of up to 160 $Gbit/s$, the focus gradually shifted more to the characterisation of the optical signals used, to find out what exactly was limiting the performance of the system. Initial SHG-FROG measurements proved to yield inadequate information, and we adopted a newly developed implementation that is based on components specifically made for telecommunications purposes.

The results of the linear spectrograms were very promising, and the technique has now been applied to many of the different research topics in our department. Also through external collaborations, I have been able to further explore and extend the applicability of this method. The following chapters in this thesis are grouping experiments where, based on results of the rigorous characterisation of optical signals, new insight was gained in the respective areas of optical communications.

Outline

Chapter 2 contains the general background for the characterisation work in this thesis. It starts off with an introduction to the various possibilities to completely characterise optical signals: tomographic, interferometric and spectrographic techniques, applied to the field of optical telecommunications. Two specific spectrographic methods are explained more in detail: SHG-FROG and linear spectrograms with an electro-absorption modulator. The data acquired from these methods, called spectrograms, need to be 'deconvolved' in order to reconstruct the intensity and phase profiles of the signals under test. The iterative algorithm is described together with some mathematical additions that can improve the quality of the measured spectrogram. For the respective pieces of Matlab code, the reader is referred to Appendix B. The chapter concludes with an experimental comparison between the two spectrographic methods applied to three different pulses.

In Chapter 3, two interesting sources for short pulses are investigated. The first one is a gain switched semiconductor laser diode, in the C-band. A series of

spectrogram measurements not only reveals the optimal settings for driving the laser diode, but also generates new insight in how the pulse develops. The chirp, that is accurately measured with the spectrograms, can be compensated with a specifically designed fibre Bragg grating, and the theoretical results predict a clean and stable 5 *ps* pulse, generated in a very compact way. Recent measurements with a diode at an operating wavelength of 1060 *nm* are also presented. These measurements were performed with a setup adapted to this operating wavelength. Pulses carved with an electro-absorption modulator are presented next, and are particularly interesting because it provides additional information of the gating function in the frequently used spectrographic method.

Chapter 4 explains a few specific pulse shaping experiments, based on advanced fibre Bragg gratings. Another pulse source, the fibre ring laser, is introduced here, because of its broad bandwidth, and particular suitability for the generation of rectangular and parabolic shaped pulses. The latter two are useful for example in pulse retiming experiments. The fine features of these pulses, as characterised here, are important for the performance of these systems.

Secondly, some of the waveforms used in optical code division multiple access (OCDMA) experiments are presented. To generate these rather exotic-looking waveforms with specific phase information, we also rely on fibre Bragg gratings. After characterising single phase shifts in simple gratings, longer and more complex codes are accurately measured. Finally, by studying the phase shifts of the optical waveforms reflected from temperature tunable gratings, we were able to gain valuable information about the spatial phase shifts induced in the Bragg gratings by this temperature tuning.

The linear spectrogram characterisation method is further applied to high capacity optical transmission systems, as explained in Chapter 5. Wavelength division multiplexing systems are key to unlocking some of the vast capacity of the optical fibre. In this chapter, I show how linear spectrograms can be used to characterise many channels simultaneously, and after transmission over a recirculating loop. Finally, I discuss a series of results obtained through collaborative work with *Acreo AB*, on high speed data modulation. Focussing on the alternating phase, return to zero modulation format, we were able to demonstrate the linear spectrogram method after transmission over an installed fibre link.

In Chapter 6, I summarise the thesis, and present a few thoughts on future directions.

References

[1] M. Dècina, "The Future of Networking," 29th European Conference on Optical Communication, Rimini, Italy (2003).

[2] E. Desurvire, "Optical communications in 2025," 31st European Conference on Optical Communication **1**, 5 – 6 (2005).

[3] B. Ferren, "Optical Fiber Communication – What's Next?" OFC/NFOEC 2006, Anaheim, Plenary Session (2006).

[4] R. Trebino, *Frequency-resolved optical gating : the measurement of ultrashort laser pulses* (Kluwer Academic Publishers, Boston, Ma., 2000).

Chapter 2

Signal Characterisation

The measurement of the electric field of light pulses, or waveforms in general, provides better understanding of their behaviour when they are applied in many fields of optics. In optical telecommunication applications in particular, full knowledge of the electric field (amplitude and phase) of the waveform is crucial to the verification of mathematical models and provides a basis for numerical simulations of complete transmission systems.
Pulses are for example distorted whilst propagating through optical fibres because of chromatic dispersion and nonlinearities. Knowing exactly how the waveform is distorted leads to the possibility to quantify the properties of fibres and other optical devices. It also makes it possible to verify various efforts in pulse generation and shaping, and allows one to optimise various parameters in a transmission network. The work in this thesis covers several of these interesting fields as described in later chapters. In this chapter, I present a brief overview of different waveform characterisation methods applicable to the optical telecommunications field, together with a more detailed explanation of the main characterisation techniques used in further chapters.

2.1 Introduction

The limited sampling bandwidth of electrical sampling oscilloscopes and the slow rise time of current photo-detectors distort the measurement of temporal intensity profiles of optical telecommunication rate pulses. Also, the square law detection

with photo-detectors (photocurrent is proportional to the intensity of the optical signal) implies that the phase information of the signal is disregarded. For a complete characterisation, i.e. phase and intensity profiles, of optical pulses, it can be shown that both time-stationary and time-non-stationary filters are needed in the setup. Walmsley and Wong have explained this basic framework for pulse characterisation in Ref. [1].
Of course, this does not mean that other measurements, not satisfying these conditions, would be irrelevant or useless. Autocorrelations, optical spectrum analyser (OSA) measurements and electrical and optical sampling traces are some of the most frequently used tools in any telecommunications lab to conveniently assess the basic properties of optical waveforms.

An optical pulse is uniquely described by its analytic signal in the time domain:

$$E(t) = A(t)\exp(i\phi_t(t) + i\phi_0 - i\omega_0 t) \tag{2.1}$$

where $A(t)$ is the time dependent envelope, ω_0 is the carrier frequency, $\phi_t(t)$ is the time dependent phase and ϕ_0 a constant. The intensity profile of the pulse is calculated as $|E(t)|^2$, which could be measured by a photo-detector of sufficient bandwidth (i.e. a bandwidth larger than about $0.35/Tr$, where Tr is the rise time of the pulse). In the spectral domain, the pulse is represented as follows:

$$\tilde{E}(\omega) = \tilde{A}(\omega)exp(i\phi_\omega(\omega)) \tag{2.2}$$

where $\tilde{A}(\omega)$ is the spectral amplitude and $\phi_\omega(\omega)$ is the spectral phase. The spectral intensity is again obtained as $\left|\tilde{E}(\omega)\right|^2$. The instantaneous frequency in the time domain is defined as $\omega_0 - \partial\phi_t/\partial t$ and is closely related to the definition of chirp:

$$C(t) = -\frac{1}{2\pi}\frac{\partial\phi_t}{\partial t} \tag{2.3}$$

The group delay in the spectral domain is defined as $\partial\phi_\omega/\partial\omega$.

These variables and terms will be used frequently in the rest of this work, to point out the particularly interesting properties of the respective pulses. Note that the word 'chirp' is also frequently used in the literature to denote that a particular waveform possesses more general phase related features, for which the meaning can sometimes be ambiguous: e.g. *a chirped pulse, red-chirp, blue-chirp,...* In

this work, I will use the terms up-chirp and down-chirp to denote that the instantaneous *frequency* of the pulse increases or decreases with time respectively.
In the following section, I will first give an overview of different optical pulse characterisation techniques. Sections 2.3, 2.4 and 2.5 discuss two particular complete pulse characterisation methods in more detail, and are then compared with each other experimentally in Section 2.6.

A totally different, but more conventional way of assessing the performance of an optical network, is given by bit error rates, and the related Q-factor measurements. In Appendix A, I document the work I have performed on implementing a system to measure the Q-factor automatically.

2.2 Characterisation techniques

The measurement of the spectral intensity profile of waveforms is fairly straightforward, as photo-detectors inherently measure the intensity. The waveforms can for example be diffracted spatially with a grating and then the power of their constituent wavelengths measured with a single detector, thereby determining the spectrum of the pulse.
To measure the intensity profile in the temporal domain is more challenging, certainly for pulse durations and pulses with features that are much faster than the fastest electronic devices. Optical sampling technology overcomes this problem. The signal is combined with a very short sampling pulse at a different repetition rate in a nonlinear medium, a highly nonlinear fibre for example [2, 3, 4]. A nonlinear interaction, such as four wave mixing FWM, between the two pulses creates a signal at the idler wavelength that can be filtered out – provided that the spectral separation between the sampling pulse and the signal is sufficient. Each idler pulse represents a sample from the signal, and its energy is proportional to the power of the signal at the position of temporal overlap with the sampling pulse. With a low bandwidth photo-detector, the temporal profile of the signal intensity can then be displayed on an electrical oscilloscope. This technique is polarisation sensitive due to the polarisation sensitivity of the nonlinear process, but more elaborate implementations based on the same technique can overcome this problem [3]. The resolution in optical sampling techniques is limited to approximately the duration of the sampling pulse. Ultrashort pulses, such as the sampling pulses (in the above

references these are 1 or 2 *ps* long), are therefore not measurable in this way, due to a lack of the even shorter pulses required.

An intensity autocorrelator uses the pulse under test itself as the 'sampling' pulse [5]. The pulse is split up, and the two replicas are then scanned through each other by delaying them appropriately with respect to each other, and then focussed on a second harmonic generation (SHG) crystal. When the two replicas overlap temporally upon arrival in the SHG crystal, they generate second harmonic photons, proportional to $(E(t)+E(t-\tau))^2$. With an appropriate optical setup where the two replicas of the original pulse arrive at the crystal with opposite angles of incidence, the cross-product is filtered out spatially, through conservation of momentum:

$$E_{sig}(t,\tau) \propto E(t)E(t-\tau). \tag{2.4}$$

A slow detector then measures this signal, which is essentially the autocorrelation intensity of the signal:

$$A^{(2)}(\tau) \propto \int_{-\infty}^{\infty} |E(t)E(t-\tau)|^2 \, dt = \int_{-\infty}^{\infty} I(t)I(t-\tau)dt \tag{2.5}$$

As $A^{(2)}(\tau)$ equals $A^{(2)}(-\tau)$, there is no information about the time direction of the pulse. In the literature, the intensity autocorrelation is a frequently used way to assess the duration of the pulse, however there is no exact way of unambiguously telling just how long the pulse really is, without further knowledge about the waveform. For example, the autocorrelation of a Gaussian pulse is also a Gaussian, with duration of 1.41 times the duration of the signal pulse. A rectangular pulse has a triangular autocorrelation, with the same full width at half maximum (FWHM) as the pulse, and the autocorrelation of a hyperbolic secant pulse has a duration that is 1.54 times the length of the pulse, etc.
On many occasions in the literature, the authors just assume a certain pulse shape to calculate the length of the pulse from its autocorrelation trace. These conclusions are unreliable though, as even fairly complex pulses can have a very nice Gaussian looking autocorrelation profile (see for example ref. [6]). The autocorrelation has certainly earned its place in the armoury of characterising techniques for short pulses, but in truth, it does not reveal much about the exact pulse shape or its exact length.

Complete pulse characterisation

Broadly speaking, there are three different categories of measurements that allow the complete characterisation of optical waveforms: tomographic, interferometric and spectrographic methods. There is no direct way of measuring the phase and intensity of an optical waveform, so the aforementioned techniques all involve an 'inversion' step, in which the intensity and phase are inferred from a set of measurements [1]. What follows is an overview with some examples of each of these three methods.

2.2.1 Tomographic pulse characterisation

Tomography originates from imaging applications where one tries to reconstruct for example two or three dimensional objects from one or two dimensional projections respectively. It can be applied to optical signal characterisation as well.

The electric field of a pulse $\tilde{E}(\omega) = \sqrt{I(\omega)}\exp(i\phi(\omega))$ (with $I = Z_0 P_D$, P_D and Z_0 representing the power density and the characteristic impedance in free space respectively) can also be fully represented by a time-frequency distribution called the Wigner-Ville distribution [7]:

$$W(t,\omega) = \frac{1}{2\pi}\int \tilde{E}(\omega + \frac{\omega'}{2})\tilde{E}^*(\omega - \frac{\omega'}{2})\exp(-i\omega' t)d\omega'. \tag{2.6}$$

From this, the electric field of the signal can immediately be calculated as [7]:

$$\tilde{E}(\omega) = \frac{1}{\tilde{E}^*(\omega = 0)}\int W(t, \frac{\omega}{2})\exp(it\omega)dt. \tag{2.7}$$

From a large number of projections of this function on the frequency axis after a varying rotation in its 2D phase-space, the Wigner-Ville distribution can be reconstructed by using a back-projection algorithm. However, due to the large number of projections needed, and the difficulty in generating large rotations practically, this method has not been implemented experimentally yet, even though the spectral projection would not be difficult to measure with a spectrometer.

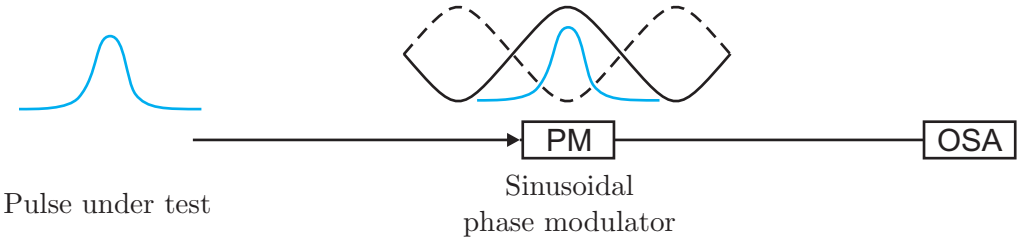

FIGURE 2.1: Experimental implementation of simplified chronocyclic tomography.

It is possible though, assuming coherent light pulses, to simplify this technique so that with only two projections of the Wigner-Ville distribution after small rotations, the distribution can be reconstructed [8]. This leads to a very practical implementation that only requires a sinusoidal phase modulator synchronised to the pulse source and a spectrometer (Figure 2.1). This experimental setup has been used to accurately characterise pulses as short as a few *ps*. The technique becomes less accurate however when characterising pulses of longer duration (>15 *ps*), as it relies on the pulse overlapping with the parabolic part of the phase modulation curve. Its advantages are the very simple implementation and good sensitivity, as there are no nonlinear effects involved.

2.2.2 Interferometric pulse characterisation

In spectral interferometric techniques, one relies on converting the phase properties of the pulse into amplitude information. This makes it possible to directly measure the phase difference between the optical frequencies in the pulse.
What follows is a brief explanation of Fourier transform spectral interferometry [9, 10]. Let $E(t)$ and $E_0(t)$ be the temporal electric fields of an unknown pulse and a known reference pulse. A delay τ is introduced to one of the pulses, after which they are (re)combined and spectrally resolved. The measured intensity is:

$$I(\omega) = |E_0(\omega) + E(\omega)\exp(i\omega\tau)|^2 = |E_0(\omega)|^2 + |E(\omega)|^2 + E_0^*(\omega)E(\omega)\exp(i\omega\tau) + c.c. \tag{2.8}$$

With $f(t) = E_0^*(-t) \otimes E(t)$, we can rewrite this as:

$$I(\omega) = |E_0(\omega)|^2 + |E(\omega)|^2 + f(\omega)\exp(i\omega\tau) + c.c. \tag{2.9}$$

$f(\omega)$ is the Fourier transform of $f(t)$:

$$f(\omega) = |E_0^*(\omega)E(\omega)| \exp(i\Delta\phi(\omega)) \tag{2.10}$$

where $\Delta\phi(\omega) = \arg(E(\omega)) - \arg(E_0(\omega))$, the spectral phase difference between the two pulses, meaning that $f(\omega)$ contains all the information on the spectral phase difference. An inverse Fourier transform of equation 2.9 leads to:

$$F^{-1}I(\omega) = E_0^*(-t) \otimes E_0(t) + E^*(-t) \otimes E(t) + f(t-\tau) + f(-t-\tau)^*. \tag{2.11}$$

The first two terms are autocorrelation functions of the individual fields, and centred around $t = 0$. Therefore, for reasonably well-behaved pulses and large enough values of τ, $f(t-\tau)$ does not overlap with the other terms in this equation [9]. This term can thus be filtered out mathematically, and re-centred around zero: $f(t)$. Its Fourier transform $f(\omega)$ is then used to obtain the electric field of the unknown pulse:

$$E(\omega) = \frac{f(\omega)}{E_0^*(\omega)}. \tag{2.12}$$

Or the spectral phase difference can be calculated as $\Delta\phi(\omega) = \arg(f(\omega))$.

Self-referenced interferometry

The reference pulse can be replaced by a spectrally sheared version of the pulse under test: $E(\omega - \Omega)$. The phase difference then becomes $\Delta\phi(\omega) = \phi(\omega) - \phi(\omega - \Omega)$, which can be integrated to find the phase of the pulse under test. Together with an independent measurement of the spectrum of the pulse, this completely characterises the pulse.
Spectral phase interferometry for direct electric-field reconstruction (SPIDER) [11] is a self-referenced interferometric technique that achieves the spectral shearing by mixing two replicas of the test pulse with a relative delay τ with a highly chirped pulse, converting the time delay between the pulses into a spectral shear.

Recently, another implementation that does not rely on nonlinearities has been demonstrated [12], see Figure 2.2. The spectral shearing in this case is achieved by temporally modulating the pulses under test with a sinusoidal phase modulation. The pulse under test is split in a Mach-Zehnder interferometer, generating two replicas of the pulse separated by 100 *ps*. The pulses acquire an alternating

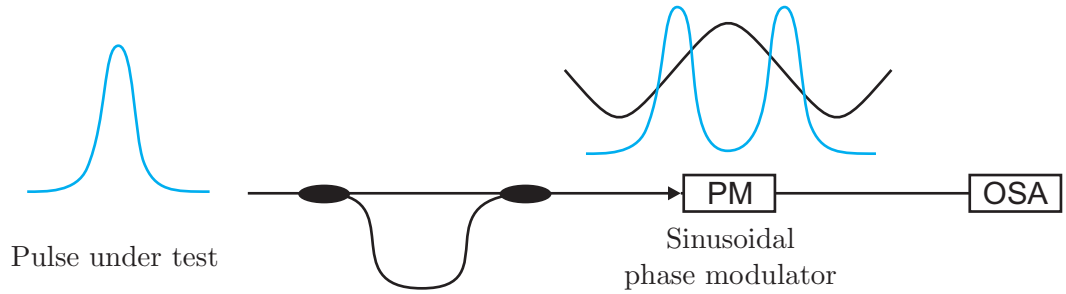

FIGURE 2.2: Experimental implementation of spectral shearing interferometry, using a phase modulator to perform the spectral shearing.

frequency shear when they overlap with the linear parts (at the zero crossing) of the 5 GHz sinusoidal phase modulation. The two pulses are then again resolved with a spectrum analyser to create the interferogram.
This technique would be very attractive for telecommunication pulses, because of its direct retrieval of the phase information, and the simplicity of its implementation. However, the repetition rates are not compatible with this technique, as the phase modulation repetition rate must be a multiple of the repetition rate of the signal under test [12]. This means that the signal under test (with a high speed repetition rate) needs to be gated down to a lower repetition rate. The electrical bandwidth of current phase modulators is limiting here, together with the fact that the length of the pulses characterisable with this method is limited to the duration over which the sinusoidal modulation is sufficiently linear.

Apex complex spectrum analyser

Another full waveform interferometric technique is currently being marketed by *Apex Technologies*, and is based on a patent from France Telecom. Its principles are published in [13, 14], and briefly explained below. With T the period and $F = 1/T$ the fundamental frequency of the signal under test, the electric field can be written as a Fourier expansion:

$$E(t) = A(t)\exp(i2\pi f_0 t) = \sum_k A_k \exp\left\{i(2\pi(f_0 + kF)t + \phi_k)\right\} \tag{2.13}$$

or in other words, a sum of spectral lines around the carrier frequency f_0 with A_k and ϕ_k as their respective amplitudes and phases. The amplitude of the spectral lines can be measured with a straightforward intensity measurement, whilst the phase is determined as follows. The signal is weakly modulated sinusoidally at a

frequency of $F/2$, so that each spectral line in the original spectrum creates two symmetrical lines at $\pm F/2$ from this line. This weak modulation is synchronised with the waveform under test, and has a variable delay τ with respect to it. With $L_+(k)$ and $L_-(k)$ the lines generated at $(f_0 + kF \pm F/2)$, the lines $L_+(k)$ interfere with the lines $L_-(k+1)$, as they have the same frequency. The resulting power of these lines is proportional to $cos(2\pi F\tau + \phi_{k+1} - \phi_k)$. By measuring the power variations as a function of the delay τ, the phase difference $\phi_{k+1} - \phi_k$ can be directly calculated, and hence the spectral phase can be integrated from this difference.

This technique requires a very high resolution spectrum analyser, as it needs to be able to resolve spectral lines at half the repetition rate of the signal. For the Apex Complex Spectrum Analyser, which requires input repetition rates of 625 *MHz*, a resolution finer than 312.5 *MHz* is required. Apex therefore integrated an optical spectrum analyser based on optical heterodyning [15] in their device. The polarisation sensitivity of this technique is overcome by separate analysis of the two orthogonal polarisation states.

2.2.3 Spectrographic pulse characterisation

Spectrographic complete pulse characterisation techniques represent perhaps the widest spread of different implementations for telecommunications applications among the three categories discussed here. This is despite the fact that these techniques require more postprocessing of the measured traces, called spectrograms, compared to the direct calculation possible with the previous two classes. Spectrographic techniques normally require iterative algorithms in order to retrieve the complete pulse information. A brief introduction on spectrographic techniques is presented below. Further sections in this chapter contain a more detailed description of two particular implementations that have been used extensively for the pulse and waveform characterisation during the course of this work. Section 2.5 then explains the algorithm used to retrieve the information from the spectrogram traces, and Section 2.6 presents a practical comparison between these two implementations.

Just like the Wigner-Ville function, a spectrogram is a time frequency distribution of a pulse, or a pair of pulses. A spectrogram is easier to measure though, as it does not involve time-reversed versions of the pulse. Measuring a spectrogram involves the use of a time-stationary and a time-nonstationary filter. Based on which of

these comes first in the setup, the obtained trace is either called a spectrogram, or a sonogram. For a spectrogram, one measures the intensity spectrum of a pulse $E(t)$ after gating $G(t)$ as a function of the delay τ between the gating function and the pulse under test. The experimental trace is thus represented by:

$$S(\tau,\omega) = \left| \int E(t)G(t-\tau)\exp(i\omega t)dt \right|^2, \tag{2.14}$$

which is a convolution of the Wigner function of the pulse and the Wigner function of the gate. For a sonogram [16], the temporal intensity of the pulse is measured after spectral filtering as a function of the filter position Ω, or in other words, the time of arrival of the different spectral components of the pulse is measured. The experimental trace is in this case represented by:

$$S(\Omega,T) = \left| \int E(\omega)G(\omega-\Omega)\exp(i\omega T)d\omega \right|^2. \tag{2.15}$$

These experimental intensity traces do not contain any direct phase information about the pulse. However, it is possible to reconstruct the constituent pulse and gate functions completely through iterative numerical calculations. The most frequently used algorithm is explained in Section 2.5. Spectrograms have an advantage over sonograms in the fact that they only need a high resolution spectrometer and a high resolution delay line, two readily available elements in optics. Obtaining the fast photodetectors that would be needed to characterise pulses with sonograms is much more of a difficulty, certainly when the pulse length goes down to *ps* durations or below. Therefore, sonograms are usually measured by means of a cross-correlation between the spectrally gated signal with the signal under test [17]. The experimental trace is now given by a convolution of the sonogram with the unknown temporal intensity of the pulse under test. This fact can be included in the retrieval algorithm.

A popular implementation of a spectrographic technique is based on nonlinear interaction in a second harmonic generating crystal between two replicas of the pulse under test. It is called FROG, or Frequency Resolved Optical Gating, and is explained in more detail in Section 2.3. Research into different implementations of spectrograms has been very active for over a decade now. One slightly different implementation is based on a known gating function, so that the complete information of the pulse under test can be calculated immediately from the spectrogram, without the need for an iterative algorithm [18]. A particularly suitable

implementation for telecommunication rate pulses was introduced by Dorrer and Kang [19]. Because it is frequently used in this thesis to characterise all sorts of waveforms, a more detailed explanation of this technique follows in Section 2.4.

2.3 FROG

2.3.1 Gating through second harmonic generation

Frequency resolved optical gating (FROG) using nonlinear mixing in a second harmonic generation crystal (SHG-FROG) is among the most frequently used FROG techniques in the optical telecommunications area. A schematic showing the principle of measuring an SHG-FROG trace is shown in Figure 2.3. Just like in an optical autocorrelator, the pulse is split into two replicas, one of which passes through a variable delay stage. The two pulses are then recombined within the SHG crystal. Where there is temporal (and spatial) overlap between the two pulses, they generate photons at the sum-frequency of the two overlapping photons. This SHG pulse is then spectrally resolved with a spectrometer, as a function of the delay between the two replicas of the original pulse.

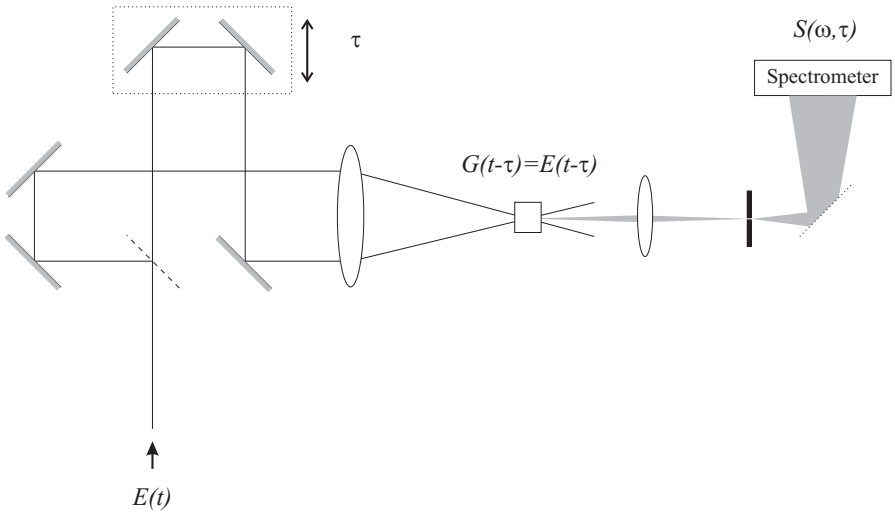

FIGURE 2.3: Scheme showing the operating principle of the FROG.

The spectrogram function (2.14) becomes, in this case with $G(t) = E(t)$:

$$S(\tau, \omega) = \left| \int E(t)E(t-\tau)\exp(i\omega t)dt \right|^2 , \tag{2.16}$$

This can also be seen as a spectrally resolved autocorrelation trace, and just like the autocorrelation, this two-dimensional FROG trace is a time symmetric function. This leads to an inherent ambiguity in the direction of time: $E(t)$ and $E(-t)$ produce the same SHG-FROG spectrogram. This 'trivial' ambiguity is easily resolved by taking another measurement of the pulse after inducing a certain known distortion, for example propagating the pulse through a known dispersive medium, or by altering the pulse in such a way that a trailing pulse accompanies the original pulse [20]. The position of this secondary pulse with respect to the original pulse in the retrieved waveform information will then establish the direction of time of the retrieved waveform.
Another ambiguity in SHG-FROG, is that two well separated pulses with relative phase differences of ϕ or $\phi + \pi$ yield the same spectrogram [21]. This is clearly not desirable in the case of alternating phase return to zero-pulses, such as the ones following in Chapter 5.

More practical problems which this particular technique suffers from are related to the bandwidth of the pulse. On one hand, the bandwidth of the SHG crystal has to be sufficient to frequency double over the entire bandwidth of the pulse. Since the SHG bandwidth of the crystal is inversely proportional to the thickness, thinner crystals generally have a larger bandwidth. Unfortunately though at the same time, they become less efficient, resulting in a trade-off in terms of sensitivity and resolution.
On the other hand, when the pulses are longer temporally, they become narrower spectrally. This requires better resolution of the spectrometer, generally meaning a longer diffraction length and thus bigger apparatus.

A schematic of the commercial FROG apparatus used in our lab is shown in Figure 2.4. It is a *Southern Photonics* HR100 Pulse Analyser, and is specified to have a temporal resolution of 15 fs. It can characterise pulses with a duration between 300 fs and 10 ps. It is used for several characterisations of pulses within this thesis. I also compared this technique experimentally with the technique described in Section 2.4 for a range of different telecommunication pulses (see Section 2.6).
A great advantage of FROG techniques in general is that they are inherently self-referenced. Suitable design of the optical paths in the device therefore ensures that timing-jitter effects are completely cancelled out.
One disadvantage is that it needs careful free space alignment of the pulses in the different paths. Another disadvantage is that the technique relies on nonlinearities.

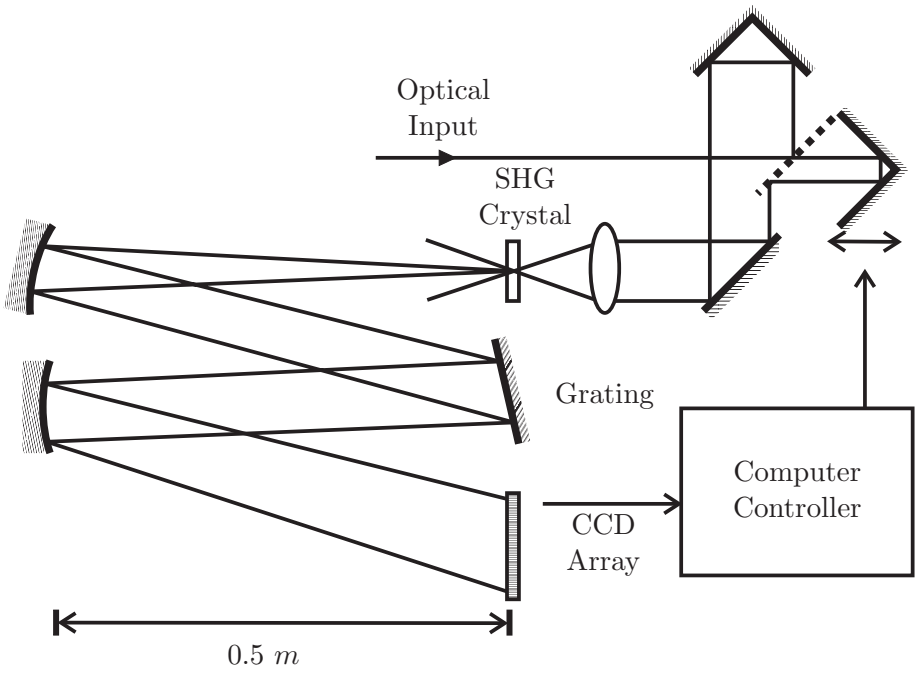

FIGURE 2.4: Southern Photonics HR100 Pulse Analyser schematic.

With a second order nonlinearity in the case of SHG-FROG, the sensitivity of SHG-FROG scales with the peak power-average power product, whereas the sensitivity of the linear spectrogram technique, as described below, scales simply with average power.

Apart from the SHG-FROG, there are various other techniques that use an optical nonlinear gate based on the pulse under test to create the spectrogram. A summary of the most important ones is given by Trebino *et al.* [21].
Another important development in this area is the so called GRENOUILLE [22], which apart from the French translation of FROG also stands for: GRating-Eliminated No-nonsense Observation of Ultrashort Incident Laser Light E-fields. Here, the delay line and the beam splitter are replaced by a Fresnel biprism, and the SHG-crystal is now a *thick* one, which as well as providing the nonlinear element, also acts as the spectrometer. A combination of cylindrical lenses then maps the SHG signal onto a two-dimensional detector array (a camera). The advantage of this implementation is that there are no movable parts and the setup is essentially single-shot. The GRENOUILLE generates spectrogram traces that are identical to the SHG-FROG setup, with that merit that a thick SHG crystal can have much better efficiency than a thin one, which makes the device more sensitive. At the same time, this device can also be used to measure spatio-temporal

distortions in pulses as well as pulse-front tilt [23]. There is a trade-off though that limits the applicability of the technique: the thick crystal that is used simultaneously as the SHG medium, and to spectrally resolve the pulse, distorts the pulse through group velocity dispersion when it becomes too thick. The upper and lower boundaries imposed by this trade-off are certainly in the $1.5\mu m$ region still quite restrictive. Due to the difficulty to find suitable crystals for this wavelength region, only pulses with a duration between 100 fs and a few ps are accurately measurable [24].

In the next section I will first explain a linear equivalent of this FROG method. The deconvolution algorithm is the same for both methods, and will then be explained Section 2.5.

2.4 Linear spectrograms with EAM-sampling

The development in 1995 of the two dimensional deconvolution algorithm described in the next section made blind-FROG possible [25], and with that a new category of frequency resolved complete pulse characterisation methods was born. This algorithm removes the need for a known functional relationship between the pulse and the gate making up the spectrogram. The techniques described in the previous section could thus also be used with two different pulses, instead of replicas of the same pulse. Dorrer and Kang then demonstrated in 2002 that it is also possible to implement the gating with a modulator [19], instead of relying on nonlinear optics. This method is particularly interesting for telecommunication rate pulses, as it can be implemented using devices previously designed for optical telecommunications. The scheme is shown in Figure 2.5.

The stream of pulses under test is fed into the optical modulator, which has a modulation function represented by $G(t)$. The sampling modulator is synchronised to the pulse stream, as it is driven by the same RF signal generator. As will be seen later, it can also be made self-referenced. An RF phase shifter in one of the paths is used to temporally shift (τ) the modulation relative to the pulses. The spectrum of the remodulated, or actually *coarsely sampled* signal $E(t)G(t-\tau)$ is then measured with an optical spectrum analyser (OSA), for a series of incremental

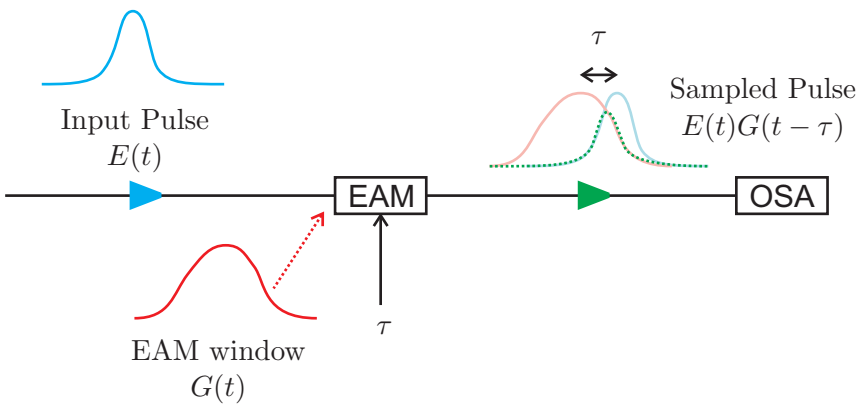

FIGURE 2.5: The linear spectrogram technique originally proposed by Dorrer and Kang.

delays τ that spans the full pulse period:

$$S(\tau,\omega) = \left| \int E(t)G(t-\tau)\exp(i\omega t)dt \right|^2 . \tag{2.17}$$

It is interesting to note that as well as retrieving the complete pulse information, the phase retrieval algorithm simultaneously characterises the sampling function of the modulator used in the experiment. A particularly suitable modulator is the electro-absorption modulator, and is described in more detail in the following chapter. Its main advantages are that very fast switching speeds are achievable, and they can be made very much polarisation insensitive.

We first implemented this technique in our lab using an optical delay stage instead of the RF phase shifter. Initially, this delay stage was tuned manually whilst saving each spectrum on a floppy disk, but it soon became clear that this was not an ideal arrangement. Due to the long time it took for one measurement – about 1 hour – the measured spectrogram was distorted due to changing lengths in the optical and electrical paths in the setup caused by fluctuating temperatures in the lab.

Two enhancements I developed drastically improved the quality of the spectrograms, and with that the retrieval process. Figure 2.6 shows the schematic of the setup that we now regularly use in the lab to characterise pulses. First of all, by using a fast photo-detector followed by an electrical amplifier, the setup is made self-referenced. Part of the pulse under test is split off with an optical fibre coupler, and converted into an electrical signal that is used to drive the sampling modulator. The combination of a fast photo-detector (32 GHz bandwidth) and

a broadband amplifier also allows us to create shorter electrical pulses than the sinusoidal signals available from an RF signal generator. This makes it possible to create shorter sampling windows in the modulator.

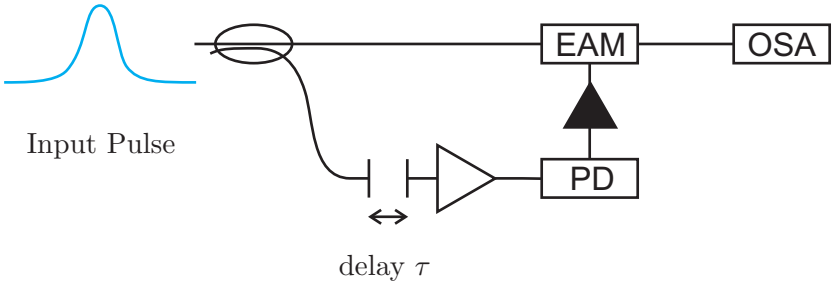

FIGURE 2.6: The scheme of the self referenced linear spectrogram technique.

Secondly, I automated the whole spectrogram acquisition setup. A computer controllable delay stage and the optical spectrum analyser have been programmed in the programming language *Delphi*, heavily building on the *general purpose interface bus* (GP-IB) commands of both devices. A snapshot of the program interface is shown in Figure 2.7. This automated setup is now able to acquire a complete spectrogram in just under a minute, depending on the exact settings of the OSA (i.e. the number of points, the spectral resolution, averaging settings, etc.) The data transfer speed of the GP-IB and the wavelength scanning speed are the limiting factors in this acquisition setup.

As can be seen in Figure 2.6, an optical amplifier follows the delay stage. The saturated output power of the optical amplifier can be fixed and this is exploited to equalise the power after the delay stage, which has a delay dependent insertion loss. In theory, the position of the delay stage can be chosen arbitrarily between either within the path of the optical signal that is then modulated by the EAM, or within the path where the optical signal is converted to an electrical signal. However, the fact that the delay stage has a delay dependent insertion loss forces us to choose the second option, in order to eliminate any distortion of the experimental spectrogram.
Further on in this thesis, various adaptations are made to this setup, to accommodate for either higher bit rates, or more complex waveforms. The updated experimental setups will be explained where appropriate, but until further notice, the 'standard' setup for linear spectrogram acquisition is the one shown in Figure 2.6.

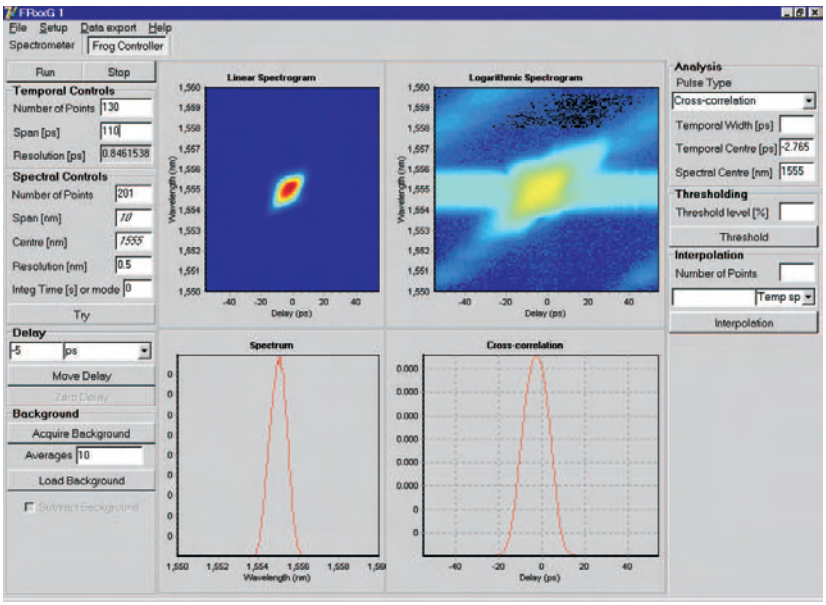

FIGURE 2.7: Front end user interface of the spectrogram acquisition program, after the measurement of a gain switched pulse.

Note that an implementation allowing real-time retrieval of the pulse and gate fields has recently been demonstrated [26, 27]. A fast scanning Fabry-Pérot etalon followed by a photodiode replaces the optical spectrum analyser, and the phase shifter is voltage controlled. Appropriate synchronisation between these two devices allows for a very fast acquisition of a complete spectrogram. To speed up the convergence of the reconstruction algorithm, the retrieved gating function of a particular spectrogram is fed into the retrieval of the following spectrogram as an initial guess. All this leads to an impressive refresh rate of 10 *Hz*.

2.5 Spectrogram reconstruction

The previous sections show how an experimental spectrogram can be measured. These spectrograms do not contain any direct phase information about the pulse or the gate that they consist of. They are merely a series of spectral intensity measurements of the convolution between the pulse and the gating function. Contrary to the one-dimensional phase retrieval problem, that is unable to deliver a unique solution, the two-dimensional phase retrieval problem here does allow one to extract the pulse and gate information completely. It is a problem that has previously been solved in image science [25, and references within].

The problem of phase retrieval from the spectrogram is simplified when there is a known functional relationship Γ between the pulse and the gate:

$$G(t) = \Gamma[E(t)], \tag{2.18}$$

as is the case in SHG-FROG for example, where $G(t) = E(t)$.
There are now two constraints that the spectrogram obeys. The first one is the physical constraint, and defines which signal is actually measured:

$$E_{sig}(t,\tau) = E(t)\Gamma[E(t-\tau)] \tag{2.19}$$

The second one is the intensity constraint, implied by the fact that the trace is a spectral intensity measurement:

$$I(\omega,\tau) = \left| \int_{-\infty}^{\infty} E_{sig}(t,\tau)\exp(i\omega t)dt \right|^2 . \tag{2.20}$$

The phase retrieval problem can be written as follows:

$$\sqrt{I_{meas}(\omega,\tau)}\phi(\omega,\tau) = \int_{-\infty}^{\infty} E(t)\Gamma[E(t-\tau)]exp(-i\omega t)dt, \tag{2.21}$$

with $I_{meas}(\omega,\tau)$ the measured spectrogram, and $E(t)$ the electric field envelope of the measured pulse. The reconstruction of $E(t)$ is possible through mathematical iteration of the following steps. Starting off with an initial guess of the pulse, one can construct a spectrogram of this pulse mathematically, based on equations (2.19) and (2.20): $\sqrt{I_{calc}(\omega,\tau)}\phi_{calc}(\omega,\tau)$. The next step is to replace the *intensity* of this mathematical trace by the measured intensity, to apply the intensity constraint, so that we get:

$$E'_{sig}(t,\tau) = F^{-1}\left\{\sqrt{I_{meas}(\omega,\tau)}\phi_{calc}(\omega,\tau)\right\}. \tag{2.22}$$

Only the phase information in the calculated trace is thus retained. The guess for $E(t)$ in the next iteration is based on this semi-experimental trace, and leads to a

new spectrogram. The goal is to minimise the spectrogram error ϵ:

$$\epsilon = \sqrt{\frac{1}{N^2}\sum_{i=1}^{N}\sum_{j=1}^{N}[I_{calc}(\omega_i,\tau_j) - I_{meas}(\omega_i,\tau_j)]^2} \tag{2.23}$$

where N represents the number of time points and frequency points, ω_i is the ith frequency point and τ_j is the jth delay in the measured spectrogram. Ideally, the next guess for $E(t)$ delivers a better estimate for the phase of the spectrogram, and the spectrogram error reduces, eventually converging to the solution. A variety of ways to determine the next guess have been described in the literature [see references in 28], but the Generalised Projections algorithm stands out in particular because of its robustness, the fact that it virtually guarantees a decreasing error for each iteration, and its speed. Here, the next guess for $E(t)$ is determined by the minimisation of the following error function with respect to $E(t)$:

$$Z = \sum_{t,\tau=1}^{N} \left|E'_{sig}(t,\tau) - E(t)\Gamma[E(t-\tau)]\right|^2. \tag{2.24}$$

2.5.1 Principal components generalised projection

Rather than actually minimising this function, which is computationally very demanding, a more elegant and general implementation called principal components generalised projections was introduced by Kane, and is explained in detail in Ref. 28. Here, there is no longer a requirement for a functional relationship Γ between the pulse $E(t)$ and the gate $G(t)$.

A measured spectrogram trace consists of sampled intensity values of the product $E(t)G(t-\tau)$ at given values of the delay τ and frequency ω. One can think of $E(t)$ and $G(t)$ as vectors whose elements sample E and G at discrete times with interval Δt:

$$\begin{aligned} E_{pulse} &= \left[E\left(-\frac{N}{2}\Delta t\right), E\left(-\left(\frac{N}{2}-1\right)\Delta t\right), \cdots, E\left(\left(\frac{N}{2}-1\right)\Delta t\right)\right] \\ &= [E_1, E_2, \ldots, E_N], \end{aligned} \tag{2.25}$$

and

$$E_{gate} = \left[G\left(-\frac{N}{2}\Delta t\right), G\left(-\left(\frac{N}{2}-1\right)\Delta t\right), \cdots, G\left(\left(\frac{N}{2}-1\right)\Delta t\right)\right] = [G_1, G_2, \ldots, G_N]. \tag{2.26}$$

The outer product of these two vectors is:

$$O.P. = \begin{bmatrix} E_1G_1 & E_1G_2 & E_1G_3 & \cdots & E_1G_N \\ E_2G_1 & E_2G_2 & E_2G_3 & \cdots & E_2G_N \\ E_3G_1 & E_3G_2 & E_3G_3 & \cdots & E_3G_N \\ \vdots & \vdots & \vdots & \ddots & \vdots \\ E_NG_1 & E_NG_2 & E_NG_3 & \cdots & E_NG_N \end{bmatrix}. \tag{2.27}$$

This matrix contains all the points required to construct the time domain spectrogram trace $E(t)G(t-\tau)$, as it contains all of the interactions between the pulse and the gate for each time delay. A one-to-one reversible mapping of the elements in this matrix can transform the outer product into the time domain spectrogram trace:

$$T.D. = \begin{bmatrix} E_1G_1 & E_1G_2 & E_1G_3 & \cdots & E_1G_N \\ E_2G_2 & E_2G_3 & E_2G_4 & \cdots & E_2G_1 \\ E_3G_3 & E_3G_4 & E_3G_5 & \cdots & E_3G_2 \\ \vdots & \vdots & \vdots & \ddots & \vdots \\ E_NG_N & E_NG_1 & E_NG_2 & \cdots & E_NG_{N-1} \end{bmatrix}. \tag{2.28}$$

For the reconstruction of the spectrogram, one starts again with a random guess for the pulse and the gate. The spectrogram is constructed according to equation 2.17, and the magnitude of the spectrogram is replaced by the square root of the measured intensity. This trace is then inversely Fourier transformed to the time domain, and transformed to the outer product form (2.27).

If the intensity and phase of the spectrogram are correct, this newly constructed outer product matrix has a rank of one. In this case, it only has one nonzero eigenvalue, one right eigenvector and one left eigenvector. The right eigenvector is then the pulse, and the left eigenvector is the complex conjugate of the gate.

The initial guesses for $E(t)$ and $G(t)$ produce an outer product matrix O that is generally not of rank one, and has several eigenvectors. It can be decomposed into

three matrices U, V and W so that:

$$O = U \times W \times V^H, \tag{2.29}$$

where U and V^H are orthogonal, square matrices, and W is a diagonal matrix. In other words, O is a superposition of outer products between the columns of U and the rows of V^H, with the relative weights given by the non-zero elements in the diagonal matrix W. Keeping the outer product pair (E_{pulse} and E_{gate}) corresponding to the largest of these elements (the principal component) minimises the function

$$\epsilon^2 = \sum_{i,j=1}^{N} \left| O^{i,j} - E^i_{pulse} E^j_{gate} \right|^2 . \tag{2.30}$$

This would reveal the best guess for the pulse and the gate vectors for the next iteration. However, a singular value decomposition (SVD) to determine the largest diagonal element and its corresponding eigenvector pair would be computationally intensive. With the vectors P_i and G_i representing the columns in matrices U and V respectively, one can write

$$OO^H P_i = \lambda_i P_i, \tag{2.31}$$

$$O^H O G_i = \lambda_i G_i. \tag{2.32}$$

When OO^H is multiplied with an arbitrary nonzero vector, we get

$$OO^H x_0 = \sum_{i=1}^{N} \kappa_i \lambda_i P_i, \tag{2.33}$$

with κ_i a set of constants. We can repeat this process:

$$(OO^H)^p x_0 = \sum_{i=1}^{N} \kappa_i \lambda_i^p P_i, \tag{2.34}$$

which leads to principal eigenvector P_l, corresponding to the largest eigenvalue λ_l when p becomes large. Thus, the next guess for the pulse vector can be obtained by multiplying the current guess by OO^H. Analogously, the next guess for the gate vector is obtained by multiplying the current gate vector by $O^H O$. Even though better approximations for the principal eigenvectors can be calculated by multiplying with OO^H or $O^H O$ several times per iteration, once per iteration seems to be adequate. The algorithm is schematically summarised in Figure 2.8. This

algorithm can be modified to incorporate a functional relation Γ between the pulse and the gate, but this is not a prerequisite. The algorithm is particularly robust when the pulse and the gate have distinctly different waveform properties.

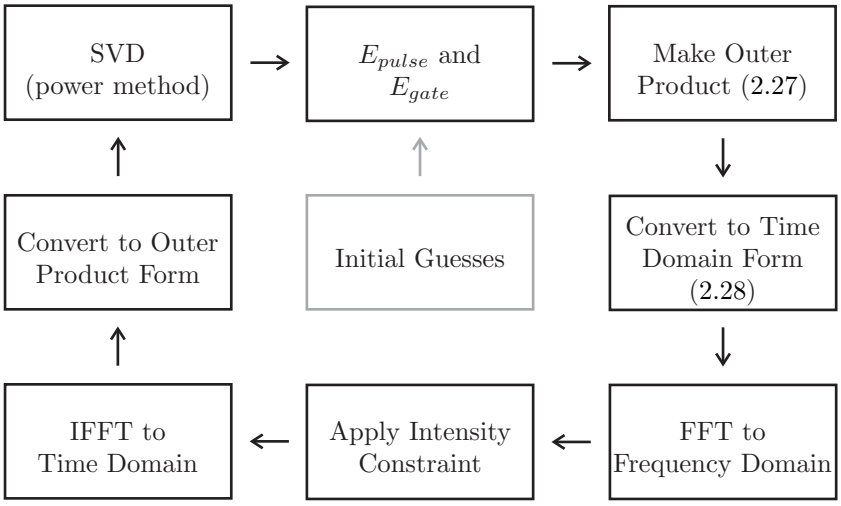

FIGURE 2.8: Summarizing schematic of the principal components generalized projections algorithm.

In analogy with this algorithm that reconstructs the temporal intensity and phase of the pulse and gate from a spectrogram, the equivalent algorithm to reconstruct a sonogram has been described in [16].

2.5.2 Algorithm additions and remarks

Even though the algorithm above is superior to other methods in terms of robustness and speed, there are cases in which it fails to converge, especially when there is a considerable amount of noise present in the measured spectrogram, or when the pulse and the gate are very similar in shape and duration. Although research into the robustness against noise has revealed that retrieval processes for spectrograms inherently distinguish between the waveform information and noise [29, 30], the algorithm eventually fails to deliver a solution, when the noise levels become too high.

Algorithms based on different schools of thought have been presented by several research groups. They include simulated annealing [31], genetic algorithms [32] and neural networks [33, 34, 35]. Even though these retrieval algorithms have promising properties, the principal components generalised projection (PCGP) algorithm is still superior because of its simple mathematical implementation. It

has certainly proven to be largely sufficient for the pulses encountered during the course of this work.
Delong and Trebino presented a summary of a series of spectrogram deconvolution algorithms in [36], and combined them in a 'composite' algorithm. Even though this article has been written before the arrival of the PCGP algorithm, it provides useful insight and various additional tricks that can improve convergence also in the PCGP algorithm. Some of these have been implemented in the Matlab code I have developed, together with a few other useful additions to the algorithm that I have conceived and developed. Below is a brief discussion, as a reference for future users of the code.

Spectral intensity constraint

Additional information about the pulse or the gate can be used in two ways in the retrieval algorithm. It can either be injected as a part of the initial guess for the pulse or the gate, to give the algorithm a head start. For example, the spectral intensity is in most cases easily obtainable by performing a simple optical spectrum analyser measurement. Adding a random phase to this spectrum creates an appropriate initial guess for the algorithm.
The other way of using this additional information is to constrain the magnitude of the pulse or the gate to the square root of the measured spectrum. Limiting the spectrum of the pulse in this way during every iteration step however is not recommended, as it restricts the algorithm too much, and it easily gets stuck in a local minimum. It can be beneficial though when this constraint is applied only after a number of iterations, as it can 'kick' the reconstruction process out of a local minimum and eventually lead it to deliver a better spectrogram error.

Overcorrection

In the step where the intensity of the calculated spectrogram is replaced by the measured spectrogram intensity, the magnitude of the reconstruction is essentially 'corrected': the magnitude is increased where it is too small, and decreased where it is too large. More specifically, this can be written as:

$$E'_{sig}(\omega,\tau) = \frac{E_{sig}(\omega,\tau)}{|E_{sig}(\omega,\tau)|}\sqrt{I_{meas}(\omega,\tau)} \tag{2.35}$$

An overcorrection can be implemented by 'amplifying' the magnitude correction:

$$E'_{sig}(\omega,\tau) = E_{sig}(\omega,\tau)\left|\frac{\sqrt{I_{meas}(\omega,\tau)}}{E_{sig}(\omega,\tau)}\right|^{\alpha}, \tag{2.36}$$

where α is the correction amplification factor. When $\alpha = 1$, this equation reduces to equation 2.35. Increasing α can lead to a faster convergence. However, it can also lead to an unstable deconvolution that repeatedly overshoots the solution and fails to converge. I found that values for α between 1 and 2 can speed up the convergence, in agreement with [36].

Ambiguities

Seifert *et al.* have recently presented a theoretical investigation into nontrivial ambiguities for blind FROG deconvolution [37]. There are three trivial ambiguities:

1. The pulse and gate pair $(\tilde{E}(\omega), \tilde{G}(\omega))$ has exactly the same spectrogram as the pair $(\tilde{E}(\omega)\exp(i(a_1 + b\omega)), \tilde{G}(\omega)\exp(i(a_2 - b\omega))$, with a_1, a_2 and b real constants. A linear phase ramp in the spectral domain is equivalent to a shift in the time domain.

2. If the spectrogram is symmetric temporally, $I_{meas}(\omega,\tau) = I_{meas}(\omega,-\tau)$, then the pair $(\tilde{E},\tilde{G})$ has the same spectrogram trace as the complex conjugate pair $(\tilde{E}^*,\tilde{G}^*)$, which corresponds to an inversion in time for the fields.

3. Also, if $I_{meas}(\omega,\tau) = I_{meas}(\omega,-\tau)$, it is impossible to distinguish between the pulse and the gate.

The latter two ambiguities can be eliminated if the spectral intensities are known (and different). However, Seifert *et al.* have shown that centro-symmetric traces can have multiple, nontrivial solutions [37]. Therefore, non-centrosymmetry is a required, although not sufficient condition for the trace to have a unique solution. The authors even hint that a spectrographic technique should create spectrograms that are as non-centrosymmetric as possible, and the spectra of the pulse and the gate should be different in order to allow a unique solution for the retrieval problem. The spectrograms presented further on in this work conform with this

suggestion. Where possible and relevant, I used consistency checks based on simulations and independent measurements to confirm the quality of the retrieved pulse information.

Spectrogram error

The spectrogram error, defined in equation 2.23 does not take into account the noise that affects any experimental trace. This error is calculated where both traces (the measured and the reconstructed trace) are normalised to a peak of unity. The fact that the highest intensity pixel is also affected by noise will slightly increase the error. Therefore, a fairer value of the error is defined as

$$\epsilon = \sqrt{\frac{1}{N^2}\sum_{i=1}^{N}\sum_{j=1}^{N}[I_{calc}(\omega_i,\tau_j) - \mu I_{meas}(\omega_i,\tau_j)]^2}. \tag{2.37}$$

Here, μ is a scaling parameter that minimises the error. Typical values that would indicate a good reconstruction, are around 0.005 for a 32×32 point grid, and 0.002 for a 128×128 point grid.

Spectrogram preparation

Before a measured spectrogram can be reconstructed mathematically, it has to be prepared adequately. It needs to be correctly sampled on a $2^n \times 2^n$ point grid for compatibility with Fast Fourier Transforms. The size of the grid depends on the complexity of the pulse and the difference in pulse duration between the pulse and the gate. Several steps to improve the quality of the measured spectrogram can also be incorporated, such as spectral and temporal filtering to average out the noise for example.
Figure 2.9 shows the different steps I incorporated in the Matlab code to adequately prepare the measured data for the deconvolution algorithm. First of all, the noise background is taken away by thresholding the data. What remains is then either spectrally averaged over a given number of pixels, or an envelope detection is executed on each of the spectral slices making up the spectrogram. After this, the spectrogram is resampled on the spectral lines (determined by the repetition rate of the pulses). This resampled spectrogram can then be interpolated onto a Fourier grid. As a final step, the spectrogram can then be filtered in the

spectrogram's 2-D Fourier domain, to try to reduce any detrimental noise effects. Depending on the exact pulse source, its stability and the optical spectrum analyser used (and its exact settings), the parameters involved in these steps may need some tweaking, in order to extract the relevant data from the measured spectrogram as accurately as is possible.

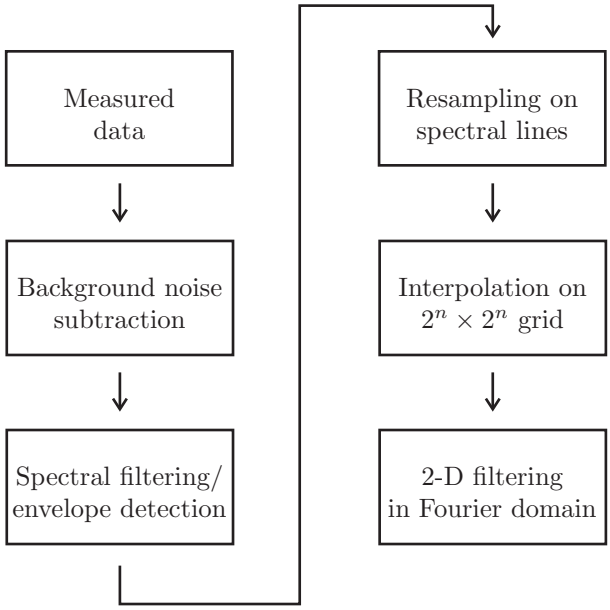

FIGURE 2.9: Schematic overview of the different steps to prepare the measured spectrogram data before feeding it into the deconvolution algorithm.

In Appendix B, I list a summary of the Matlab code, detailing the implementation of the different steps in the preparation of the spectrogram, together with the iterative PCGP algorithm.

2.6 Comparison between SHG and EAM frog

SHG-FROG, as described in Section 2.3, is a well established technique for ultrashort pulse characterisations, and has been frequently used to characterise short pulses in the 1.5 μm wavelength region. Still, it has a few drawbacks and disadvantages that make this spectrographic technique less than ideal for characterising pulses in the telecommunications area. The other spectrographic technique introduced above is based on gating with a modulator and is ideally suited for optical telecommunications.

Overcoming some of the fundamental drawbacks of SHG-FROG, the linear spectrograms acquired using sampling with an EAM have proved to give more reliable

pulse information than frequency resolved optical gating based on a nonlinear gating in a SHG crystal.

Because of the rapid recent advances in spectrographic techniques in the field of optical communications, it is difficult to find information on what the better approach is for complete pulse characterisation. Therefore, I have experimentally investigated the two spectrographic techniques mentioned above, and have compared their results for several different pulses, with durations ranging from 2 to 33 *ps*. These findings are described below and have also been published in [38].

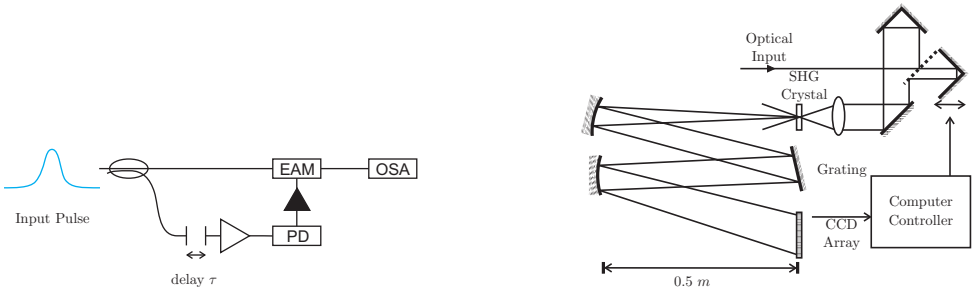

(a) Linear spectrogram setup

(b) SHG-FROG setup

FIGURE 2.10: Two spectrogram methods, side by side.

Figure 2.10 shows the two experimental setups side by side. The SHG-FROG is a device based on free space optics, and requires careful alignment of a series of mirrors, lenses and a grating. The EAM-based setup on the contrary is all fibre based, except in our case for the fibre coupled free space optical delay line, which means a much easier and more robust practical implementation.

The Czerny-Turner type spectrometer used in the SHG-FROG setup provides a spectral resolution of 20.35 *GHz*, or 0.04 *nm* at the SHG wavelength. This is in fact insufficient to adequately sample at the Nyquist frequency of 10 *GHz* for the pulses we are characterising here, which have a period of 100 *ps*. Spectrographic techniques are however particularly robust against undersampling because of the dual measurement domain approach [6]: information missing in the spectral domain can still be found in the temporal domain and vice versa. In such cases of undersampling, the traces and results should however be interpreted with care, as will be shown further on. Where possible, the retrieved information should be checked against independent information. The spectral resolution of the optical spectrum analyser used in the linear spectrogram technique is 1.25 *GHz* or 10 *pm*, which is largely sufficient for sampling at the Nyquist frequency at 10 *GHz*.

In the intrinsically self referenced SHG-FROG setup, the optical gate is optimally tailored to the pulse. This is not the case in the linear spectrogram setup. Here, we are limited by the bandwidth of the electronics available in our laboratory, currently 20 GHz. By using a high bandwidth photo-diode followed by a broad-band amplifier, we are able to create an electrical pulse with a duration of 30 ps. When this pulse drives the electro-absorption modulator (here: Corning EAM-P n.MV2276A12.20), it can create an optical transmission window of 10 to 16 ps duration, when the bias is varied between $-6.5\ V$ and $-4\ V$ respectively. Dorrer *et al.* have demonstrated that it is possible to characterise a 900 fs pulse when 'sampling' with a 30 ps long gate [39]. However, a shorter gating window that is of comparable duration to the pulse under test is generally preferable, because this makes the spectrogram more compact and easier to deconvolve.

The retrieved information of three different pulse streams have been examined closely: 33 ps long MZM carved pulses, 5 ps linearly compressed gain switched laser pulses and 2 ps actively mode locked ring laser pulses. The reader is referred to the following chapters for more detailed information about these particular pulse sources.

Figure 2.11 summarises the results, displaying the spectrograms for both techniques, and their respective retrieved pulse intensity and phase profiles in the temporal domain and the spectral domain.

The SHG-FROG spectrogram error (see equation 2.37) for the narrow bandwidth MZM carved pulses is 0.05, an order of magnitude higher than the 0.005 error in the linear spectrogram. This is due to the undersampling of the spectral slices in the SHG-FROG trace. Compared to the spectrum measured with an optical spectrum analyser, the intensity retrieved from the linear spectrogram agrees much better than the SHG-FROG retrieved intensity.
To quantify the effect of this spectral mismatch on the retrieved temporal intensity, the retrieved spectral intensity is replaced with the measured spectral intensity and the resulting complex field is numerically Fourier transformed to calculate the complex temporal field. The resulting mismatch in the time domain is then quantified by calculating the rms error between the calculated pulse intensity and the original retrieved pulse intensity. The SHG-FROG measurement gives an error of 0.1, compared to an error of 0.033 for the linear spectrogram. The SHG-FROG is not able to correctly measure these pulses because the spectral resolution of the 0.5 m spectrometer employed in this setup is insufficient to completely resolve the

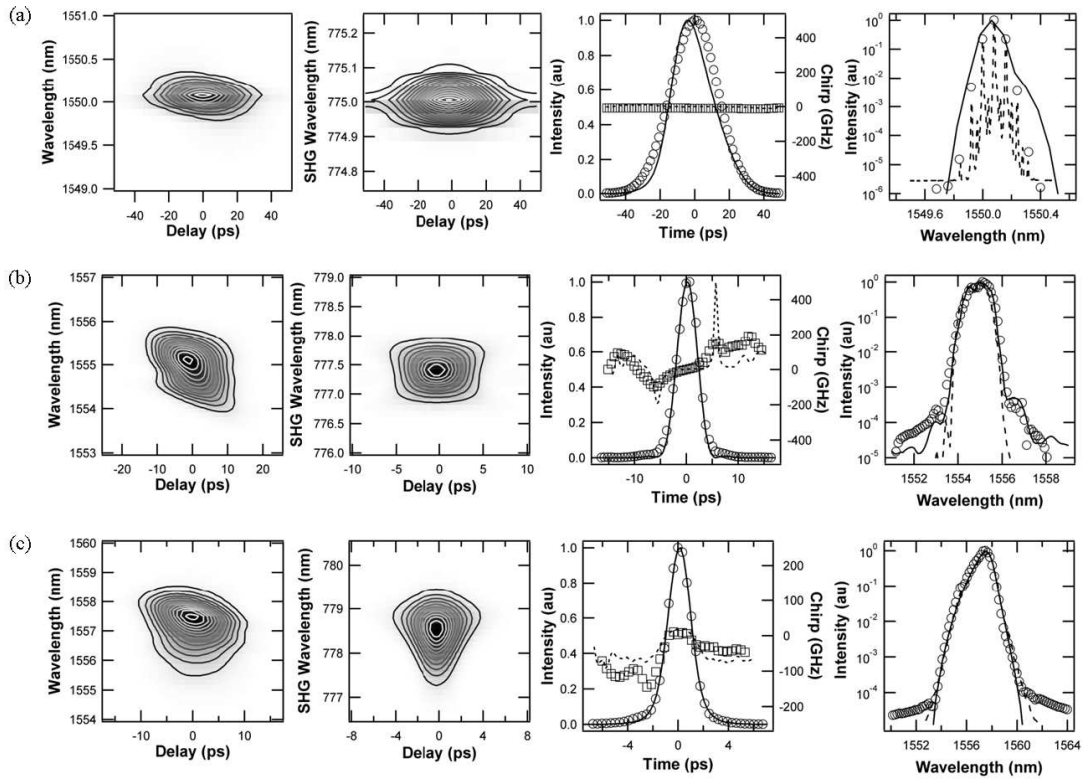

FIGURE 2.11: Linear-spectrogram and SHG-FROG results for 10-*GHz* pulses of durations (a) 32, (b) 5, and (c) 2 *ps*. The columns show (from left to right) the measured linear and SHG-FROG spectrograms, the retrieved temporal intensity and chirp (Linear: circles and squares; SHG-FROG: solid and dashed lines) and the retrieved spectral intensity chirp (Linear: circles; SHG-FROG: solid line) compared to the independently measured spectrum (dotted line).

SHG signal. While this is not an intrinsic limitation of the SHG-FROG technique as it can be resolved by increasing the resolution of the spectrometer, the increase in required real estate and complexity makes this unattractive.

The spectrogram retrieval errors for the measurements on the 5 *ps* and 2 *ps* long pulses is smaller than 0.005 for both the SHG-FROG technique as well as the linear spectrogram. Also the agreement between the independently measured spectrum and the retrieved spectrum is very good in both cases. The rms error in the temporal intensity arising from the mismatch between the retrieved spectrum and the measured spectrum for the 5 *ps* gain switched pulse is 0.015 and 0.004 and for the 2 *ps* ring laser pulse 0.008 and 0.005 for the SHG-FROG and the linear spectrogram respectively. While the SHG-FROG spectrogram is still undersampled spectrally, the broader spectral bandwidth of these shorter pulses reduces the effects of the undersampling.

Another way of interpreting this is that these short pulses generate SHG-FROG

spectrograms with a shorter temporal reach; the intensity essentially falls to zero outside of a temporal interval $[-10, 10]$ *ps* for the gain switched pulses and $[-8, 8]$ *ps* for the ring laser pulses. The spectrograms can be cropped temporally, increasing the Nyquist frequency, which means that the required spectral resolution is relaxed. The linear spectrograms, on the other hand, cannot be cropped without distorting the spectrogram as the extinction ratio obtained with the sampling EAM is not infinite and there is still significant intensity at the edges of the spectrogram. The resolution of the optical spectrum analyser is already sufficient though, and makes it possible to retrieve the information for the whole period of the pulse (and the gate).

Whilst the linear spectrograms deliver accurate pulse information for the three different pulse durations investigated here, the SHG-FROG fails to deliver correct information for the longer pulses, due to the limited resolution of the spectrometer. Furthermore, it is only because of the limited sensitivity of the spectrometer in the SHG-FROG setup that the spectrogram can be cropped to a duration shorter than the real pulse period. Note though that this is sufficient for many clean pulse sources, with insignificant amounts of energy in the pulse's wings.

2.7 Conclusions

The great interest in complete pulse characterisation has led to a rapidly evolving landscape in short pulse measurement techniques over the recent years. Spectrographic techniques in particular, such as the ones described in this chapter, are now quickly becoming essential tools in any optical telecommunications lab, and this area of research is still very much active.
In this chapter I have explained a frequently used implementation of frequency resolved optical gating (SHG-FROG), and compared it with the linear spectrogram method based on sampling with an electro-absorption modulator.
As already indicated here, the linear method is suitable for characterising a whole range of optical pulses in the optical telecommunications area. In the following chapters, I will frequently rely on the versatility of this technique to characterise a whole range of optical waveforms. Even though the information gained by these advanced pulse characterisation schemes is *complete*, they do not immediately replace the conventional methods of assessing optical waveform properties, such as photo detectors followed by electric sampling oscilloscopes, optical spectrum

analysers and autocorrelators. Acquisition speed is one limiting factor here, but real-time implementations are already being built commercially. Other factors are that they can generally only be applied to a limited wavelength region, and need substantial configuration before the acquisition of the spectrograms can be started as the time *and* frequency domain have to be considered.
Ultimately, these detailed characterisations should lead to a better understanding of various detrimental effects in optical networks. The performance of which is naturally determined by the bit error rates. Appendix A explains some of the work I have performed to implement an accurate way of assessing the Q-factor based on BER measurements.

References

[1] I. Walmsley and V. Wong, "Characterization of the electric field of ultrashort optical pulses," Journal of the Optical Society of America B (Optical Physics) **13**, 2453 – 63 (1996).

[2] F. Parmigiani, P. Petropoulos, P. Almeida, M. Ibsen, J. Lee, and D. Richardson, "A direct assessment of the performance of pulse shaping superstructured fiber gratings using an optical sampling oscilloscope," Optical Fiber Communications Conference (OFC) **1**, 40 – 2 (2003).

[3] M. Westlund, P. Andrekson, and H. Sunnerud, "High performance all-optical waveform sampling for fiber communication systems," 31st European Conference on Optical Communication **4**, 937 – 40 (2005).

[4] M. Westlund, P. Andrekson, H. Sunnerud, J. Hansryd, and J. Li, "High-performance optical-fiber-nonlinearity-based optical waveform monitoring," Journal of Lightwave Technology **23**, 2012 – 22 (2005).

[5] J.-C. Diels, J. Fontaine, I. McMichael, and F. Simoni, "Control and measurement of ultrashort pulse shapes (in amplitude and phase) with femtosecond accuracy," Applied Optics **24**, 1270 – 82 (1985).

[6] R. Trebino, "SC155: The Measurement of Ultrashort Laser Pulses," Frontiers in Optics 2005, Tucson, Short course notes (2005).

[7] L. Cohen, "Time-frequency distributions - A review," Proceedings of the IEEE **77**, 941 – 981 (1989).

[8] C. Dorrer and I. Kang, "Complete temporal characterization of short optical pulses by simplified chronocyclic tomography," Optics Letters **28**, 1481 – 3 (2003).

[9] C. Dorrer, N. Belabas, J.-P. Likforman, and M. Joffre, "Spectral resolution and sampling issues in Fourier-transform spectral interferometry," Journal of the Optical Society of America B (Optical Physics) **17**, 1795 – 802 (2000).

[10] L. Lepetit, G. Cheriaux, and M. Joffre, "Linear techniques of phase measurement by femtosecond spectral interferometry for applications in spectroscopy," Journal of the Optical Society of America B (Optical Physics) **12**, 2467 – 74 (1995).

[11] C. Iaconis and I. Walmsley, "Spectral phase interferometry for direct electric-field reconstruction of ultrashort optical pulses," Conference on Lasers and Electro-Optics Europe - Technical Digest p. 518 (1998).

[12] C. Dorrer and I. Kang, "Highly sensitive direct characterization of femtosecond pulses by electro-optic spectral shearing interferometry," Optics Letters **28**, 477 – 9 (2003).

[13] J. Debeau, B. Kowalski, and R. Boittin, "Simple method for the complete characterization of an optical pulse," Optics Letters **23**, 1784 – 6 (1998).

[14] B. Kowalski, J. Debeau, and R. Boittin, "A simple and novel method for measuring the chirp parameter of an intensity modulated light source," IEEE Photonics Technology Letters **11**, 700 – 2 (1999).

[15] M. van Deventer, C. de Blok, and C. Park, "High-dynamic-range heterodyne measurement of optical spectra," Optics Letters **16**, 678 – 80 (1991).

[16] D. Reid, "Algorithm for complete and rapid retrieval of ultrashort pulse amplitude and phase from a sonogram," IEEE Journal of Quantum Electronics **35**, 1584 – 9 (1999).

[17] I. Cormack, W. Sibbett, R. Ortega-Martinez, and D. Reid, "Ultrashort pulse characterization using a scanning Fabry-Perot etalon enabling rapid acquisition and retrieval of a sonogram at rates up to 1.52 Hz," Review of Scientific Instruments **72**, 4071 – 9 (2001).

[18] S. Linden, H. Giessen, and J. Kuhl, "XFROG-a new method for amplitude and phase characterization of weak ultrashort pulses," Physica Status Solidi B **206**, 119 – 24 (1998).

[19] C. Dorrer and I. Kang, "Simultaneous temporal characterization of telecommunication optical pulses and modulators by use of spectrograms," Optics Letters **27**, 1315 – 17 (2002).

[20] E. Zeek, A. Shreenath, M. Kimmel, and R. Trebino, "Calibrating and removing the direction of time ambiguity in FROG," Technical Digest. Summaries of papers presented at the Conference on Lasers and Electro-Optics **1**, 357 – 8 (2002).

[21] R. Trebino, K. DeLong, D. Fittinghoff, J. Sweetser, M. Krumbugel, B. Richman, and D. Kane, "Measuring ultrashort laser pulses in the time-frequency domain using frequency-resolved optical gating," Review of Scientific Instruments **68**, 3277 – 95 (1997).

[22] P. O'Shea, M. Kimmel, X. Gu, and R. Trebino, "Highly simplified device for ultrashort-pulse measurement," Optics Letters **26**, 932 – 4 (2001).

[23] S. Akturk, M. Kimmel, P. O'Shea, and R. Trebino, "Measuring pulse-front tilt in ultrashort pulses using GRENOUILLE," Optics Express **11** (2003).

[24] S. Akturk, X. Gu, and R. Trebino, "Measuring the intensity and phase of 1.5-μm ultrashort laser pulses," 31st European Conference on Optical Communication **3**, 399 – 402 (2005).

[25] K. DeLong, R. Trebino, and W. White, "Simultaneous recovery of two ultrashort laser pulses from a single spectrogram," Journal of the Optical Society of America B (Optical Physics) **12**, 2463 – 6 (1995).

[26] C. Dorrer and I. Kang, "Real-time implementation of linear spectrograms for the characterization of high bit-rate optical pulse trains," IEEE Photonics Technology Letters **16**, 858 – 60 (2004).

[27] C. Dorrer and I. Kang, "Real-time characterization of short optical pulse using spectrograms," Optical Fiber Communications Conference (OFC) **1**, 99 – 100 (2003).

[28] D. Kane, "Recent progress toward real-time measurement of ultrashort laser pulses," IEEE Journal of Quantum Electronics **35**, 421 – 31 (1999).

[29] D. Fittinghoff, K. DeLong, R. Trebino, and C. Ladera, "Noise sensitivity in frequency-resolved optical-gating measurements of ultrashort pulses," Journal of the Optical Society of America B (Optical Physics) **12**, 1955 – 67 (1995).

[30] D. Kane, F. Omenetto, and A. Taylor, "Convergence test for inversion of frequency-resolved optical gating spectrograms," Optics Letters **25**, 1216 – 18 (2000).

[31] P. Honzatko, J. Kanka, and B. Vrany, "Retrieval of the pulse amplitude and phase from cross-phase modulation spectrograms using the simulated annealing method," Optics Express **12** (2004).

[32] J. Nicholson, F. Omenetto, D. Funk, and A. Taylor, "Evolving FROGS: phase retrieval from frequency-resolved optical gating measurements by use of genetic algorithms," Optics Letters **24**, 490 – 2 (1999).

[33] M. Krumbugel, D. Fittinghoff, K. Delong, and R. Trebino, "Direct ultrashort-pulse retrieval in frequency-resolved optical gating using wavelets and a neural network," Proceedings of the SPIE - The International Society for Optical Engineering **2701**, 171 – 5 (1996).

[34] M. Krumbugel, C. Ladera, K. DeLong, D. Fittinghoff, J. Sweetser, and R. Trebino, "Direct ultrashort-pulse intensity and phase retrieval by frequency-resolved optical gating and a computational neural network," Optics Letters **21**, 143 – 5 (1996).

[35] M. Wang, T. Li, and S. Jian, "Tunable PMD compensator based on high-birefringence linearly chirped FBG with cantilever beam," Optics Express **11** (2003).

[36] K. DeLong and R. Trebino, "Improved ultrashort pulse-retrieval algorithm for frequency-resolved optical gating," Journal of the Optical Society of America A (Optics, Image Science and Vision) **11**, 2429 – 37 (1994).

[37] B. Seifert, H. Stolz, and M. Tasche, "Nontrivial ambiguities for blind frequency-resolved optical gating and the problem of uniqueness," Journal of the Optical Society of America B (Optical Physics) **21**, 1089 – 97 (2004).

[38] B. Thomsen, M. Roelens, R. Watts, and D. Richardson, "Comparison between nonlinear and linear spectrographic techniques for the complete characterization of high bit-rate pulses used in optical communications," IEEE Photonics Technology Letters **17**, 1914 – 16 (2005).

[39] C. Dorrer, "Investigation of the spectrogram technique for the characterization of picosecond optical pulses," 2005 Optical Fiber Communications Conference Technical Digest **2** (2005).

Chapter 3

Pulse Generation

3.1 Introduction

The stringent requirements on various aspects of pulses, and their respective modulation formats, have forced research groups across the world to look into many different ways of generating optical pulses that are: first of all short enough to enable very high repetition rates; and secondly capable of providing conditioned pulses with a good extinction ratio, both temporally and spectrally, exhibiting low timing jitter, and preferably transform limited characteristics. Two low-cost ways of generating short optical pulses suitable for optical telecommunication are studied in this chapter: gain switching of a semiconductor laser, and pulse carving with an electro-absorption modulator.

State-of-the-art electronics nowadays make it feasible to implement full electronic TDM transmitter and receiver subsystems with data rates of up to 85 $Gbit/s$ [1]. Economics and physics currently present major obstacles to a further increase of speeds reachable with electronics. All-optical processing delivers a solution for many areas where electronics cannot follow the demand for higher bandwidth.

In our lab, we currently start at an electronic base rate of 10 $Gbit/s$, which means that the time slot (period) of one bit is 100 ps long. Using an optical interleaver (as described in Appendix C), it is possible to perform measurements at bit-rates higher than the electrical repetition rates available, and thus to overcome some of the limits imposed by electronics. The bit period is inversely proportional to the bit rate so with aggregate bit rates of 40, 80 and 160 $Gbit/s$, the bit slot

becomes 25, 12.5 and 6.25 *ps* long respectively. To enable these high bit rates, the pulses have to become shorter accordingly - assuming single polarisation, single wavelength binary transmission.

Modulation formats

There are two basic ways of using the time slot for transmitting data through intensity modulation. The first one is return to zero (RZ), in which the signal always returns to a rest state (i.e. zero) during a portion of the bit period. The second possibility is non-return to zero (NRZ), where the signal level can only make a transition at the borders of the bit period when the bit value changes. For a given bit period, the bandwidth of an RZ signal will thus be broader than that of an NRZ signal. However, RZ pulses are advantageous as they allow for passive optical interleaving to higher aggregate bit rates. RZ also becomes less sensitive to nonlinearities and dispersion than NRZ for bit rates of 40 $Gbit/s$ and higher [2, 3, 4].

Many variations on these two basic formats exist, and a good overview can be found in Ref. 5. Peter Winzer gives an interesting summary, including a classification of the different formats in his short course "Modulation Formats and Receiver Concepts for Optical Transmission System" [6], regularly featuring at the major conferences on optical communications (e.g. OFC and ECOC).

Over recent years, interest has grown in exploiting the phase properties of pulses in addition to the pulse amplitude – in particular the relative phases between neighbouring pulses. The goal is to combine the positive properties of phase modulation with amplitude modulation. More details about one of these advanced formats, called alternating phase, return to zero APRZ, are presented in Chapter 5, together with setups used to generate these pulses, and the particular advantages or disadvantages of the format itself.

The initial scope of this thesis was an investigation into high bit-rate optical communication systems in general. These systems require highly specialised pulse sources that are compatible with the short bit slots. Both the exact phase/chirp and intensity profiles of the pulses used here are very important from this perspective. The propagation of the pulses in dispersive and nonlinear media is strongly

influenced by the pulse properties, and requires a thorough investigation to assess their suitability in high speed optical networks. This explains the particular attention I have paid to accurate characterisation of various waveforms in this work.

Pulse sources

The first of the sources I investigated was a gain switched laser diode. The principles of operation, characterisations and several optimisation schemes will be explained in Section 3.2. This section starts with an introduction to the principle of gain switching, after which I investigate the pulses generated with laser diodes operating in the $1.5\mu m$ region. This includes the chirp characterisation, and how this information can be used to generate cleaner pulses.
These pulses have been used as the seed in a high power amplification experiment, which will briefly be described in Section 3.2.3. Recently, we have also been able to perform very similar measurements at 1060 nm. The preliminary results here too are very promising and are described briefly in Section 3.2.4.

Another way of generating pulses is by amplitude modulating a continuous wave (CW) laser beam. The common modulators used to do this in the 1550 nm region are electro-absorption modulators (EAMs) and $LiNbO_3$ (lithium niobate) Mach-Zehnder modulators. Because of the particular relevance of electro-absorption modulators in the rest of this thesis, they are investigated more in detail in Section 3.3. Related to the APRZ format, I will describe a series of measurements based on $LiNbO_3$ modulators for high speed transmission systems in Chapter 5.

3.2 Gain Switched Laser Diode

The principle of gain switching in semiconductor lasers was first demonstrated by Ito *et al.* in 1979 [7, 8]. Using this technique, an optical pulse can be created with a pulse duration which is much less than the electrical pulse used to drive the laser diode.

The setup we use for gain switching a distributed feedback (DFB) laser diode is shown in Figure 3.1. The semiconductor laser is initially biased just below threshold (see Figure 3.2), giving a low photon density. When a high current is

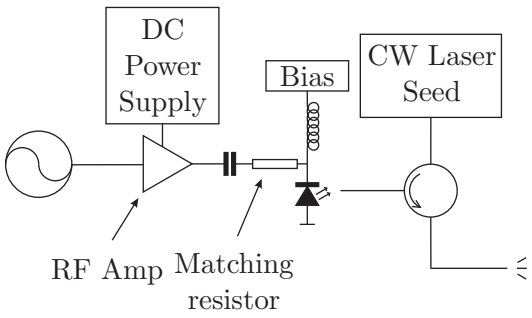

FIGURE 3.1: Scheme of the transmitting laser.

then applied to the device, the carrier density increases and exceeds the lasing threshold level. Through stimulated emission, a large number of photons are generated. During this process, the carrier density is rapidly depleted. The lasing is halted when the carrier density falls back to below threshold. If the injection current is reduced to a low level before threshold is reached again (relaxation oscillations), this process produces a single pulse which is much shorter than the electrical driving pulse.

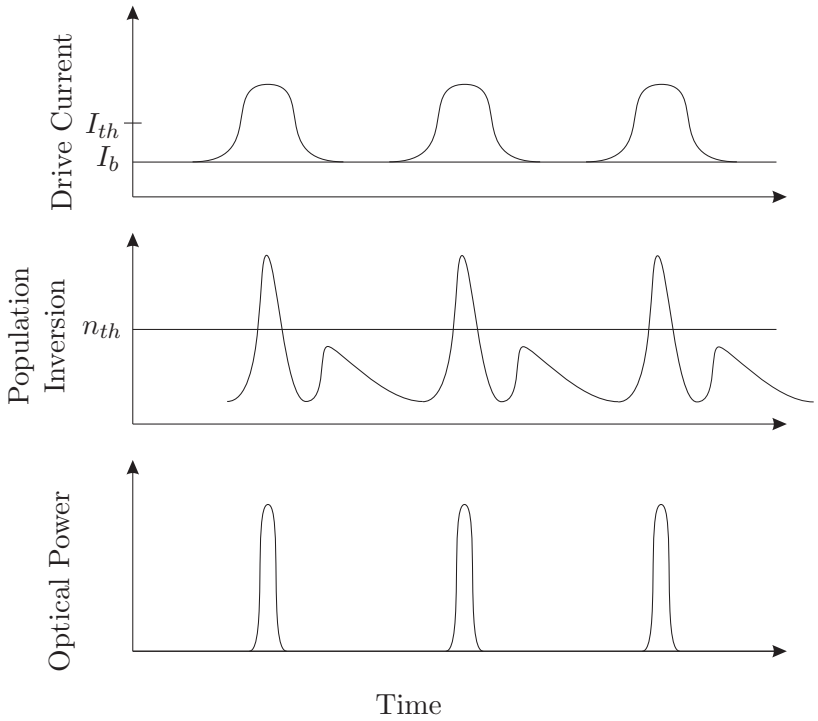

FIGURE 3.2: Gain switching laser time characteristics.

Due to the random nature of spontaneous emission, from which the pulse develops, the timing jitter between the pulses can be very high. However, when the pulse is forced to develop in a stimulated way, e.g. by seeding it with a continuous wave

source, such as a CW laser, with better defined optical phase properties, this timing jitter can be reduced by about 60 % [9]. This process is called external seeding. The external seed can be injected into the DFB laser, using an optical circulator or a 50/50 coupler.
Varying the seeding power, wavelength and polarisation affects the pulse length and side mode suppression ratio (SMSR). In Section 3.2.1, I will investigate the optimal seed wavelength and powers through a full characterisation of the pulses. Seo *et al.* have investigated the dependence on the injection power and wavelength [9], and concluded that the *optimum power* is determined by a trade-off between low timing jitter/high SMSR, and short pulse durations. Similar conclusions can be drawn from measurements performed with the laser diode used throughout this work. However, I have found, based on the complete characterisation of the pulses using linear spectrograms, that the wavelength of the seeding laser can significantly alter the pulse generation process, as will be explained in Section 3.2.1.

Self-seeding has also been suggested as a mechanism to reduce the timing jitter [10]. According to this approach, a fraction of the signal generated by the laser diode is sent back into the device after having travelled some distance outside the cavity. Ideally, the reflected pulse must arrive back in the laser cavity during the narrow time window just as the carrier density reaches threshold. This will select the longitudinal mode, and allows the pulse to develop in a stimulated way. This of course cancels the advantage of the variable repetition rate of the gain switched laser, as the distance the pulse has to travel outside the cavity before returning to seed the next pulse, will vary with the repetition rate. However, it does make for an easier and cheaper implementation.

We looked to circumvent this problem by using a weak narrow band FBG which could reflect a smeared out replica of the pulse back to the cavity. If the reflected pulse is sufficiently stretched out in time, it could mimic the behaviour of an external CW seed. Figure 3.3 shows the configuration for a FBG self seeded gain switched laser. Together with a specially designed grating for compensation of the chirp on the pulses, as explained later on in Section 3.2.2, the practical implementation of this very short and versatile pulse source can become very compact.

Direct intensity modulation of semiconductor lasers is accompanied by phase modulation, due to changes in the carrier densities and resultant changes in the refractive index of the cavity. This means that the pulses generated by gain switching a

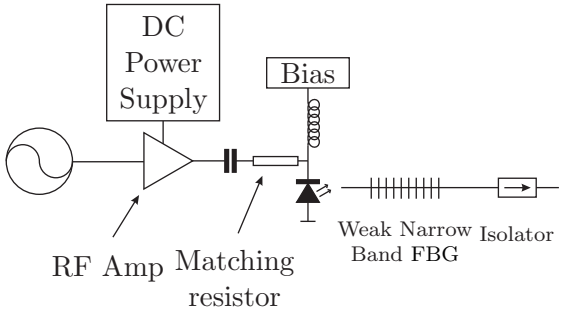

FIGURE 3.3: Self seeded gain switched laser using a FBG.

semiconductor laser carry a considerable amount of chirp. The down-chirp (i.e. the instantaneous frequency of the pulse reduces over time) observed on gain switched laser pulses is close to linear, with the carrier density quickly reducing at the moment of pulse generation. Linear chirp can be compensated through propagation in dispersive fibre, or with linearly chirped gratings. However, with a specially designed fibre Bragg grating, it is even possible to compensate for the nonlinear chirp to create a clean, transform limited pulse. This will be explained in Section 3.2.2.

3.2.1 Measurements on C-band gain switched laser diodes

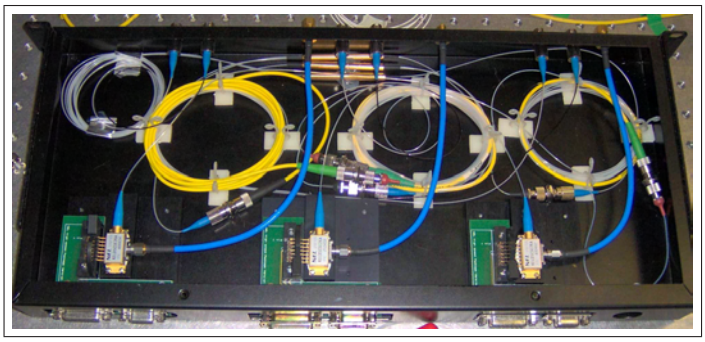

FIGURE 3.4: Photo of 3 C-band semiconductor laser diodes, in a setup ready for gain switching, including external seeding.

The NEL KELD5C5E2KA DFB semiconductor laser diodes are the base components in the 5 units which we have constructed, ready for gain switching. The diodes have nominal central wavelengths between 1540 nm and 1560 nm with 5 nm interspacing. By temperature tuning the cavities of these laser diodes, we can reach virtually any wavelength between 1538 nm and 1562 nm, largely sufficient for C-band experiments. A picture of a box with three of these units is shown in Figure 3.4. All of the measurements shown below have been performed

with the 1555 nm diode. The conclusions are valid for all of the diodes.
To determine the optimal working regime and to better understand the influence of the different parameters, I measured and deconvolved a series of spectrograms, characterising the pulse properties as a function of seeding wavelength and power. The bias current was set at 60 mA (with a forward voltage of 1.08 V), and the RF port driven with a 29 dBm RF sinusoid. These parameters only need minor adjustment in the instance for example that the cavity temperature is changed to obtain slightly higher or lower wavelengths (± 1 nm around the specified nominal wavelength).

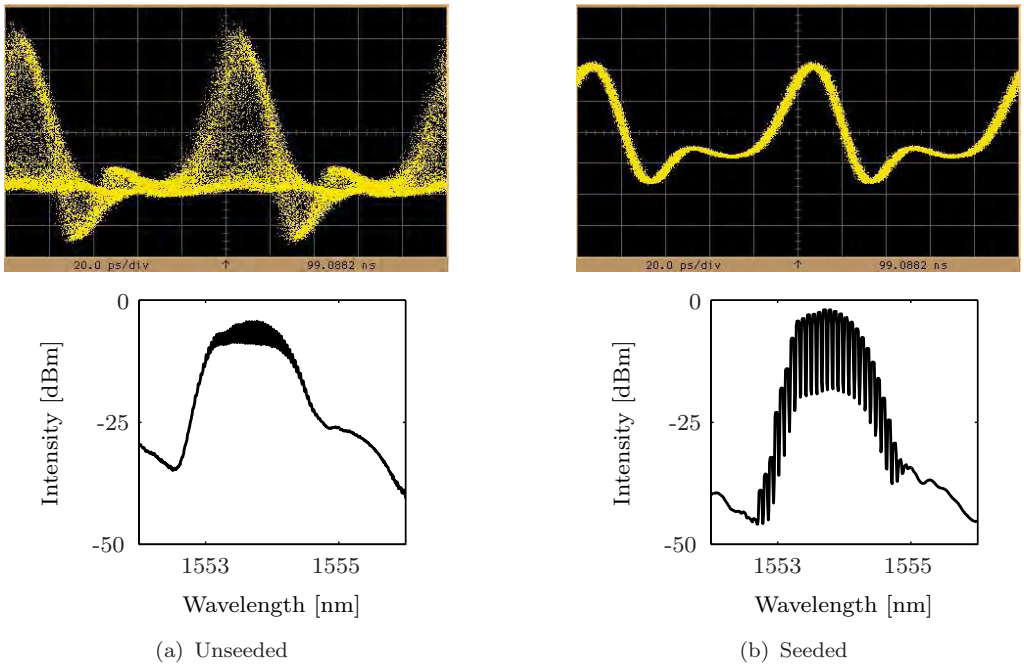

(a) Unseeded (b) Seeded

FIGURE 3.5: Electrical oscilloscope traces (top) of both unseeded and seeded gain switched laser pulses, together with their respective spectra (bottom).

Figure 3.5 shows oscilloscope traces of the gain switched laser pulses with and without external seeding. It is clear that some form of seeding within the cavity is needed to lock the generated mode to the desired wavelength, and at the same time reduce the significant amount of timing jitter (down to less than 800 fs, measurement limited by the resolution of the sampling oscilloscope) and amplitude noise apparent in Figure 3.5(a). The bottom plots show the equivalent in the spectral domain: the 10 GHz spectral lines are hardly visible without seeding – a clear indication of significant timing and amplitude jitter. There is a 15 dB better contrast between the main mode and the longitudinal side modes when the gain switched laser is externally seeded.

3.2.1.1 Spectrogram

A typical experimental EAM-spectrogram (see 2.4) of an externally seeded gain switched laser is shown in Figure 3.6. The same spectrogram after envelope detection, background noise removal and interpolation on a 64×64 point Fourier grid is shown in Figure 3.7, next to the reconstructed spectrogram, for comparison. When the gain switched laser is appropriately seeded (see further), the pulses are in phase and have a significantly reduced amount of timing jitter. However, the adjacent longitudinal cavity modes are still not fully suppressed. These modes are not in phase with the main mode, as can be seen in the spectrum, Figure 3.8 (measured with an optical spectrum analyser, with a resolution of 10 pm), since there are no 10 GHz spectral interference lines visible on the sidemodes. The spectral intensity, retrieved from the spectrogram is also shown in Figure 3.8. There is very good spectral agreement with the independently measured spectrum over 4 orders of magnitude.

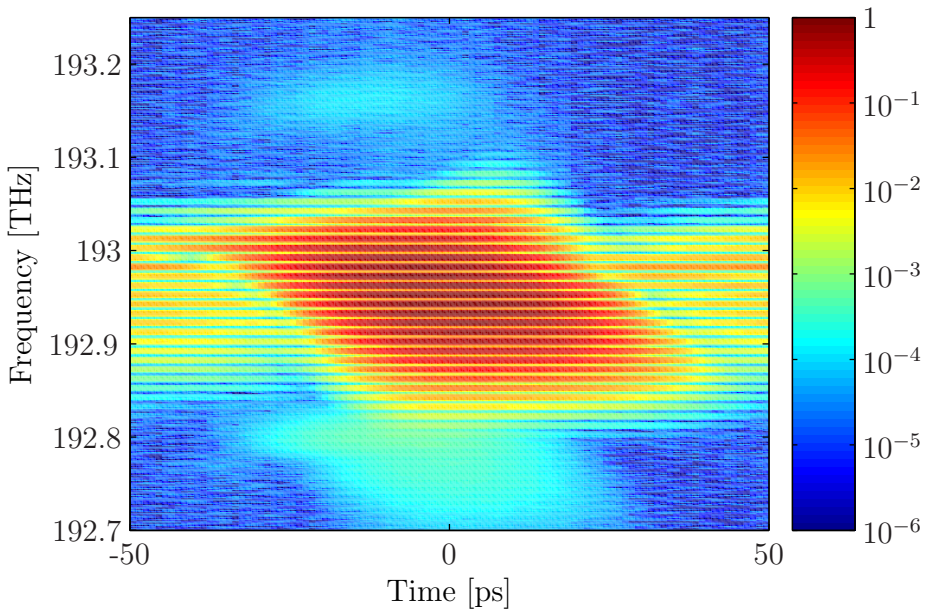

FIGURE 3.6: Unprocessed measured spectrogram of an externally seeded gain switched laser pulse ($\lambda_{seed} = 1553.5\ nm$, seed power= $-10\ dBm$).

However, because there is no well defined phase relationship between the main lasing mode and the sidemodes, they do not contribute constructively or destructively to temporal features of the pulse. This makes it impossible to perfectly reconstruct the spectrogram: the reconstruction method intrinsically assumes only coherent

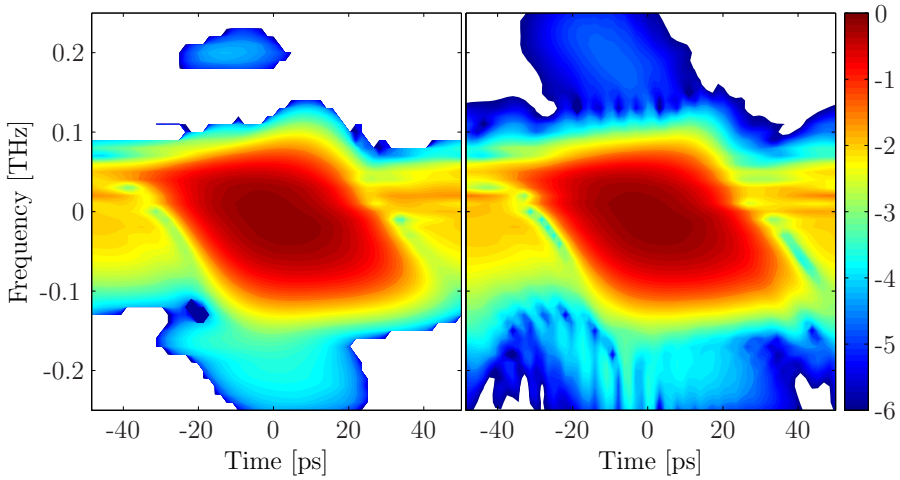

FIGURE 3.7: Measured and interpolated (left) and reconstructed (right) spectrogram of gain switched laser pulses.

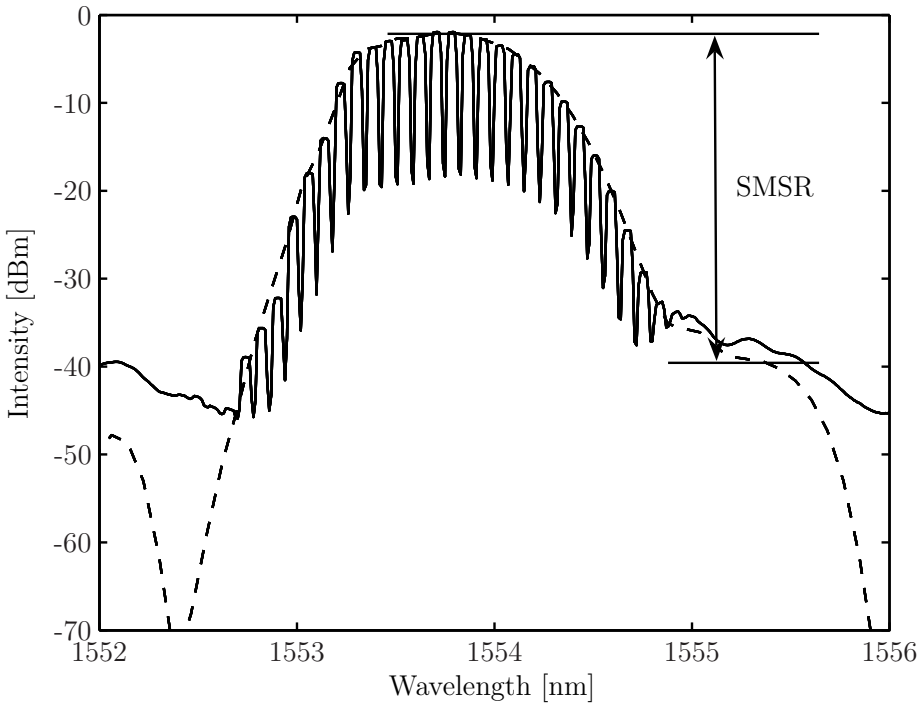

FIGURE 3.8: Spectrum measured with an optical spectrum analyser (full line) and spectrum retrieved from the FROG deconvolution algorithm (dashed line).

information. As can be seen in Figure 3.7, the reconstruction incorporates semi-periodic intensity features that do not occur in the original spectrogram. These features are merely there because that is the closest solution the retrieval algorithm can find whilst looking for pulses that make the spectrogram match both in the spectral and the temporal domain.

Note however that these sidemodes are about 40 dB down on the main mode, and therefore most of the relevant pulse information is contained in the main mode in any event. In other words, the presence of sidemodes does not dramatically affect the quality of the retrieved pulse information. This will be confirmed by numerical simulations further on in this section.

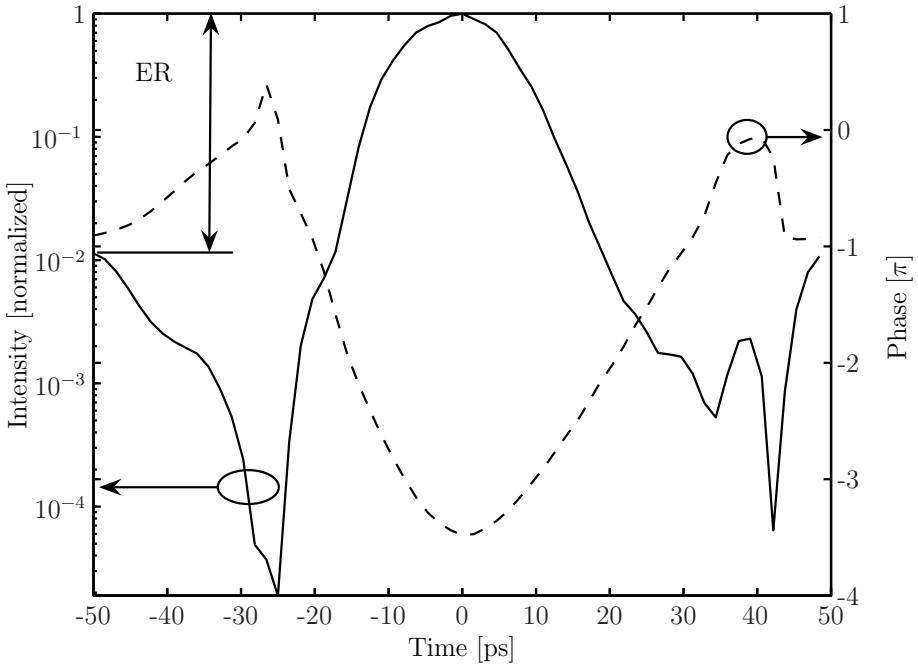

FIGURE 3.9: Intensity (full line, logarithmic scale) and phase (dashed line) of the gain switched laser pulse, retrieved from the spectrogram in Figure 3.6.

The temporal information retrieved from the spectrogram is shown in Figure 3.9. There is a clear parabolic phase profile noticeable where there is significant pulse intensity. This corresponds to a pulse with a linear chirp profile.

3.2.1.2 Seed power

Figures 3.10i a, b and c display the pulse duration (FWHM), the temporal extinction ratio (ER) and the spectral sidemode suppression ratio (SMSR) versus the

power (in dBm) of the seed wavelength, for both with and without propagation over 125 m of dispersion compensating fibre (DCF) (this length of fibre was calculated by solving the nonlinear Schrödinger equation (NLSE), as will be explained in Section 3.2.2). How the SMSR and ER are measured is shown in Figures 3.8 and 3.9. The information is measured on the retrieved pulse profiles.

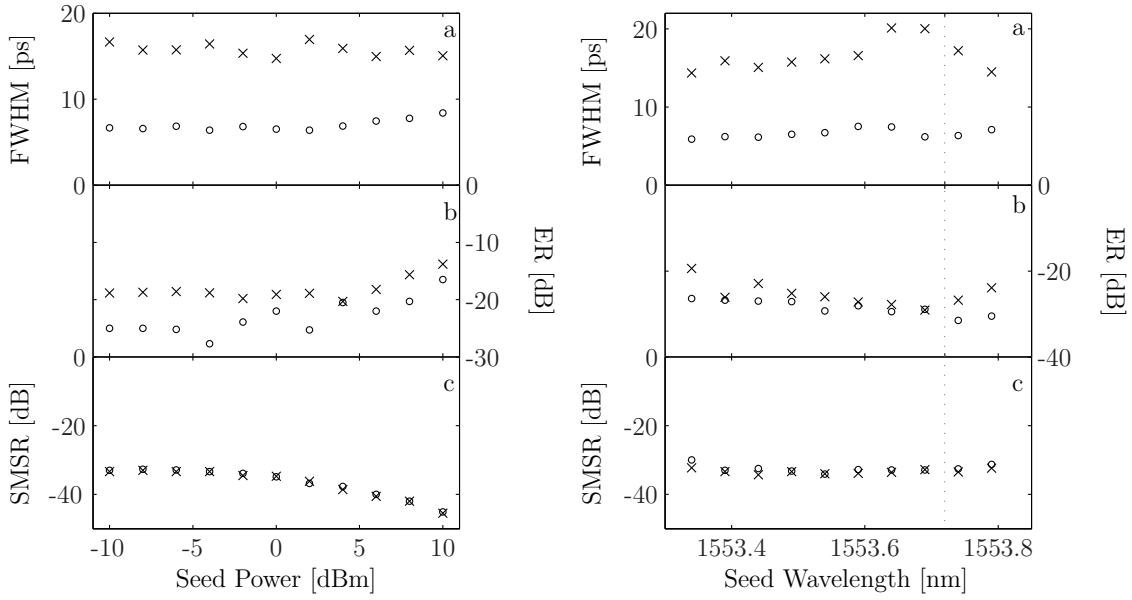

(i) Power dependence, seed wavelength: 1553.41 nm (ii) Wavelength dependence, seed power: -10 dBm

FIGURE 3.10: Pulse duration (FWHM), temporal extinction ratio (ER) and sidemode suppression ratio (SMSR) versus seed power (left, $\lambda_{seed} = 1553.41\ nm$) and wavelength (right, seed power= $-10\ dBm$). The dashed vertical line indicates the central wavelength of the pulse (1553.72 nm). Crosses ($\times$) are measurements on original gain switched pulses, circles ($\circ$) denote measurements of the pulses compressed through propagation over 125 m of DCF.

The fact that there is as good as no difference between the SMSR before and after propagation means that, as expected, the pulses propagate linearly over the fibre, without changing their spectrum. The SMSR improves with higher seeding powers, meaning that more of the generated photons are locked into the main lasing mode. At the same time, this increased seeding power slightly reduces the bandwidth of the pulses. The consequence of this is noticeable in terms of pulse length: the pulse duration after compression gets longer with increased seeding powers, as shown in Subfigure 3.10i(a). Also the extinction ratio gets worse with higher seed powers. All together, this means there is a trade off between good temporal characteristics (short pulses, good extinction ratio) and good spectral sidemode suppression ratio. In the lab, we usually run the gain switched laser

diodes with a minimal amount of seed power: -10 dBm, and thus optimising for shorter pulse durations rather than better sidemode suppression.

3.2.1.3 Seed wavelength

The results of a similar set of measurements versus seed wavelength is shown in the right hand side of Figure 3.10. Again, the SMSR of the pulses before and after propagation are nearly identical (max 2 dB difference on SMSRs of over 30 dB). However, in this case, the spectrograms become more complex when they are seeded with wavelengths that do not coincide with the initial wavelengths generated in the cavity. This makes the deconvolution a little more difficult, as the pulse shapes become more complex: when the sidemodes are not mathematically removed before the deconvolution, the retrieval algorithm gets easily trapped in a local minimum where it tries to relate the temporal intensity modulation to the sidemodes instead of the intensity feature emerging from seeding with a wavelength higher than the central wavelength of the pulse. The pulse even starts to break up when the seed wavelength overlaps with the red-wavelength side of the pulse.

On the other hand, the ER and the pulse duration *at half maximum* do not seem to be strongly affected by the exact seed wavelength. This is deceiving however, because the temporal pulse shape does get distorted and more power goes into the close pedestal of the pulse. This was not immediately measured as the extinction ratio. It is clear that these degraded pulse shapes are not desirable in transmission systems.

These conclusions are confirmed by a direct visual inspection of the spectrogram. Figure 3.11 shows the spectrogram and the retrieved pulse intensity for a gain switched pulse with central wavelength of 1553.72 nm and a seed wavelength of 1553.84 nm. An intensity feature develops with increasing seeding wavelength (lower frequency). This disrupts the ideal development of the pulse in the cavity, which normally chirps from lower to higher wavelengths. Due to the higher seed wavelength, there is an increased amount of red-shifted wavelengths at the onset of the pulse. The result is the emergence of a pre-pulse that corresponds to a slight dip in the middle of the spectrum.

The results above show that it is important to carefully consider the wavelength of the seed signal, if an optimised pulse is desired. The best way is to choose

a suitable seed wavelength by looking at the spectrum of the pulse. The ideal seed wavelength should be chosen as low as possible whilst still falling within the generated spectral bandwidth, and at the same time avoiding seeding the neighbouring side mode. When a dip develops in the middle of the spectrum (see Figure 3.11(iii)), the seed wavelength is too high, and the temporal profile of the pulse will be much less than ideal.

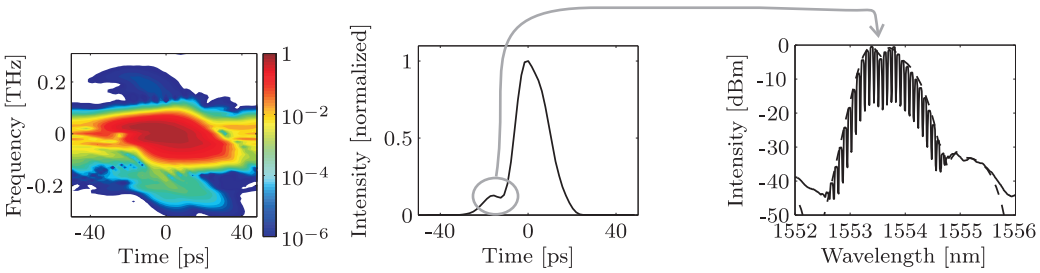

(i) Spectrogram (ii) Temporal intensity (iii) Spectral intensity

FIGURE 3.11: Spectrogram, retrieved temporal and spectral intensity profiles of the pulses with a higher seed wavelength (1553.840 *nm*).

3.2.2 Pulse Compression

The pulses generated with a gain switched (GS) laser diode are down-chirped. Chirp means essentially that the frequency of the pulse varies over the pulse duration. The instantaneous frequency chirp $\delta\nu(t)$ across the pulse is obtained by taking the derivative of the phase $\phi(t)$ with respect to time:

$$\delta\nu(t) = -\frac{1}{2\pi}\frac{d\phi(t)}{dt}. \tag{3.1}$$

3.2.2.1 Fibre based linear compression

Figure 3.12 clearly shows a negative chirp slope, meaning that the instantaneous frequency at the leading edge of the pulse is higher than the instantaneous frequency at the trailing edge of the pulse.
By slowing down these higher frequencies slightly with respect to the lower frequencies, the pulse can effectively be compressed in time. This method of compressing pulses has already been demonstrated frequently using DCF [11] and linearly chirped fibre Bragg gratings [12, 13, 14]. In a dispersion compensating fibre (with a negative dispersion around the 1550 *nm* region), the higher frequencies

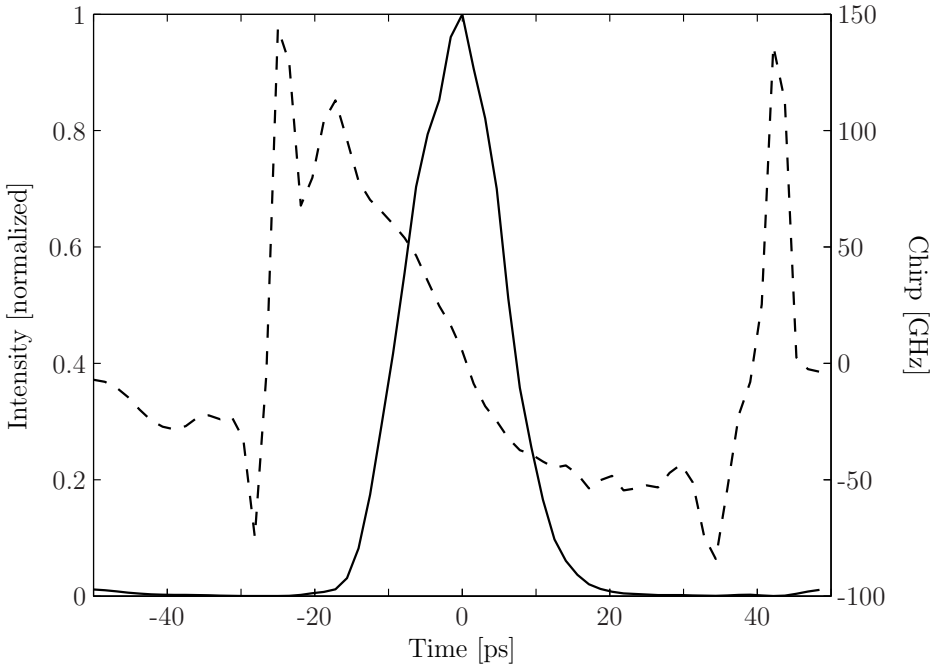

FIGURE 3.12: Intensity (full line) and chirp $\delta\nu(t)$ (dashed line) of the gain switched laser pulse, retrieved from the spectrogram in Figure 3.6.

travel slower than the lower frequencies. So, when the amount of chirp is known, the necessary length of DCF through which the pulse should be sent to compress optimally can be determined.

As can be seen in Figure 3.12, the chirp is not exactly linear over the duration of the pulse. Using a fibre, or a linearly chirped fibre Bragg grating would only compensate the linear component of this chirp. This has a detrimental effect on the pulse quality, as some of the intensity is not delayed sufficiently with regards to the maximum intensity of the pulse, and significant side pulses emerge. I will show later on that a specific fibre Bragg grating can be designed that compensates for this nonlinear chirp. In the next section however follow a few more results on compression with a dispersion compensating fibre.

3.2.2.2 Nonlinear Schrödinger Equation

Because the pulse is completely characterised, it is possible to feed the full waveform information into numerical simulations based on the NLSE, or commercial packages such as VPItransmissionmaker. The deconvolution algorithm is programmed in Matlab, and implementing a simple split-step Fourier method [15]

to solve the NLSE makes it possible to quickly simulate how the pulses would propagate over a fibre with given parameters.

The NLSE is used to model the propagation of the optical pulses through the fibre:

$$\frac{\partial A}{\partial z} + \frac{\alpha}{2}A + \frac{i\beta_2}{2}\frac{\partial^2 A}{\partial t^2} = i\gamma(|A|^2 A), \tag{3.2}$$

where $A(z,t)$ is the slowly varying pulse envelope, γ the nonlinear parameter and β_2 the group-velocity dispersion parameter related with the dispersion D (usually expressed in $ps/nm/km$) as follows:

$$D = -\frac{2\pi\beta_2 c}{\lambda^2}. \tag{3.3}$$

For example, the pulses are measured just after their generation. Numerical propagation simulations based on many measurements on the gain switched pulses with various driving conditions (V_{bias} and V_{pp}) show that the optimal length of DCF (D=-106$ps/nm/km$), in order to maximally compress the pulses by removing the linear chirp, varies between 90 m and 150 m, depending on the exact driving conditions of the gain switched laser (Figure 3.13). The best settings (in terms of pulse duration and reproducibility) were found to require an optimal length of around 125 m (I_{bias}=60 mA, V_{bias}=1.09 V, RF driving power: 29 dBm). Without the need for a trial-and-error approach we can now cut the desired length of fibre to optimally compress the pulses.

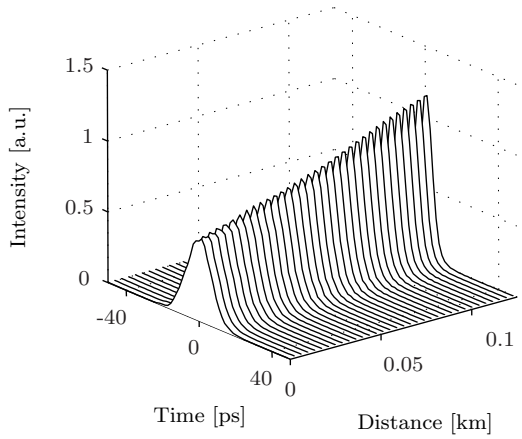

FIGURE 3.13: Pulse intensity evolution versus distance propagated over DCF.

The pulses are now measured again with the spectrogram technique after physical propagation over this chosen length of fibre. The results of the numerical and physical propagation are shown in Figure 3.14. As can be seen on these plots,

there is excellent agreement, both in the temporal and the spectral domain for over 4 orders of magnitude - note the logarithmic scale of the intensity axes. This is in itself an indirect confirmation of the accuracy of the spectrogram technique, and shows how powerful this method can be.

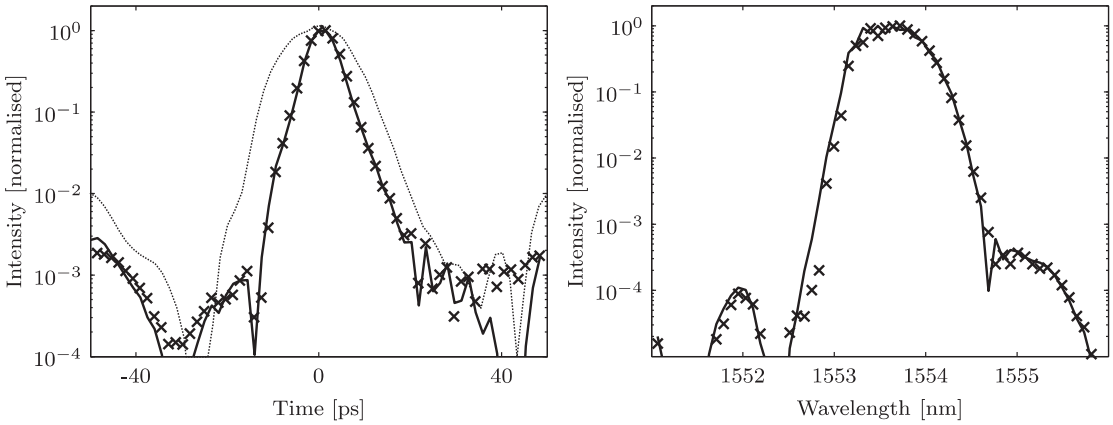

(i) Time domain (ii) Spectrum

FIGURE 3.14: Temporal and spectral intensity of gain switched laser pulses after propagation over 125 m of DCF, directly measured (full line) and from numerical simulation ($\times$) using the split step method on the original gain switched laser pulses (dotted line).

Starting from a pulse that is originally about 16 *ps* long, with a time-bandwidth product (TBP) of $\Delta t \Delta f = 1.48$, we obtained a 7 *ps* long pulse by removing the linear chirp with the dispersion compensating fibre. The time-bandwidth product becomes 0.69. A further decrease of the TBP is limited by the spectral shape of the pulse, which is fairly flat over the central wavelengths.

3.2.2.3 FBG based linear compression

The DCF can be replaced by a fibre Bragg grating (FBG) with a linear chirp profile, as explained by Ahmed *et al.* [12]. In a linearly chirped FBG, the different frequency components of the pulse get reflected at different points in the grating, and thus return with an adjusted relative delay. With the correct chirp profile, the pulse can in this way again be shortened while the chirp is eliminated.

Looking carefully at the chirp profile in Figure 3.12, it can be noticed that it is not completely linear over the region of interest. We note that an appropriately designed FBG can be used to impose an arbitrary spectral intensity profile and to compensate for both the linear and nonlinear chirp that is present on the pulses.

Design and fabrication techniques have become accurate enough to be able to make a FBG which can compensate also for a nonlinear chirp profile.

The characterisations of the pulses as shown above contain all the information needed to design the ideal grating to filter a transform-limited pulse out of a highly chirped gain switched laser pulse. The design of the FBG that will be used for compression is based on the retrievals of the pulse itself (spectral intensity profile: $I_{incident}(f)$). The group delay of the FBG is designed to perfectly compensate the measured group delay (the derivative of the phase in the spectral domain) of the optical pulse. At the same time, spectral filtering can be incorporated into the FBG. It turns out that the available spectrum generated by the gain switched laser best matches a Gaussian profile, compared to either a hyperbolic secant or a parabolic pulse profile for example. The reflection strength profile ($R(f)$) is designed so that the pulse reflected by the FBG is a perfect chirp free Gaussian ($G(f)$), in order to minimise the amount of lost power due to the filtering:

$$R(f) = G(f)/I_{incident}(f) \quad \Longrightarrow \quad I_{reflected}(f) = I_{incident}(f)R(f) = G(f). \quad (3.4)$$

The spectral width of the Gaussian is determined by the spectral bandwidth of the original pulse, and in order to get the shortest possible pulses, should be as broad as possible. It will of course not be broader than the original spectrum. In principle, it is possible to trade bandwidth for loss here. I wrote an algorithm to optimise the desired reflected spectrum: the spectral bandwidth is made as broad as possible, subjected to minimising the energy lost in the reflection. The advantage of this method should be that the reflected pulse is transform limited.

Figure 3.15 shows the reflection spectrum of the designed grating (thick full line), the spectrum of the pulse (full line) and the reflected pulse spectrum (dashed line) which is perfectly Gaussian. The reflected Gaussian pulse, designed to retain as much as possible of the original pulse spectrum is cleaned from its adjacent longitudinal side modes. The FWHM duration of the pulse is now determined by the spectral width, as this pulse will automatically be transform-limited (fully chirp compensated). This input is imported into a commercial FBG design package (*AttolightReconstructor*). This package implements a full time domain layer peeling algorithm [16]. The spectral response calculated from the designed grating is then subsequently used for further simulations, in particular to assess the effectiveness of the design shown in the results below.

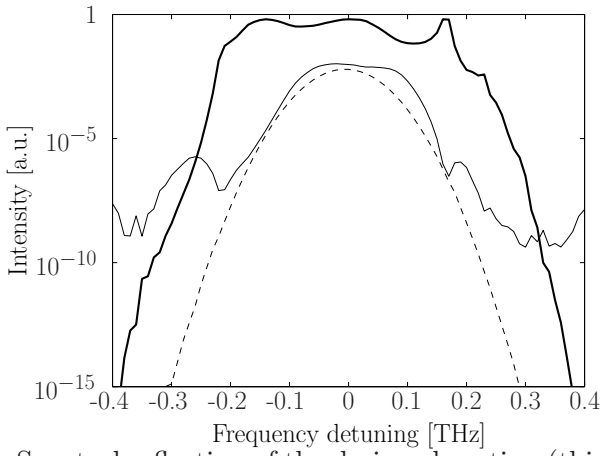

FIGURE 3.15: Spectral reflection of the designed grating (thick solid line), pulse spectrum (solid line) and the calculated reflected (Gaussian) pulse spectrum (dashed line).

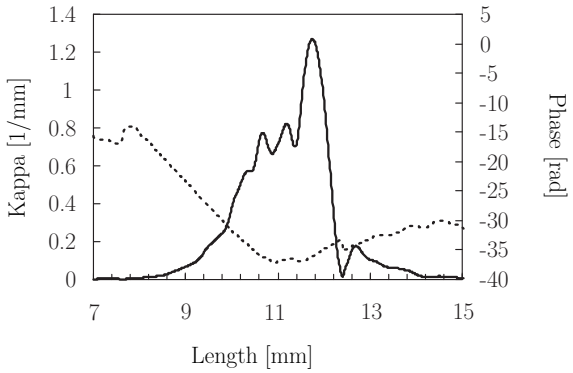

FIGURE 3.16: The grating design parameters Kappa (full line) and phase (dotted line) versus distance.

Figure 3.17 summarises four different possibilities to linearly compress and optimise the measured gain switched pulses: either through propagation over dispersive fibre, a linearly chirped grating, a linearly chirped grating including spectral filtering, or a matched grating, as designed above, including both nonlinear chirp compensation and optimal spectral filtering. Starting from a measured pulse with a time bandwidth product (TBP) of 1.35, a pulse with a TBP of 0.69 is formed through propagation over 90 m of DCF. A better fit of the chirp characteristics means that a pulse with a slightly better temporal extinction ratio is created by reflection off a linearly chirped FBG (ER=20 dB). When spectral filtering is introduced together with the linear chirp compensation in the grating, the extinction ratio further improves to 30 dB, but an even cleaner pulse can be created by compensating for both linear and nonlinear chirp, and incorporating spectral filtering. With this, we can theoretically reach a temporal extinction ratio of more than 50 dB, and a time bandwidth product of 0.45, very close to the 0.44 limit for

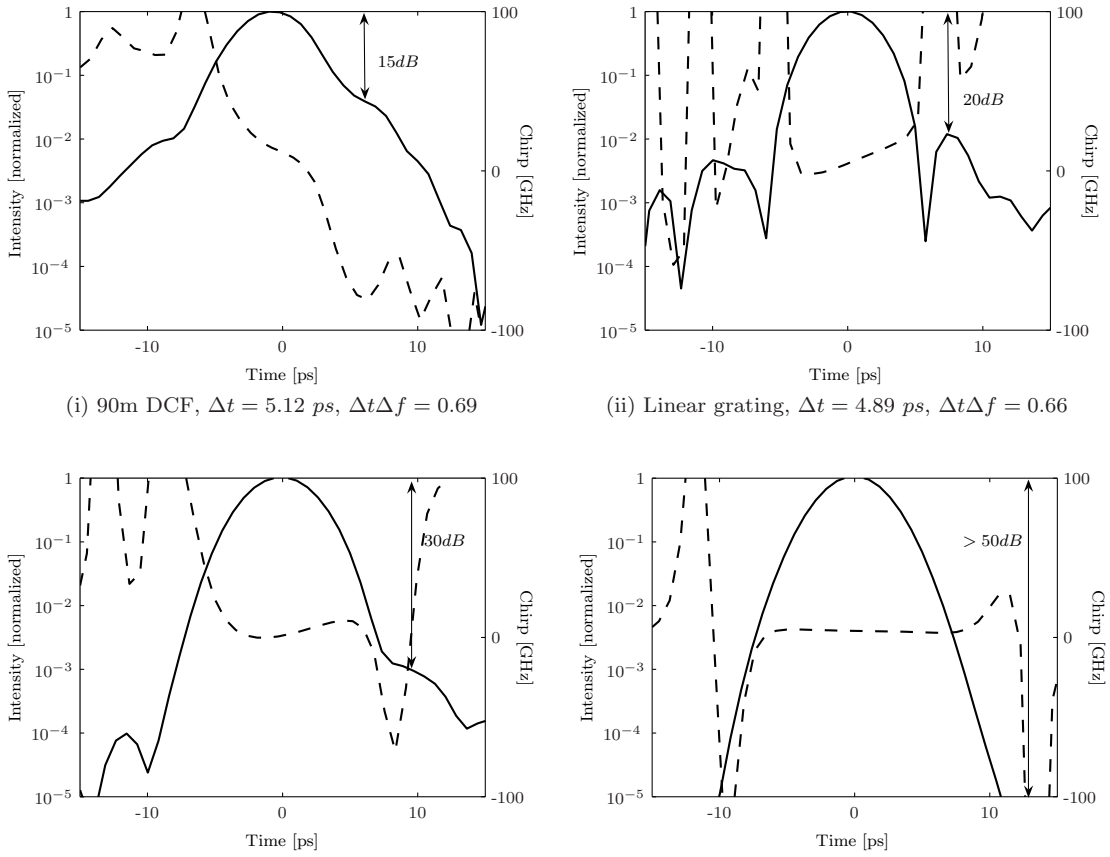

(i) 90m DCF, $\Delta t = 5.12\ ps$, $\Delta t \Delta f = 0.69$

(ii) Linear grating, $\Delta t = 4.89\ ps$, $\Delta t \Delta f = 0.66$

(iii) Linear grating and spectral filtering, $\Delta t = 5.37\ ps$, $\Delta t \Delta f = 0.47$

(iv) Matched FBG, $\Delta t = 5.11\ ps$, $\Delta t \Delta f = 0.45$

FIGURE 3.17: Overview of the results of various compression and pulse cleaning methods, showing the temporal intensity (full line) profile and the chirp (dashed line) of the pulses.

Gaussian pulses.

We note that the pulses become slightly longer when spectral filtering is introduced (0.4 *ps* longer), due to the decreased spectral bandwidth. The better temporal extinction ratio however makes this pulse more suitable than the slightly shorter pulse with worse extinction ratio, for high repetition rate systems (80 *Gbit/s*), where neighbouring pulses would otherwise overlap and interfere with these side-pulses.

Unfortunately, the fibre Bragg gratings I designed here were not delivered within the time scale of this project. However, the gain switched lasers are frequently used now in various experiments, especially the linearly compressed pulse, using DCF, because of its compactness and practical applicability. It has enough bandwidth to accurately produce complicated OCDMA waveforms (see further on in this thesis), and has also been used for different regeneration experiments, such as

those performed by Francesca Parmigiani in work reported in references [17, 18], as a sort of optical clock for example.

3.2.2.4 Nonlinear compression

With a FWHM duration of about 5 ps, the pulses may just be short enough to be used in an 80 $Gbit/s$ system, but they are definitely too long for a 160 $Gbit/s$ system, where the bit period is only 6.25 ps. The preferred mark to space ratio in optical RZ transmission systems is around 20 %, as one has to mitigate the effects of timing jitter, dispersive broadening and nonlinear effects.

To shorten the pulses even further, nonlinear techniques have to be used. Self phase modulation will broaden the pulses spectrally, after high power amplification and propagation in a nonlinear medium (for example a dispersion shifted fibre). Simultaneously the pulses develop a large up-chirp. This chirp can be compensated by propagation in standard single mode fibre as previously discussed.
We have also briefly looked at other techniques, such as nonlinear optical loop mirrors, to temporally compress the pulses. However, to engineer pulses with picosecond and shorter durations, the compression schemes become so involved that the original compactness of the gain switched laser looses much of its attractiveness due to the considerable postprocessing required to get down to these ultrashort pulse lengths. Considerable lengths of fibres have to be used, making the short pulse setup more prone to environmental changes. However, using such approaches, I succeeded to generate pulses as short as 500 fs, albeit of limited quality. The complete pulse characterisation techniques mentioned in this thesis are very helpful in the design of these advanced compression techniques, and can significantly reduce the amount of experimental work required to fully optimise the compression schemes.

3.2.3 Power scaling

The gain switched pulses described above, compressed using the 125 m of dispersion compensating fibre, have also been used in a high power amplification experiment. There is increasing interest in compact high power pulse sources for use in terrestrial and spaced based free space communications [19], LIDAR [20]

and micro-machining [21]. The gain switched laser was used as the master oscillator in the high power amplification scheme (MOPA), shown in Figure 3.18.

The pulses (3 dBm average power) are data modulated before they are pre-

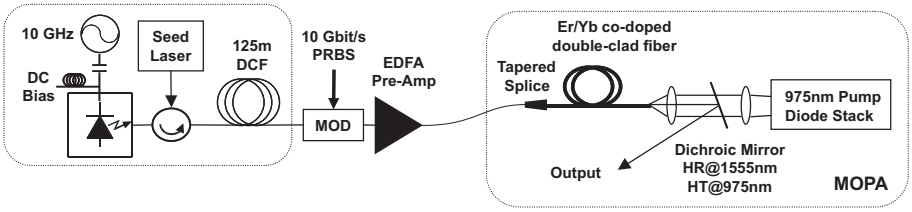

FIGURE 3.18: Experimental setup to amplify 4.5 ps pulses to an average power of 60 W (experiments in collaboration with the High Power Fibre Laser group).

amplified up to 33 dBm, so that we can assess the quality of amplification (i.e. low ASE levels) through a visual inspection of the eye diagram. A tapered splice optimises the mode matching between the standard single mode fibre and the core of the high gain fibre. This gain fibre is pumped by a diode stack at 975 nm that is free space coupled into the double clad final stage amplifier, in a counter propagating configuration. My contributions involved the integration of the gain switched laser setup into the MOPA system, and the characterisation of the pulses after amplification.

The pulses were amplified to a record average power level at 1550 nm of 60 Watt, using a specially fabricated Erbium/Ytterbium (Er/Yb) co-doped fibre. Figure 3.19 shows some of the results. The spectral trace shows no broadening after the high power amplification (fig. 3.19ii), confirming that nonlinear effects are minimised in the large core amplifier fibre. Also the eye diagrams indicate that there is no significant penalty added by the amplification (fig. 3.19iii). The pulse duration of 4.5 ps is maintained after amplification to 60 W, as can be seen on the autocorrelation traces (fig. 3.19iv).

We have also used the data modulator to produce a pattern of 1 'on' bit out of 1000, to gate the repetition rate down to 10 MHz, whilst maintaining the 60 W average signal power. This leads to roughly 1.3 MW peak powers. The results of these experiments were published and presented at the Conference on Lasers and Electro-Optics in San Francisco, 2004 [22]. More details about the experiment and the results can be found in this paper.

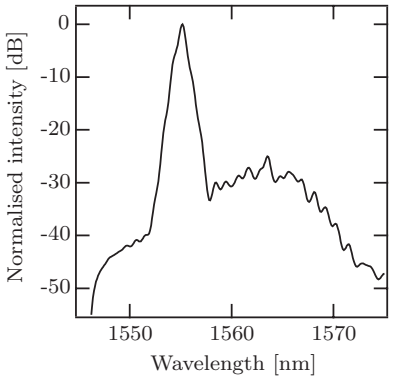

(i) Spectrum

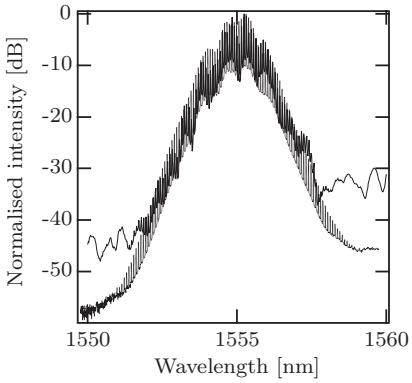

(ii) Spectrum detail, before (dotted) and after amplification (full line)

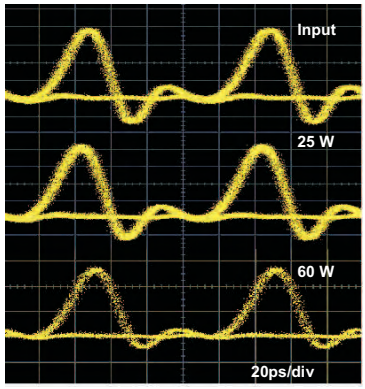

(iii) Oscilloscope traces

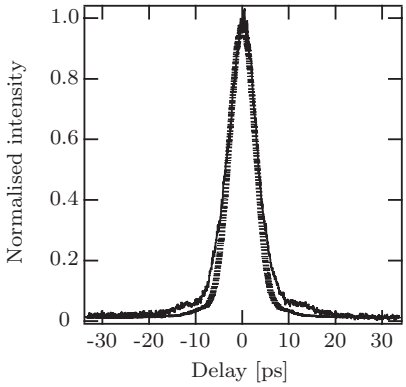

(iv) Autocorrelation traces, before (dashed) and after amplification (full line)

FIGURE 3.19: Spectrum, oscilloscope and autocorrelation traces for the high power amplification of the 4.5 *ps* gain switched laser pulses.

3.2.4 1060 *nm* gain switched laser and its characterisation

The linear spectrogram technique demonstrated in this thesis is certainly not limited to the region around $1.5\mu m$ and neither are short pulse sources. It does become more challenging to find a gating modulator that is compatible with short pulse durations at wavelengths outside of the $1.5\mu m$ region. Nevertheless, we have been able to adapt the scheme to suit gain switched DFB laser pulses, with a repetition rate of 1 *GHz*, in the $1\mu m$ region.
With increasing interest in this wavelength region for power scaling with Yb^{3+}-doped fibre technology, this pulse characterisation method is certainly attractive.

The experimental setup is shown in Figure 3.20. The gating function here is implemented with an electro-optic Mach-Zehnder modulator with a bandwidth of 5 *GHz*. The modulator is driven by a short pulse generator with a 3 *GHz* bandwidth electrical pulse capable of *variable delays* (as needed for a spectrographic

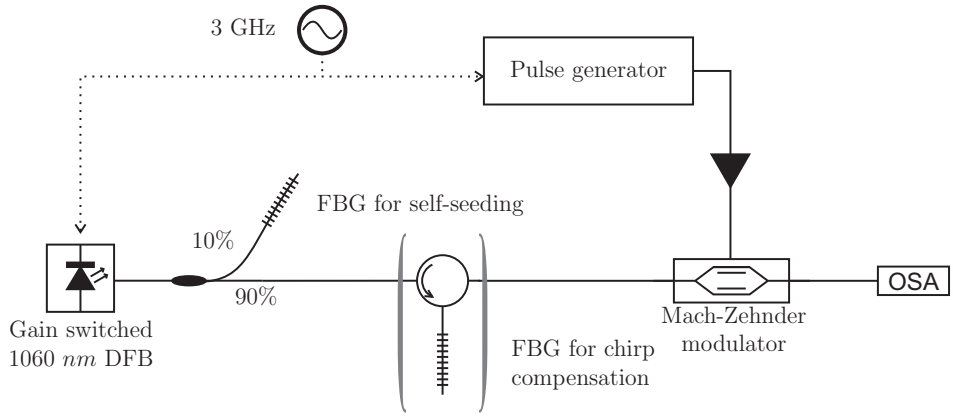

FIGURE 3.20: Experimental setup for generation and characterisation of gain switched pulses at 1060 *nm*.

technique) and variable duty cycles.

The optical spectrum analyser resolution of 1.25 *GHz* means that the 1 *GHz* spectrograms are slightly undersampled spectrally. However, the intrinsic redundancy of information in the spectrogram means that a good retrieval is still possible.

We investigated two ways of seeding these gain switched pulses (cf. Section 3.2), in order to select a longitudinal mode and reduce the timing jitter: either by injecting a 1060 *nm* CW signal, or by self-seeding the diode using an external fibre Bragg grating (as shown in Figure 3.20). The results of the characterisations are shown in Figures 3.21 and 3.22 respectively. In both cases, the pulses were measured with and without linear compression with a chirped fibre Bragg grating.

The main difference between the two different ways of seeding the pulse generation is a clear spectral intensity ripple in the case of self-seeding. Similarly to the 1550 *nm* gain switched lasers, the pulses are ideally seeded at the higher initial frequencies. When the whole spectrum of the pulse is reflected, as is the case for the self-seeding here, the ideal down-chirp pulse development is disturbed.

As can be seen in the figures, there is excellent agreement between the measured and reconstructed spectrograms (0.002 rms error on a 128×128 point grid). The agreement of the independently measured spectrum and the spectrum retrieved from these spectrograms is excellent over a range of 3 orders of magnitude. This is limited by the noise level, and adjacent modes which were both thresholded from the data.

The gain switched pulses are again heavily chirped, and have a duration of about 75 *ps*. This is still easily measured with a fast photo-diode and electrical sampling oscilloscope (20 *GHz* bandwidth). The pulses were subsequently compressed using

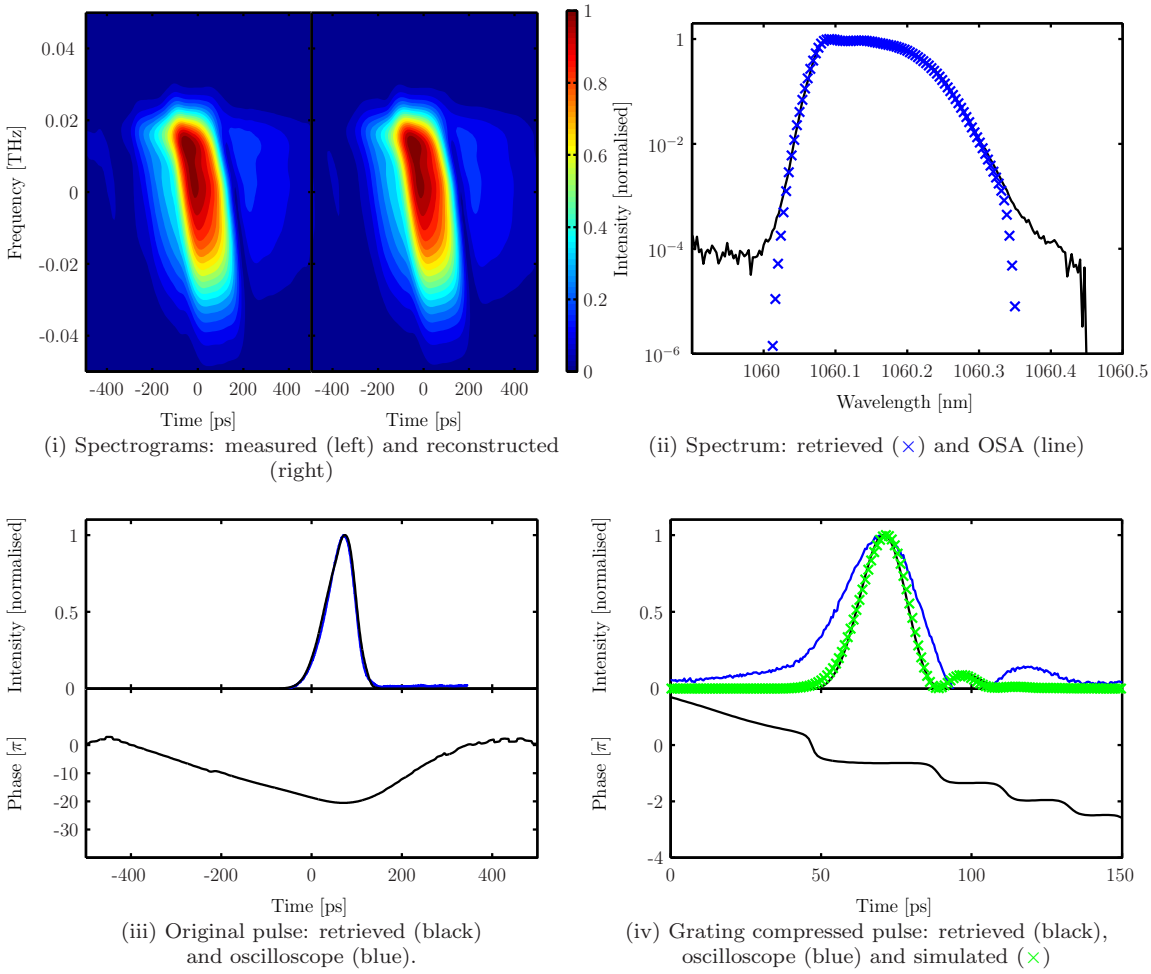

(i) Spectrograms: measured (left) and reconstructed (right)

(ii) Spectrum: retrieved (×) and OSA (line)

(iii) Original pulse: retrieved (black) and oscilloscope (blue).

(iv) Grating compressed pulse: retrieved (black), oscilloscope (blue) and simulated (×)

FIGURE 3.21: Pulse information for the 1060 *nm* gain switched laser, seeded with an external CW laser.

a linearly chirped fibre Bragg grating, and measured again. The pulses are now too short (18 *ps*) to be accurately measured with the electrical sampling oscilloscope: the blue trace in subfigures (iv) shows a clear ringing effect, and the shape of the pulse is severely distorted.

These figures, on the other hand, show the excellent agreement between the intensity profile retrieved from the spectrogram, and the intensity calculated by mathematically propagating (NLSE) the uncompressed pulses.

NLSE propagation simulations show that the minimum pulse duration obtainable by removing the linear chirp is 16 *ps*, slightly less than that achieved to date using the fibre Bragg grating, due to a slight mismatch of the chirped grating with respect to the chirp of the generated pulse.

The retrieved gating function is shown in Figure 3.23. The FWHM duration is 139 *ps* and 190 *ps* long for an electrical driving pulse with nominal durations of

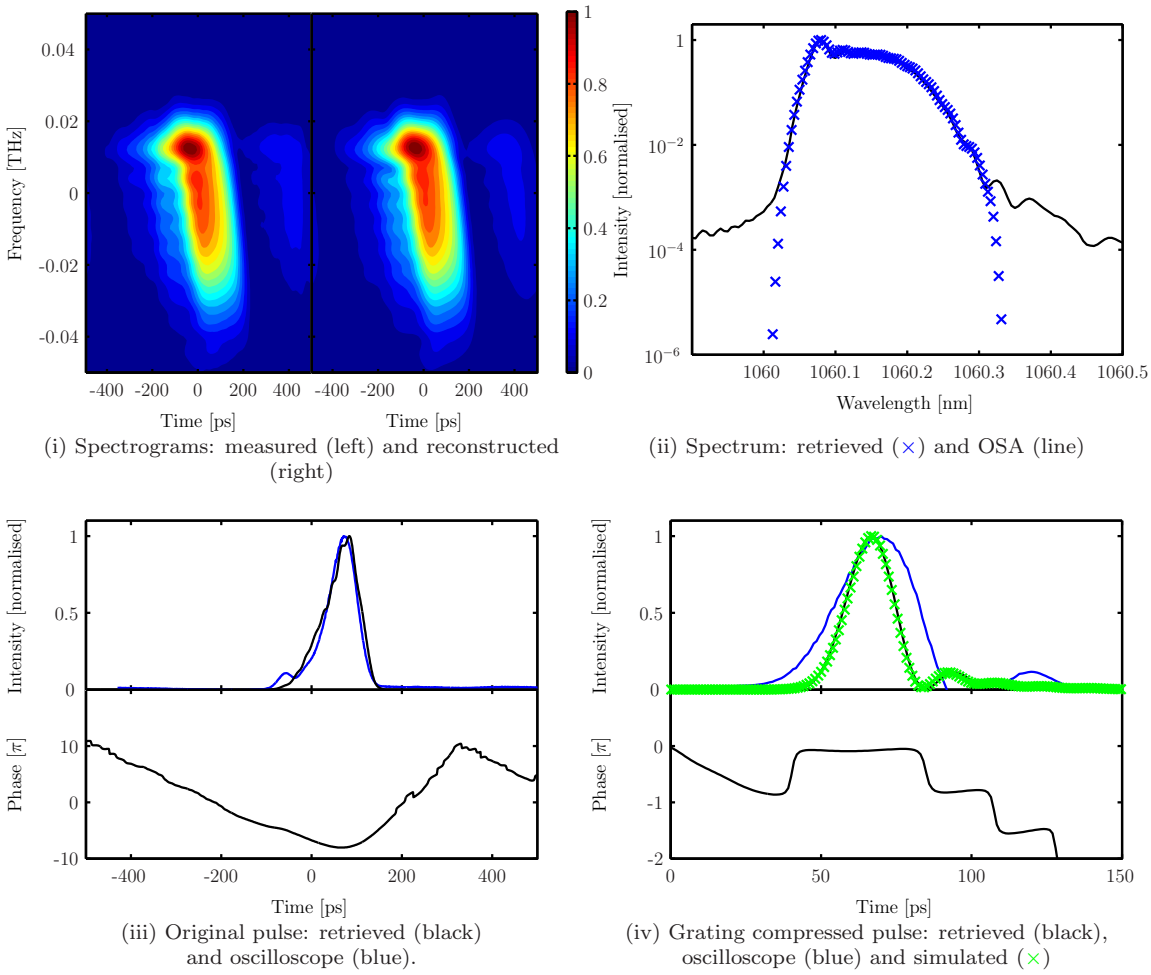

(i) Spectrograms: measured (left) and reconstructed (right)

(ii) Spectrum: retrieved (×) and OSA (line)

(iii) Original pulse: retrieved (black) and oscilloscope (blue).

(iv) Grating compressed pulse: retrieved (black), oscilloscope (blue) and simulated (×)

FIGURE 3.22: Pulse information for the 1060 *nm* gain switched laser, self-seeded through the reflection of a fibre Bragg grating.

100 *ps* and 200 *ps* respectively. Note the $1 - \exp(-c.t)$ profile of the leading edge of this gate, which can be explained by considering the capacitive effect of the electrical drive circuitry of the modulator, which is not optimised for high speed operation. The abrupt phase shift of about π is due to the fact that modulator is biased slightly negatively in the rest state (fig. 3.23, bottom).

This example, and the excellent agreement with independent measurements, shows again that the linear spectrogram method is not grossly limited by the duration of the gating function.

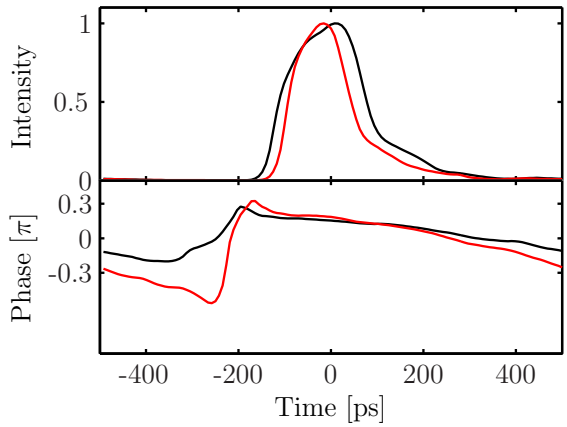

FIGURE 3.23: The gating function of the $LiNbO_3$ Mach Zehnder modulator, driven with a 100 *ps* (red) or 200 *ps* (black) electrical pulse.

3.3 EAM carved pulses

The electro-absorption modulator (EAM) is introduced briefly in Section 2.4, as the sampling element of the pulse characterisation method. Due to the fast switching speeds that can be reached with these modulators, they are quickly infiltrating various different fields of high speed optical pulse generation, modulation and processing.

In insulators and semiconductors, the optical absorption edge shifts to lower energies under the influence of an electric field. Specially engineered semiconductor materials and optical waveguides now make it possible to create very effective optical modulators based on this quantum-confined Stark effect [23]. By applying a reverse bias to the electro-absorption device, the electric field induces a shift of its optical absorption edge to lower energies (higher wavelengths). Photons with energies slightly lower than the bandgap energy of the semiconductor material will now be absorbed, creating electron-hole pairs that are swept away in the presence of an electrical field, whereas the material is transparent for these photons when there is no electrical field applied. With efficient coupling of the RF electrical field (travelling-wave EAMs), switching speeds good for > 80 $Gbit/s$ transmission systems have been demonstrated [24].

As in semiconductor lasers, there is phase modulation accompanying the intensity (absorption) modulation. However, the origin is not due to changes in carrier densities in this case; rather the change in absorption spectrum induces changes

in refractive index n through the Kramers-Kronig relation:

$$\Delta n(\omega) = \frac{c}{\pi} \int_0^\infty \frac{\Delta\alpha(\omega')}{\omega'^2 - \omega^2} d\omega' \tag{3.5}$$

$\Delta n(\omega)$ denotes the voltage induced changes. The chirp parameter in recent EAMs has been greatly decreased through careful engineering of the waveguide, but remains significant. The measurements below and further on in this work will show distinct chirp profiles in both the sampling function of the linear FROG spectrogram technique, as well as on pulses generated with EAMs.

Due to the fast absorption changes possible, the EAM can follow the applied electrical signal on to the optical CW signal travelling through the waveguide at very high speeds. With state-of-the-art EAM bandwidths currently reaching speeds up to 80 *GHz* and beyond, the challenge now becomes more and more one of finding a suitable electrical drive signal and a compatible package in order to fully utilise the available bandwidth.

Research in optimising various properties of EAMs that are important for high speed telecommunication systems is mainly focussed on reducing the polarisation dependence and insertion (fibre coupling) loss through waveguide engineering, reducing the optical wavelength dependence and chirp generation, the optical power handling and further increasing the electrical modulation bandwidth.

3.3.1 EAM coupling

For most of the examples in my thesis I used commercial, appropriately packaged EAMs. However, in order to gain access to state-of-the-art lab samples, we entered a collaboration with Alcatel-Thales. Since our collaborators could only provide submounted chip samples, I had to set up an EAM coupling station, including optical input and output coupling and electrical RF coupling. A photo of the setup I built to test and use the submounted EAMs provided by Alcatel-Thales is shown in Figure 3.24. A detail of the fibre optic coupling and the waveguide is shown in Figure 3.25. The fibres used to efficiently couple light in and out of the waveguide are lensed and tapered, because the EAM waveguide dimensions are of the order of micrometers. To match the mode diameter of the optical signal to this very fine waveguide, the lens at the end of the fibre focusses the optical wave down to 3 μm. The free space distance from the fibre tip after which this 3 μm

beam waist is reached is 7 μm. Even an on screen magnification using cameras by a factor of 200 does not give enough resolution to be able to accurately position the tapered-lensed fibres for optimal coupling into the waveguide. As for all III-IV semiconductor waveguide components (laser diodes, photodetectors, etc.) the faces are very fragile quasi-perfect mirrors made of nearly single atomic scale flatness as formed by cleaving. It is as good as impossible to *touch* the faces of an EAM without causing irreversible damage.

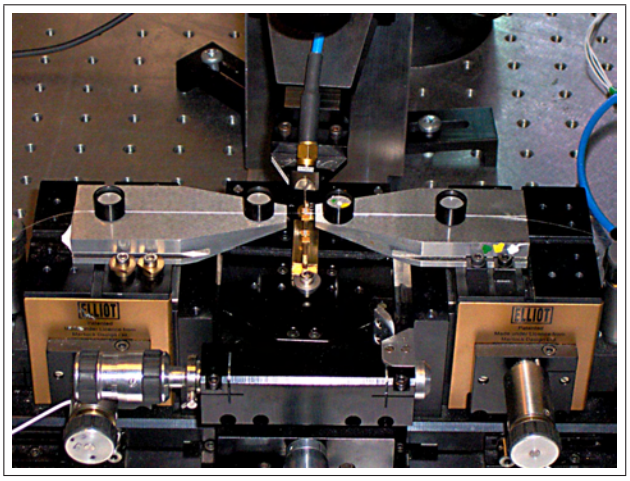

FIGURE 3.24: Photo of the test setup for the submounted EAMs provided by Alcatel.

FIGURE 3.25: Close up photo of the lensed fibres coupling light in and out of the EAM waveguide.

The physics of the focussed laser beam and the EAM waveguide are helpful though to ensure optimal coupling: after the laser beam has reached its minimal beam waist, it expands again. The optimal coupling distance can thus be found by progressively moving the fibre tip closer to the waveguide, whilst watching the

electrical current generated by the device due to photon absorption. As the coupling efficiency increases as the fibre tips are moved closer, the generated current increases. At a certain point, the generated current reaches its maximum, and moving the fibre tip still closer to the waveguide edge makes the current drop again. At this point, the fibre tip is already too close to the waveguide. The warning given by the decreasing current makes the optical coupling optimisation a fairly straightforward procedure, greatly reducing the danger of destroying the EAM by touching the cleaved edge.

The total insertion loss I reached with the provided EAMs and the tapered-lensed fibre coupling setup was less than 9 dB (0 V bias). This figure is similar to those of commercial, packaged EAMs (of the order of 8 dB).

As well as the optical coupling, I also had to take care of the electrical coupling of the submounted EAM. The submount provided three patches in a ground-signal-ground configuration, compatible with the standard 150 μm pitch. The electrical probe I used to probe these patches is a Picoprobe 40A-GSG-150-P, which is a broadband probe, with a bandwidth of 40 GHz. A current meter was then included in the DC path (providing the bias on the EAM with a bias-T), to monitor the photo-current.

3.3.2 Measurements

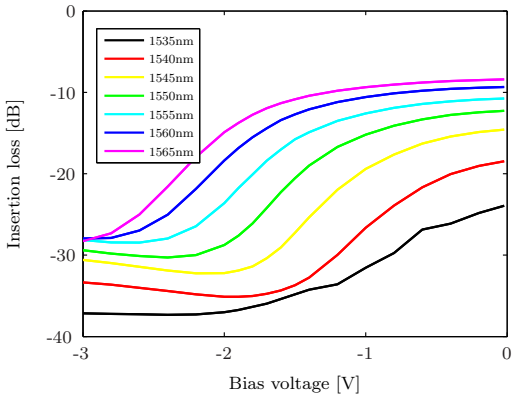

FIGURE 3.26: DC transfer curve of EAM A3 at various wavelengths.

Figures 3.26 and 3.27 show the transfer characteristics for the two EAMs provided by Alcatel-Thales, named A3 (50μm long waveguide) and D3 (100μm long waveguide), for several wavelengths. Choosing the correct bias point and modulation

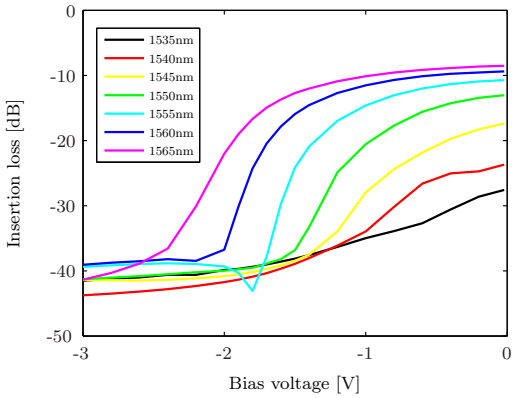

FIGURE 3.27: DC transfer curve of EAM D3 at various wavelengths.

depth allows one to optimise the extinction ratio of the modulation. With higher bias voltages applied, the modulation window is shortened, although the extinction ratio will be reduced, due to the increased absorption and total insertion loss. These DC transfer curves give a reasonable idea of the modulation properties of the EAM at high speed radio frequencies (RF), however they do not contain any phase information. A direct measurement with the EAM-FROG technique provides more insight into the exact phase modulation induced by the RF modulation, as it characterises the sampling function of the measurement setup as well as the phase characteristics of the pulses under test.
The transfer curves highlight the fact that the two EAMs were designed with a different purpose in mind. According to C. Kazmierski, who fabricated them, there is a trade-off between wavelength uniformity and steepness of the transfer curve. Either one can choose to make EAMs with very steep transfer curves, but that will make the transfer characteristics very wavelength dependent, or one can choose to make the transfer function nearly wavelength independent (apart from the higher insertion loss towards lower wavelengths), but then the transfer characteristic is no longer as steep. The steeper the transfer curve, the shorter the pulses one can carve with the modulator. A steeper transfer curve may be more desirable in single channel high repetition rate systems, while wavelength independent EAMs will find their application in wavelength division multiplexing (WDM) systems.

A typical spectrogram for a simple EA modulated CW laser beam is shown in Figure 3.28. In this case, the commercial EAM (OKI OM5642W-30B, n.418-3) was used for the pulse source, and the submounted Alcatel-Thales EAM A3 was used as the sampling EAM in a self-referenced setup (see Figure 2.6). Due to the very good stability of this pulse source, these pulses lead to very good measurements

and subsequent retrievals in the case that the linear FROG spectrogram method is used. With a retrieval error < 0.002 on a 32x32 point grid and very good spectral agreement between the retrieved and independently measured signals, the information gained from these measurements is very reliable and interesting. To avoid ambiguities in the phase retrieval though, it is better to choose the bias voltage of the sampling EAM in such a way that the pulse and the sampling window have a different duration.

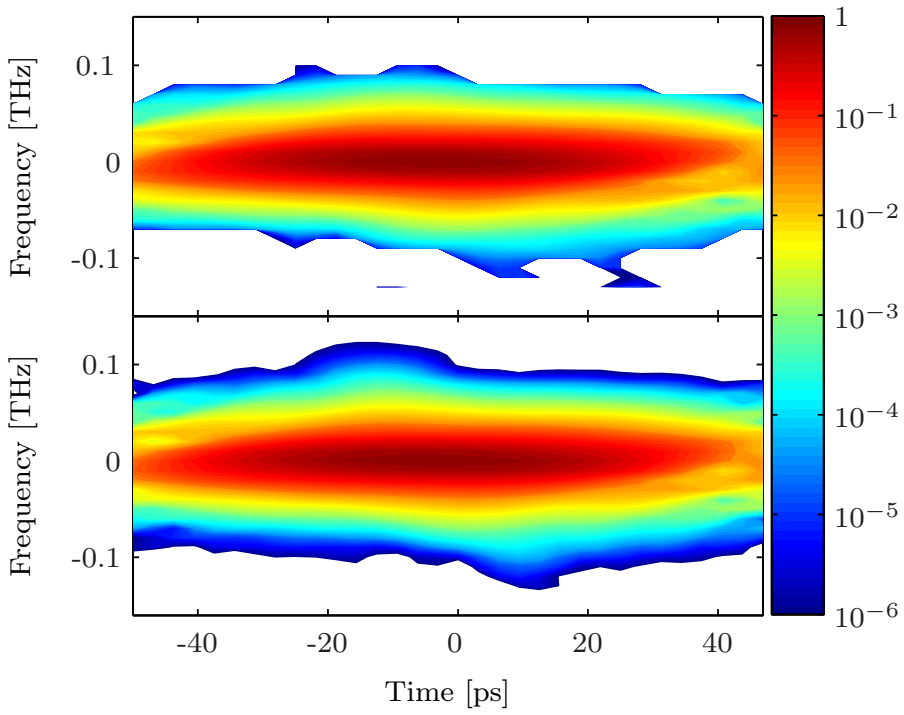

FIGURE 3.28: EAM-FROG spectrogram of EAM carved pulses, measured (top) and retrieved(bottom).

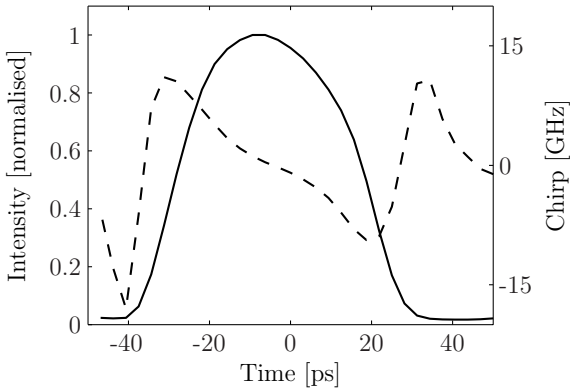

FIGURE 3.29: Retrieved pulse information (OKI EAM bias voltage $-2V$, driven with $2.5V_{pp}$ sinusoid).

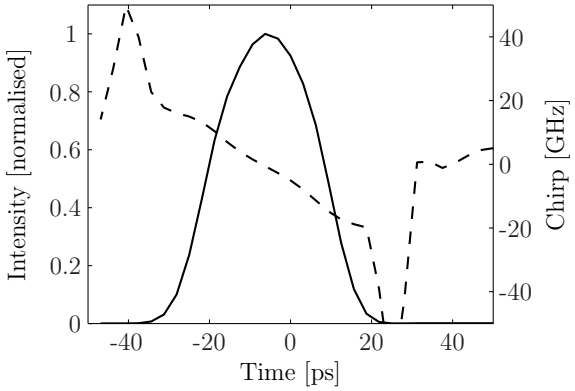

FIGURE 3.30: Retrieved gate information (Alcatel-Thales EAM D3, bias voltage $-1.5\ V$, driven with a 1.2 V_{pp} short pulse, converted from the optical pulse shown in Figure 3.29).

The pulses created in this way are chirped (again downchirp), which means that again, they can be compressed by propagating them over DCF, in the same way as described in Section 3.2.2. It turns out that the ideal length of fibre for the usual driving range of the EAMs is also around 150 m, close enough to the 125 m cut to match the gain switched laser pulses. The minimum pulse length reachable after compression with DCF is about 6 ps, depending on the EAM used and the exact driving parameters. Due to its ease of use, stability and clean spectral and temporal properties, this source is frequently used in the lab, as a pulse source for transmission experiments or as an input for various pulse shaping experiments. The main drawback of this pulse source is that the optical input power is limited to 5 dBm (or 13 dBm for the newer units), which means that the output power is limited to under 0 dBm for normal RF driving conditions. Amplifiers are always needed, introducing ASE at the start of practically any experiment using this pulse source. More extensive experiments with EAM carved pulses are presented in chapter 5.

Compared to the commercial EAM packages we have in our lab, the two different EAM-chips provided by Alcatel-Thales were up to very high standards, even though it was my first attempt in coupling them both electrically and optically. Certainly for pulse carving, EAM D3 performed very well, as it required a very low driving voltage and bias, to generate pulses slightly shorter than the commercial EAMs, at least for wavelengths around 1550 nm. If a broader operating wavelength region is desired, then EAM A3 performs better than the commercial EAMs, for wavelengths down to 1535 nm. This EAM is preferable when working at the lower C-band wavelengths, particularly for use in a linear spectrogram scheme, where the gate function duration is not critical.

3.4 Conclusions

The gain switched and the EAM-carved laser pulses, as presented in this chapter, are particularly stable and convenient pulse sources. Even though they generate pulses with a significant chirp profile, they are now frequently used in various experiments, most often in conjunction with a linear compression stage formed by a length of DCF. Knowing the exact pulse shape and phase is of great value, as has been demonstrated with the design of a special fibre Bragg grating that could in principle compress the gain switched pulses to clean 5 ps Gaussian pulses.
Furthermore, thanks to the linear spectrogram technique, it has been possible to see how the pulse develops, and what the influence of the external seed power and wavelength is. In the case of the 1060 nm laser diode, we can see that self-seeding, where the whole pulse is reflected back, has detrimental effects on the pulse development. However, we should be able to avoid this effect by using a narrow band reflecting grating for reflecting only the lower wavelengths of the pulse. This would then mimic the behaviour of a narrow external laser as a seed.
The fact that we have been able to adapt the technique successfully to measurements of short pulses at 1 μm, with another kind of optical modulator, also shows some of the versatility of spectrographic characterisation methods.

Pulse carving with an electro-absorption modulator is not only relevant for its use as a short pulse source, but also for the gating function we frequently use for the construction of the linear spectrograms. The measurements presented here also provide valuable information for future generations of EAMs. The exact specifications for the modulators will vary with the envisaged application, e.g. as a pulse generator or gating function in a demultiplexing setup (which both require short temporal windows), or as a gating function in a spectrogram setup. The effects of the wavelength dependency of the EAMs in spectrograms will be shown in Chapters 4 and 5, where some spectrally broad signals are investigated.

References

[1] W. Lee, V. Filsinger, L. Klapproth, H.-G. Bach, and A. Beling, "Implementation of an 80 Gbit/s full ETDM multi-format ASK optical transmitter," 31st European Conference on Optical Communication **3**, 383 – 4 (2005).

[2] G. Bosco, A. Carena, V. Curri, R. Gaudino, and P. Poggiolini, "On the use of NRZ, RZ, and CSRZ modulation at 40 Gb/s with narrow DWDM channel spacing," Journal of Lightwave Technology **20**, 1694 – 704 (2002).

[3] P. Winzer and A. Kalmar, "Sensitivity enhancement of optical receivers by impulsive coding," Journal of Lightwave Technology **17**, 171 – 7 (1999).

[4] H. Sunnerud, M. Karlsson, and P. Andrekson, "A comparison between NRZ and RZ data formats with respect to PMD-induced system degradation," IEEE Photonics Technology Letters **13**, 448 – 50 (2001).

[5] S. Bigo, G. Charlet, and E. Corbel, "What has hybrid phase/intensity encoding brought to 40 Gbit/s ultralong-haul systems?" 30th European Conference on Optical Communication ECOC 2004 **4**, 872 – 5 (2004).

[6] P. Winzer and C. Chandrasekhar, "SC4 - Modulation Formats and Receiver Concepts for Optical Transmission Systems," 31st European Conference on Optical Communication. ECOC 2005 **Short course notes** (2005).

[7] H. Ito, H. Yokoyama, S. Murata, and H. Inaba, "Picosecond optical pulse generation from an r.f. modulated AlGaAs d.h. diode laser," Electronics Letters **15**, 738 – 40 (1979).

[8] H. Ito, H. Yokoyama, S. Murata, and H. Inaba, "Generation of picosecond optical pulses with highly RF modulated AlGaAs DH laser," IEEE Journal of Quantum Electronics **17**, 663 – 70 (1981).

[9] D.-S. Seo, H.-F. Liu, D. Kim, and D. Sampson, "Injection power and wavelength dependence of an external-seeded gain-switched Fabry-Perot laser," Applied Physics Letters **67**, 1503 – 5 (1995).

[10] D. Huhse, M. Schell, J. Kaessner, D. Bimberg, I. Tarasov, A. Gorbachov, and D. Garbuzov, "Generation of electrically wavelength tunable (Δλ = 40 nm) singlemode laser pulses from a 1.3 μm Fabry-Perot laser by self-seeding in a fibre-optic configuration," Electronics Letters **30**, 157 – 158 (1994).

[11] L. Barry, B. Thomsen, J. Dudley, and J. Harvey, "Optimised design of fibre-based pulse compressor for gain-switched DFB laser pulses at 1.5 μm," Electronics Letters **35**, 1166 – 8 (1999).

[12] K. Ahmed, B. Eggleton, H.-F. Liu, P. Krug, and F. Ouellette, "Simultaneous mode selection and pulse compression of gain-switched pulses from a Fabry-Perot laser using a 40-mm chirped optical fiber grating," IEEE Photonics Technology Letters **7**, 158 – 60 (1995).

[13] X. Zhang, Z. Yu, N. Lin, and X. Liu, "Chirp elimination using a linearly chirped fiber grating," Optical and Quantum Electronics **33**, 1173 – 80 (2001).

[14] S. Li, K. Chan, Y. Liu, L. Zhang, and I. Bennion, "Simultaneous chirp compensation and single-mode operation of a self-seeded gain-switched semiconductor laser with a linearly chirped fiber Bragg grating," Technical Digest. CLEO/Pacific Rim '99. Pacific Rim Conference on Lasers and Electro-Optics **3**, 922 – 3 (1999).

[15] G. Agrawal, *Nonlinear Fiber Optics* (Academic Press, 2001).

[16] R. Feced, M. Zervas, and M. Muriel, "An efficient inverse scattering algorithm for the design of nonuniform fiber Bragg gratings," IEEE Journal of Quantum Electronics **35**, 1105 – 15 (1999).

[17] F. Parmigiani, P. Petropoulos, M. Ibsen, B. Thomsen, and D. Richardson, "Retiming of short optical pulses using linear pulse reshaping and all-optical switching," Optical Fiber Communication Conference (OFC) (IEEE Cat. No.04CH37532) **2** (2004).

[18] F. Parmigiani, P. Petropoulos, P. Almeida, M. Ibsen, and D. Richardson, "Amplitude and timing jitter reduction using a fiber NOLM incorporating a fiber Bragg grating based pulse shaper," 2005 Optical Fiber Communications Conference Technical Digest **1** (2005).

[19] K. Hall, W. Atia, J. Moores, R. Bondurant, and K. Rauschenbach, "A 100 Gb/s, 9-Watt transmitter," Technical Digest. Summaries of papers presented at the Conference on Lasers and Electro-Optics. Postconference Edition. CLEO '99. Conference on Lasers and Electro-Optics pp. 17 – 1 (1999).

[20] W. Gong, D. Temple, A. Omar, J. Mangana, K. M. Maung, S. Bailey, D. Harper, R. Battle, A. Futrell, L. Haughton, D. Johnson, K. Lewis, C. Gile, J. Davis, L. Williams, T. Chyba, D. Richter, and N. Higdon, "A portable eye-safe scanning aerosol lidar of the Hampton University Center for Lidar and Atmospheric Sciences Students," Technical Digest. Summaries of papers

presented at the Conference on Lasers and Electro-Optics. Conference Edition **1**, 218 – 19 (2002).

[21] B. Chichkov, C. Momma, S. Nolte, F. von Alvensleben, and A. Tuennermann, "Femtosecond, picosecond and nanosecond laser ablation of solids," Applied Physics A: Materials Science & Processing **63**, 109 – 115 (1996).

[22] B. Thomsen, Y. Jeong, C. Codemard, M. Roelens, P. Dupriez, J. Sahu, J. Nilsson, and D. Richardson, "60 W, 10 GHz 4.5 ps pulse source at 1.5 μm," Conference on Lasers and Electro-Optics (CLEO) **1** (2004).

[23] D. Miller, D. Chemla, T. Damen, A. Gossard, W. Wiegmann, T. Wood, and C. Burrus, "Band-edge electroabsorption in quantum well structures: the quantum-confined Stark effect," Physical Review Letters **53**, 2173 – 6 (1984).

[24] R. Lewen, S. Irmscher, U. Westergren, L. Thylen, and U. Eriksson, "Ultra high-speed segmented traveling-wave electroabsorption modulators," Optical Fiber Communications Conference (OFC). Postdeadline Papers **3**, 38 – 1 (2003).

Chapter 4

Advanced pulse shapes and their characterisation

4.1 Pulse shaping with fibre Bragg gratings

Fibre Bragg gratings (FBG) have been used extensively for various applications in optical telecommunications. Both the amplitude and phase of pulses reflected in FBGs can be controlled very accurately with today's grating fabrication technology [1]. In Section 3.2.2.3, I have already proposed how gain switched pulses can be cleaned up through spectral filtering and compensation of the nonlinear chirp characteristics. More frequently implemented functions with FBGs are for example steep spectral filters for use in add-drop multiplexers, and tunable dispersion compensating units.

In this chapter, I will focus on a few very interesting pulse shaping functions implemented with fibre gratings. I first consider the generation of rectangular and parabolic pulses through the reflection of very short optical pulses from an appropriately designed fibre grating. Such pulses have interesting applications in the domain of all-optical regeneration, but require a very short pulse source, so that very fine pulse features can be generated.

For our experiments, we have used a harmonically and actively mode locked fibre ring laser to generate these pulses. The principle of operation will first be explained in Section 4.2, and an accurate characterisation of pulses from such a laser using the linear spectrogram technique is presented. After this, rectangular and parabolic pulses filtered from this short pulse source will be characterised, in

Sections 4.3 and 4.4 respectively, accompanied by a brief explanation of why these pulse shapes are so interesting.

Fibre Bragg gratings are also a strong candidate for optical code division multiple access systems. The fine structure that can be implemented with fibre Bragg gratings is ideal for generating the complex codes needed in these multi-user systems. In Section 4.5, I will show that linear spectrograms give very accurate, unique and useful information about these special phase encoding gratings.
With the results in this chapter, I am exploring some of the limits of the linear spectrogram method using an electro-absorption modulator. I am grateful for the curiosity of my colleagues, to find out what the exact shape and phase is of these interesting waveforms. Their help in setting up the experiments and making it possible for me to perform the characterisations has been invaluable: Francesca Parmigiani for the experiments involving rectangular and parabolic pulses; Chun Tian and Zhaowei Zhang for the OCDMA experiments; and Dr. Morten Ibsen for the fabrication of the numerous gratings.

4.2 Fibre ring laser pulses

4.2.1 Background

Fibre ring lasers can generate short pulses suitable for telecommunications repetition rates and wavelengths. Because of the long cavities possible in fibre lasers, a large number of longitudinal modes fall within the gain bandwidth of the gain medium in the cavity. The frequency spacing between the modes is given by $\Delta\nu = c/L_{opt}$, where L_{opt} is the cavity round trip length. When the phases of various longitudinal modes are synchronised such that the phase difference between any two neighbouring modes is constant (ϕ), mode locking occurs. For M coupled modes, the time dependent total intensity of the light is given by the following formula (E_0^2 is the amplitude of a mode, and is assumed equal for all modes) [2]:

$$|E(t)|^2 = \frac{\sin^2\left((2M+1)\,\pi\Delta\nu t + \phi/2\right)}{\sin^2\left(\pi\Delta\nu t + \phi/2\right)} E_0^2 \tag{4.1}$$

This is a periodic function with period $1/\Delta\nu$, the round trip time of the cavity, with a *sinc*-like shape. This can be interpreted as a single pulse circulating inside

the cavity, emitting a fraction of its energy every time it propagates through the output coupler.

The optical field inside the cavity can be modulated (either in phase or amplitude), to generate sidebands spaced apart by the modulation frequency. When the modulation frequency is equal to $\Delta\nu$ or an integer multiple thereof (harmonically mode locked), the sidebands overlap with other longitudinal modes, which leads to synchronisation between the phases of the modes, and thus active mode locking of the laser. A $LiNbO_3$ electro-optic modulator is commonly used as the active mode locking element in a fibre ring laser, because of its high speed operation and low insertion loss. When the modulation frequency of this modulator is an integer multiple of the mode spacing, the laser is *harmonically* mode locked. An integer number of pulses are now travelling around in the ring laser cavity at the same time. A basic scheme of a mode locked fibre ring laser is shown in Figure 4.1. The isolator ensures unidirectional operation and the erbium doped fibre represents the gain element in the cavity.

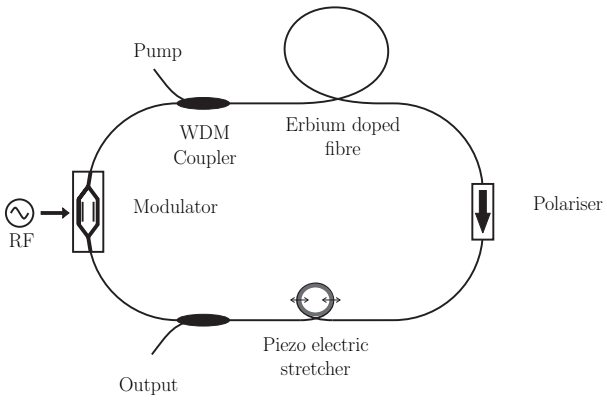

FIGURE 4.1: Schematic diagram of a mode locked fibre ring laser.

A drawback of harmonically mode locked fibre ring lasers is that due to the long cavity, they are very sensitive to environmental changes such as mechanical disturbances and temperature variation: the modulation frequency must remain matched to the longitudinal mode spacing $\Delta\nu$ or a multiple thereof. An electronic feedback loop can for example stabilise the cavity length through the use of a piezoelectric transducer for fine adjustment of the cavity length. However, even with these fine adjustments, the spectral modes of the pulses can still drift and jump around a little. It then becomes very difficult to apply any spectrally resolved technique for accurate phase characterisation of these pulses. These instabilities in fact make mode locked ring laser pulses some of the most difficult pulses to accurately phase characterise.

The pulses generated by the Pritel fibre ring laser in our lab are tunable between 1530 nm and 1560 nm, and have a pulse length of about 2.2 ps and a repetition rate of 10 GHz. Due to the broad bandwidth of these pulses, they are frequently used as inputs for various pulse shaping gratings. These pulses can also easily be interleaved to aggregate bit rates, as described in Appendix C. They have well defined properties (hyperbolic secant shape) and are virtually chirp and pedestal free.
What follows is a characterisation of these pulses, using linear spectrograms. Another fibre ring laser, with even shorter pulse durations, and operating at a 40 GHz repetition rate was used in experiments on the APRZ pulse format, as will be explained in Chapter 5.

4.2.2 Characterisation

A typical EAM-spectrogram of the Pritel pulses is shown in Figure 4.2. The temporal intensity and phase retrieved from this spectrogram are shown in Figure 4.3. Apart from the fact that the spectrogram grid needs to be larger in order to accommodate the pulse spectrally, whilst keeping the same temporal span (100 ps), the main difficulty is the spectral instability of the source. In many cases, there is severe spectral mode hopping during the acquisition of the spectrogram, making the spectrogram irregular. It becomes impossible to resample on the 10 GHz spectral lines. An envelope reconstructing algorithm was used together with mathematical filtering of the spectrogram before interpolating the data on a 128×128 point grid, according to the procedure explained in Section 2.5.2. To demonstrate the effect of this procedure, a detail of the spectrogram is shown before and after envelope detection in Figure 4.5. The spectral instability is indicated by the arrow, and becomes unnoticeable after the the envelope detection.
The accuracy of the retrieval is confirmed by the good agreement of the retrieved spectrum with the independently measured spectrum, as shown in Figure 4.4.

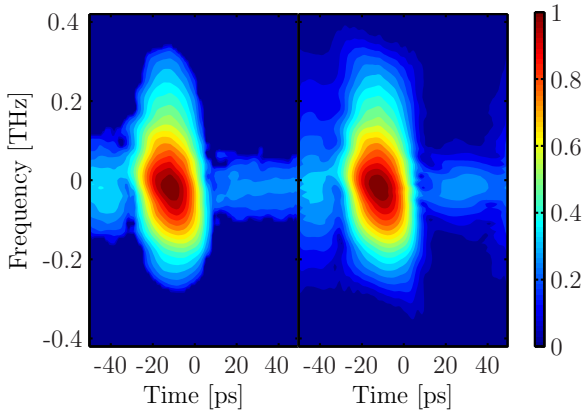

FIGURE 4.2: Measured (left) and retrieved (right) spectrograms for 2.5 *ps* fibre ring laser pulses.

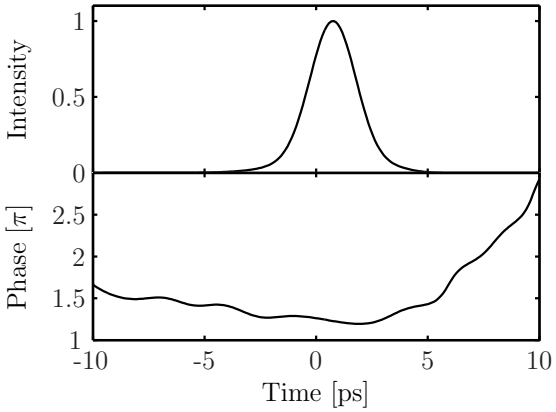

FIGURE 4.3: Intensity and phase retrieved from the spectrogram shown in Figure 4.2.

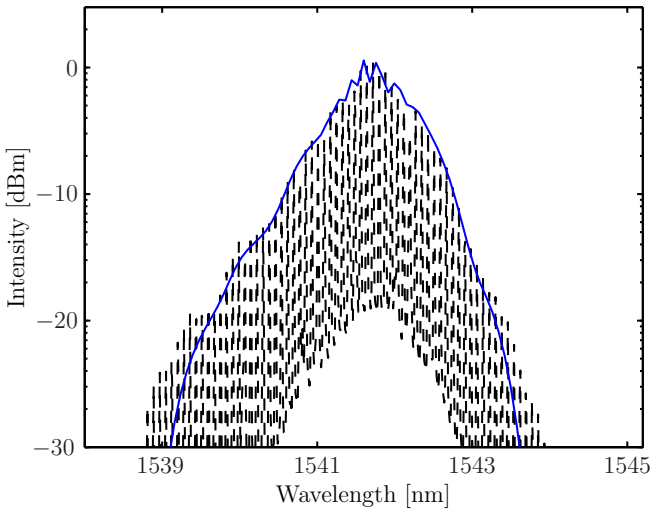

FIGURE 4.4: Spectrum retrieved from the spectrogram (blue), and independently measured (black, dashed).

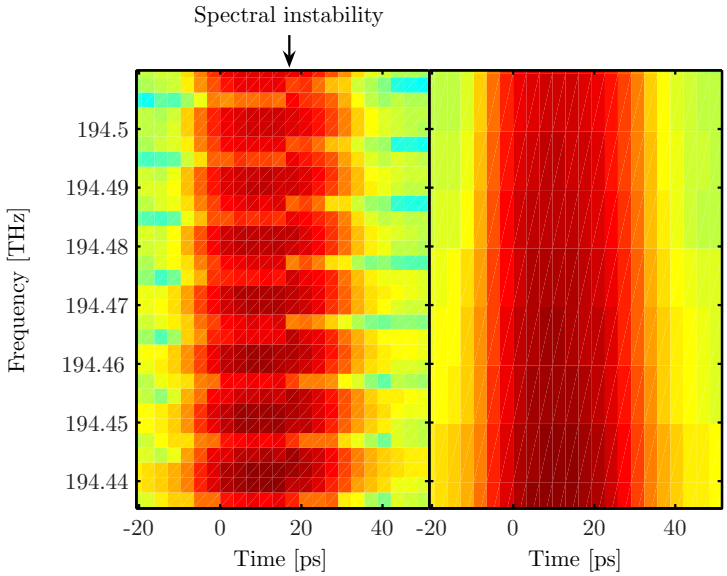

FIGURE 4.5: Detail of the spectrogram of a spectrally unstable pulse before (left) and after spectral envelope detection. The instability occurs where the arrow is pointing.

4.3 Rectangular pulses

4.3.1 Signal regeneration with rectangular-shape pulses

Dr. Periklis Petropoulos *et al.* first demonstrated the high quality generation of rectangular pulses using super structured fibre Bragg gratings [3]. Since then rectangular pulses have been used frequently in various optical pulse retiming experiments in our lab. Francesca Parmigiani *et al.* have recently described the reshaping and retiming possibilities with rectangular shaped optical pulses in [4]. Here, I will briefly describe the principles of operation.

A scheme for the retiming and reshaping of optical pulses is shown in Figure 4.6. The nonlinear optical loop mirror (NOLM) provides an optical switch based on the principle of cross-phase modulation. It consists of a Sagnac interferometer [2] built with highly nonlinear fibre, and an additional port for a control pulse. With accurate synchronisation, the control pulse (i.e. the reshaped pulse exhibiting timing jitter) co-propagates with one half of a locally generated clean optical pulse, which subsequently acquires a phase shift through cross-phase modulation. On recombination of the two halves of the locally generated signal in the 50/50 coupler, the phase difference between these two replicas determines which way the pulse is sent: i.e. transmitted or reflected by the NOLM.

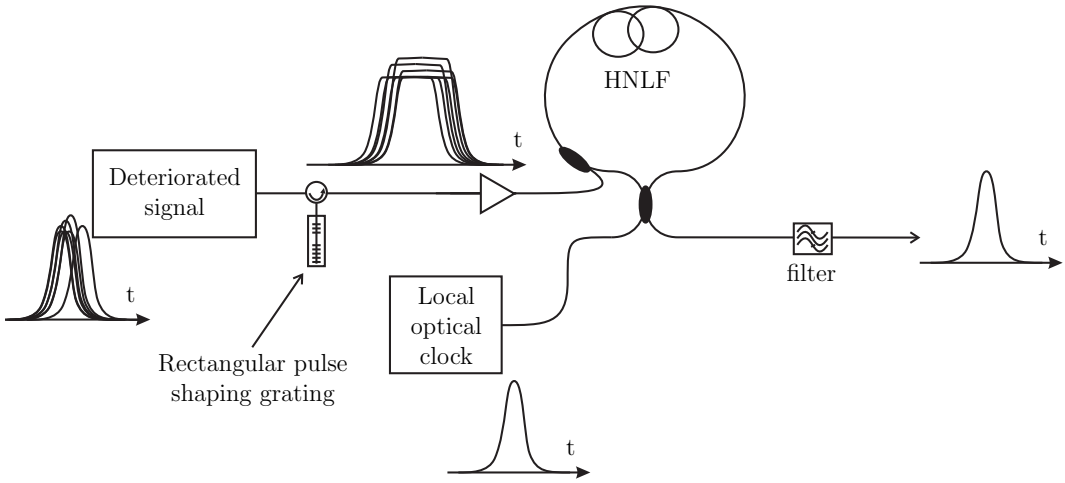

FIGURE 4.6: Scheme for retiming short optical pulses by reshaping them into rectangular pulses, and co-propagating them in a Sagnac NOLM with a locally generated optical clock signal. The output of the NOLM is a clean and retimed version of the optical signal.

The control pulses are formed by reshaping the 2.5 *ps* jittered input pulses into 20 *ps* long rectangular pulses, thus covering a significant part of the 100 *ps* bit slot. This means that the clean, locally generated pulse and the control pulse overlap even in case of severe timing jitter on the rectangular pulses. When the switching characteristic (as a function of the control peak power) has flat regions near its minimum and maximum peak transmittivity, the switching will also be insensitive to fluctuations in the power of the control pulses, and thus create clean regenerated pulses.
Variations on this scheme can be found in [4] and references therein.

Critical in these experiments is the quality of the rectangular pulses. Francesca Parmigiani has initially assessed these pulses with optical sampling experiments, and SHG-FROG traces. In the next section, I will compare the results from these experiments with EAM-spectrograms.

4.3.2 Characterisation

Measured and reconstructed EAM-spectrograms of 20 *ps* rectangular pulses are shown in Figure 4.7. The retrieved temporal intensity is compared with SHG-FROG and optical sampling traces in Figure 4.8. The EAM-spectrogram was measured at a much later date than the optical sampling and SHG-FROG traces, which made it impossible to reproduce precisely the same operating conditions and

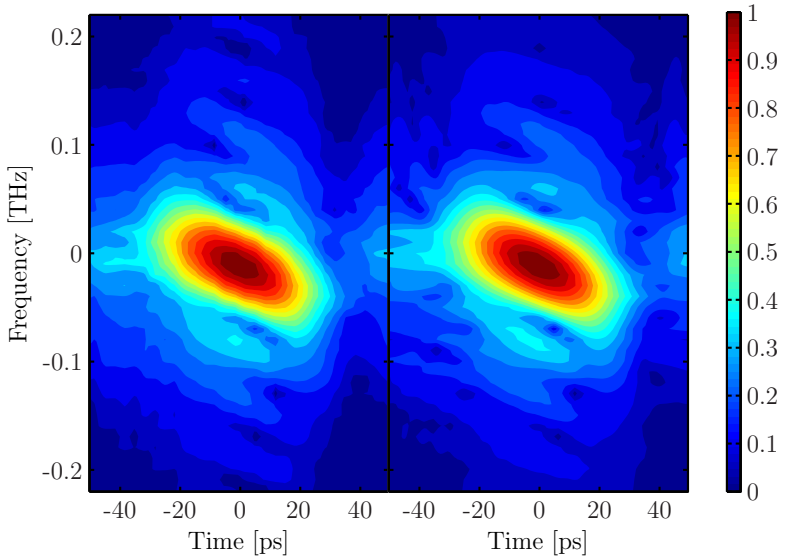

FIGURE 4.7: Measured (left) and retrieved (right) spectrogram of 20 *ps* rectangular pulses.

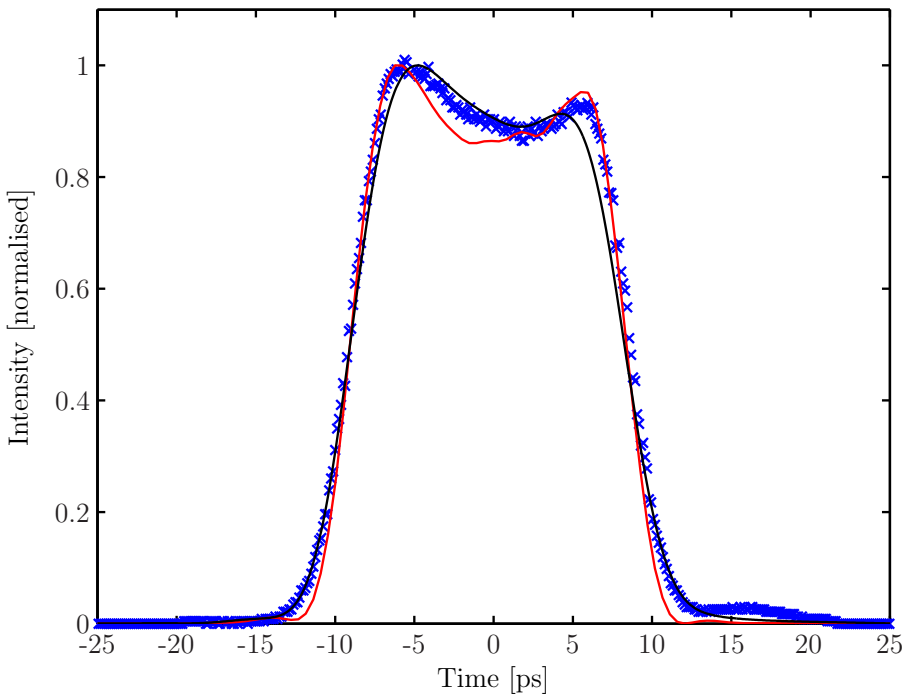

FIGURE 4.8: Intensity traces for the 20 *ps* rectangular pulses, measured in the following different ways: (blue ×): optical sampling, (black): EAM-FROG, (red): SHG-FROG.

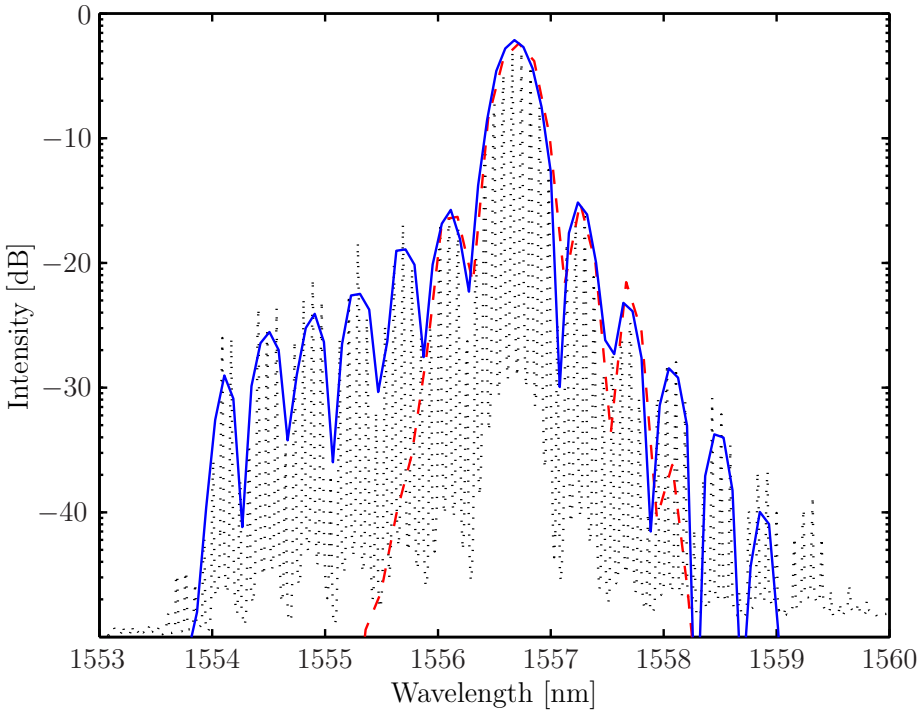

FIGURE 4.9: Spectral intensity traces for the 20 *ps* rectangular pulses, measured in the following different ways: (black, dotted): optical spectrum analyser, (blue): EAM-FROG, (red): SHG-FROG.

pulses. A slightly different tuning of the short pulse source with regards to the central wavelength of the grating therefore most likely explains the difference of the profiles at the higher intensities. The agreement between the EAM-spectrogram retrieval and the optical sampling trace at the edges of the pulse is remarkable though.

The spectral information gained from both spectrographic methods is compared with an independently measured spectrum in Figure 4.9. The typical $sinc^2$-shape is clearly visible, with neighbouring sidelobes having π phase shifts between them. Here, we can immediately see that the dynamic range in the SHG-FROG of only 13 *dB* severely limits the accuracy of the retrieved information. Only 2 sidelobes are resolved, the rest disappearing in the noise floor. The information retrieved from the EAM-spectrogram holds accurate information for nearly all the sidelobes the grating covers. The finer temporal features are thus more accurately resolved with the EAM spectrograms.

In the next section follows the closely related parabolic pulse, which can also be used in retiming experiments.

4.4 Parabolic pulses

The interest in pulses with a parabolic shape results from the fact that the derivative of its intensity profile is linear *across the whole pulse*, contrary to hyperbolic secant or Gaussian shaped pulses, where the derivative is only in first approximation linear across the *centre* of the pulse. The complete control given by fibre Bragg gratings to reshape short pulses has given us the possibility to create parabolic pulses in a simple and reliable manner. Francesca Parmigiani *et al.* have recently demonstrated a pulse retiming technique based on cross-phase modulation with parabolic pulses [5]. I will briefly summarise the principle first, and then continue with accurate characterisations of the parabolic pulses.

4.4.1 Pulse retiming using parabolic pulses

Cross phase modulation (XPM), for example between two co-propagating pulses in a highly nonlinear fibre, causes a frequency shift $\delta\omega(T)$ on the signal, which can be described as follows:

$$\delta\omega(T) = -\frac{\partial\phi}{\partial T} = -2\gamma P_o L_{eff} \frac{\partial \left|U(T-\Delta T)\right|^2}{\partial T}. \tag{4.2}$$

Here, γ and L_{eff} are the nonlinear coefficient and the effective length of the fibre respectively. P_o is the peak power of the 'control' pulse, and $U(t)$ is the normalised envelope amplitude of the control pulse and ΔT is the initial relative delay between the signal and the control pulse.

This equation shows that signal pulses that temporally overlap with the leading edge of a parabolic control pulse, acquire a red frequency shift, whilst pulses overlapping with the trailing edge of the pulse acquire a blue frequency shift. After propagation (Figure 4.10), the signal pulses, affected by timing jitter, have thus been shifted in the spectral domain, depending on their exact position relatively to the control pulse.

By now propagating these pulses in an appropriate amount of linearly dispersive optical fibre, the frequency shift is translated into a temporal shift, for each of the individual signal pulses, thus retiming them with respect to each other.

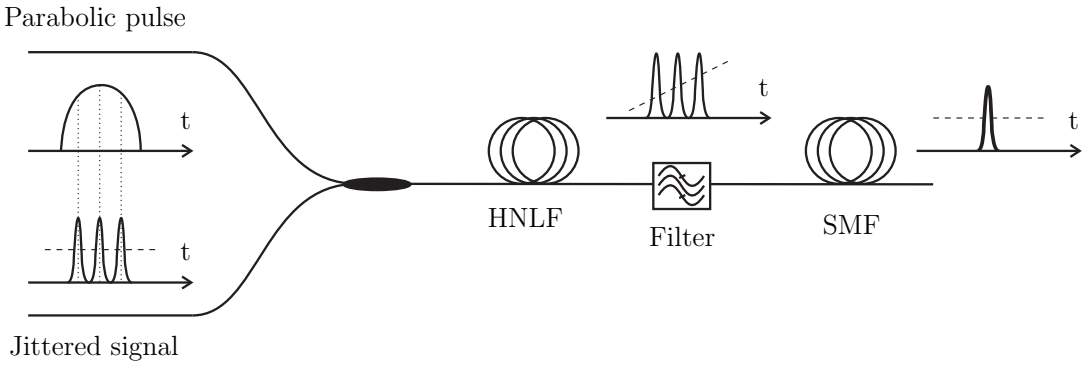

FIGURE 4.10: Scheme for retiming short optical pulses with parabolic pulses. The cross-phase modulation with a parabolic pulse induces a linear frequency shift. Propagation over 500 m of SMF will then retime the pulses because of dispersion.

It is clear that the exact shape of the intensity profile of these parabolic pulses is crucially important for this retiming technique. Again, the 2 *ps* fibre ring laser source was used as an input to the grating, which in this case created 10 *ps* long parabolic pulses. In the design for the grating, the pulse edges were smoothed with a fifth order Gaussian, which also reduced the spectral extent of the profile. The next section describes the characterisation of these pulses.

4.4.2 Characterisation

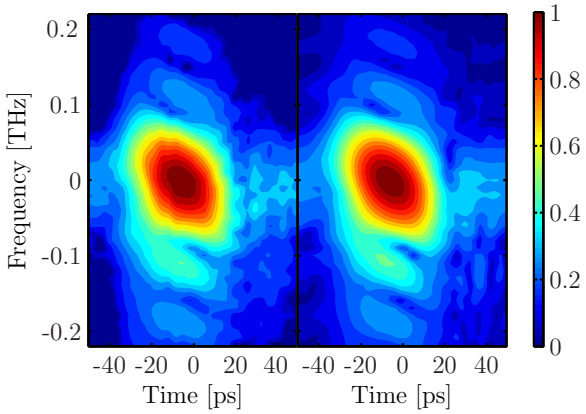

FIGURE 4.11: Measured (left) and retrieved (right) spectrogram of parabolic pulses, filtered from a 2.5 *ps* fibre ring laser pulse with a specially designed fibre Bragg grating.

Similarly to the rectangular pulses, the spectrum of the parabolic pulses consists of several side lobes. This is clear already in the EAM-spectrograms, shown in Figure 4.11. The retrieved temporal intensity is shown in Figure 4.12, together with the shape it was designed to be. The derivative of both the theoretical design

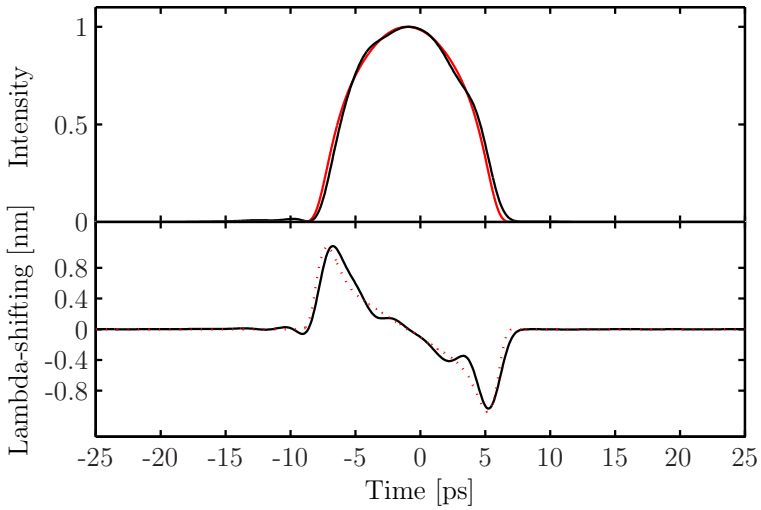

FIGURE 4.12: (top): Designed (red) and measured (black) intensity of the parabolic pulses, filtered from a 2.5 *ps* fibre ring laser pulse. (bottom): the wavelength shift (proportional to the derivative of the intensity profile) induced by the cross phase modulation with the parabolic pulse.

and the retrieved intensity is shown in the lower half of the figure. The deviation from a straight line towards the edges of the pulse is due to the super-Gaussian profile superimposed on the ideal parabolic shape.

Even though the intensity profile closely matches the design, the derivative has a distinct dip towards the leading edge of the pulse. The deviation from the linear profile is small though, and its effect on the retiming of signal pulses will be smoothed out when signal pulses with a duration of more than a few *ps* are considered.

4.4.3 Flat continuum generation

We have then continued to use this parabolic pulse source as the seed for ultra-flat supercontinuum generation. Due to the fact that self phase modulation induces a linear chirp to parabolic pulses, the pulse shape remains parabolic during nonlinear propagation in a normally dispersive fibre. This leads to the generation of a spectrum that is much flatter than can be achieved with hyperbolic secant shaped pulses [6]. The spectral ripple that arises from SPM of the sech shaped pulses and the effects of wave breaking (which cause a severe transfer of energy into the wings of the spectrum) can be avoided with a parabolic shaped pulse.

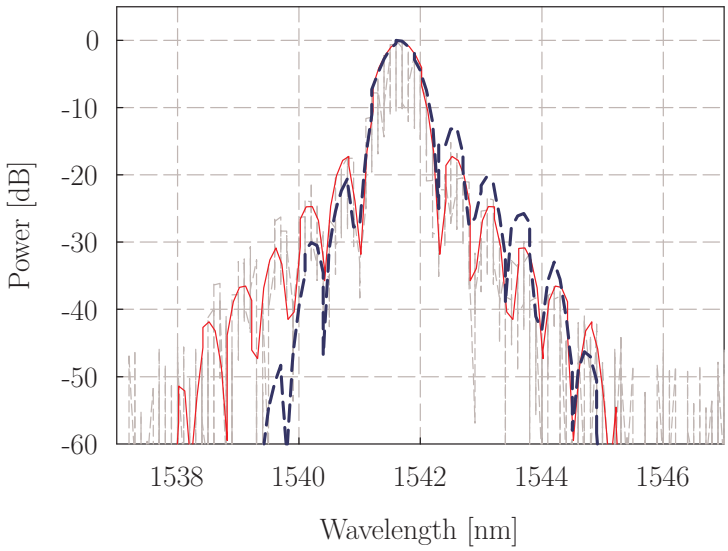

FIGURE 4.13: The spectrum of the parabolic pulse, measured with an optical spectrum analyser (gray), designed (red), and retrieved from the EAM-spectrogram (blue dashed).

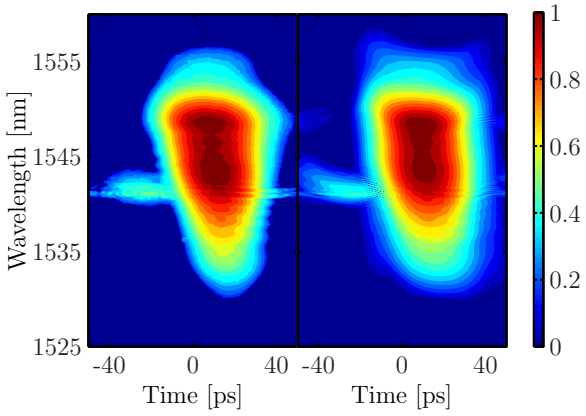

FIGURE 4.14: Measured (left) and retrieved (right) spectrogram of the parabolic pulses after spectral broadening in a highly nonlinear fibre.

We have amplified these 10 ps long parabolic pulses, with a repetition rate of 10 GHz, up to 27 dBm, before propagating them in a highly nonlinear fibre (length: $500m$, dispersion: $-0.87\ ps/nm/km$, slope: $-6.10^{-4} ps/nm^2/km$, nonlinear coefficient: $19W^{-1}km^{-1}$). Figure 4.14 shows the measured spectrogram of the spectrally broadened pulses. Compared with the independent spectral measurement, as shown in Figure 4.15, we can immediately see that the spectrogram is missing information towards the lower wavelength side. This is due to the steep increase in insertion loss for wavelengths below 1540 nm in the electro-absorption modulator (see also Section 5.2). The increase is in fact so detrimental that the signal completely disappears in the noise floor of the spectrogram measurement. This

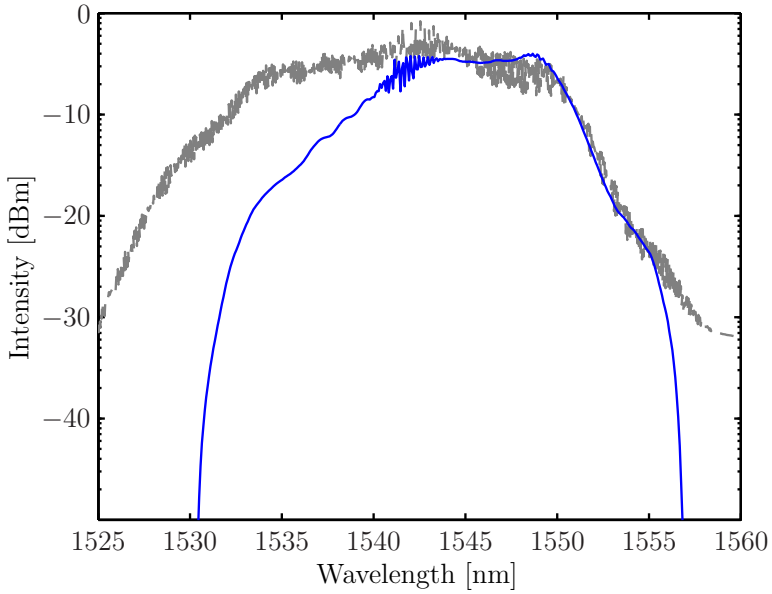

FIGURE 4.15: Spectrum of the broadened parabolic pulses, measured with an optical spectrum analyser (gray), compared with the spectrum retrieved from the spectrogram in Figure 4.14 (blue).

means that it is impossible to correct for this loss mathematically [7] before trying to deconvolve the spectrogram into its constituent pulse and gate information.

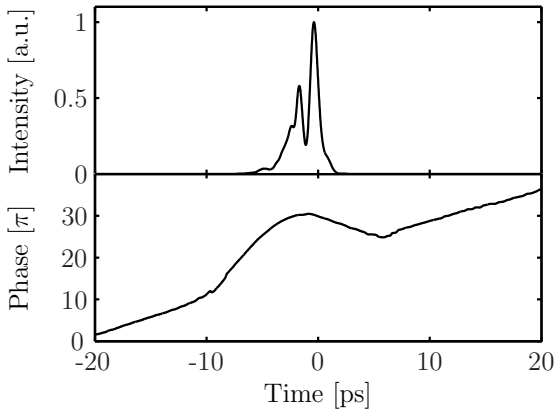

FIGURE 4.16: Intensity and phase for the broadened parabolic pulses, as retrieved from the spectrogram (fig. 4.14). Note the parabolic phase profile at the onset of the pulse, and the missing trailing side of the pulse (containing lower wavelengths).

The pulses are strongly chirped at this point. Even though the information retrieved from the spectrogram is bound to be incorrect, due to the fact that nearly half of the spectral information is missing, it is interesting to note that the temporal pulse profile has a parabolic like phase profile for at least the half of the pulse that has been resolved correctly (fig. 4.16).

It is clear that this is a limitation of the spectrogram technique which is purely related to the properties of the sampling EAM. With a modulator that has a broader operating spectrum, the method would deliver correct information. A modulator that seems to be a good candidate for this experiment could be a fast lithium niobate modulator, of which the main drawback would be the polarisation dependence. Otherwise, it is also possible to mathematically correct the spectrogram by multiplying it with a wavelength dependent slope, so that the lower wavelength components in the spectrogram are enhanced. In this case however, the wavelength dependent insertion loss induced by the modulator is so severe below 1538 *nm* that the signal disappears in the noise floor, which makes it impossible to correctly adjust the measured spectrogram.

For the EAM used here (Corning EAM-P n.MV2276A12.20), we have thus reached one of the limits of this spectrographic method: spectrograms reaching below 1540 *nm* should be interpreted with care, certainly when a significant proportion of the power of the pulse is situated at these wavelengths.

In the next part of this chapter, I continue to use fibre Bragg gratings, in order to reshape short pulses. Contrary to the pulses shown above, the emphasis of the characterisations below is on the temporal *phase* of the pulse.

4.5 OCDMA

4.5.1 Introduction

Next to the two main methods of multiplexing data (WDM and time domain multiplexing (TDM)), in order to achieve higher capacity and flexibility in transmission networks, there is a third player: code division multiple access (CDMA). CDMA is a spread spectrum broadcast technique that allows users to efficiently share transmission bandwidth in a flexible manner [8]. It is well-known in the field of radio communications, and has recently become a major research area in the field of optical telecommunications.

In OCDMA systems, a user is assigned a specific code which is used to label bits sent to and from that user. In the direct-sequence (DS) implementation, short optical pulses are transformed into OCDMA encoded waveforms, consisting of a

series of 'chips', on reflection from specifically designed FBGs. The chip sequence is a phase or intensity code, or a combination. However, the correlation properties of phase encoding permit higher extinction ratios than pure amplitude encoding. The phase encoding can for example be implemented with only 2 (binary), or with 4 (quaternary) different phase levels.

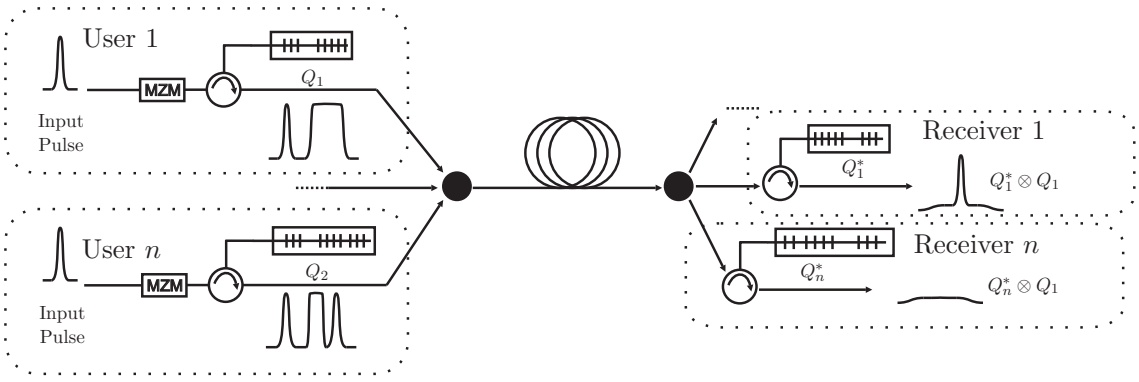

FIGURE 4.17: Simplified schematic of an OCDMA network with n users.

Figure 4.17 shows a simplified schematic of a possible implementation of an OCDMA network. The FBGs reshape the optical pulses into the coded pulse sequences Q_n, where each n represents a different user. The codes have the same temporal form as the spatial superstructure imprinted in the grating. The code is recognised at the receiver by a matched filter, which has the spatially reversed refractive index superstructure. When the encoding and decoding gratings are correctly matched, a pulse is generated: the code's autocorrelation. With unmatched gratings, the result is a cross-correlation between the two gratings. A carefully chosen set of codes with distinct autocorrelation characteristics and mutually low cross-correlation profiles is the key to obtaining a good discrimination between the codes, and minimises the effects of multi-user interference. Longer codes allow for a greater number of orthogonal codes and hence a greater number of simultaneous users on the network.

The waveforms used in OCDMA systems are thus deliberately chosen to be quite complex, and as with the other waveforms in this thesis, we decided to have a detailed look at them by trying to completely characterise their phase and intensity. Conventionally the quality of the coding or decoding is assessed by relying on electrical or optical sampling measurements combined with simple OSA measurements. However, these measurements are relatively crude and provide no direct information on the real quality of the phase coding. The accurate characterisation

of these gratings is critical though for understanding the operation and accuracy of fabrication of the superstructured FBGs.

4.5.2 OCDMA waveform characterisation

Because of its specific phase information, FROG immediately springs to mind as a means to characterise the waveform. However, because of the extreme complexity of these pulses, the spectrograms acquired from SHG-FROG would be very complex as well, making a good retrieval challenging, and making it difficult to assess for accuracy. Also the length of these waveforms does not favour SHG-FROG, which is only really suited to short pulses with high peak intensities.

The linear spectrogram technique based on creating spectrograms with the help of an electro-absorption modulator (Chapter 2) is a much better candidate. Not only can the spectrogram be made considerably simpler: a cross correlation between the single pulse gating function and the OCDMA waveform; the linear spectrograms are also much more sensitive. This allows us to achieve much higher temporal resolution and accuracy because of the increased dynamic range.
However, because of the long pulse lengths, and their complex shape, the characterisation setup needs to be modified. The main issue here is to find a suitable electrical signal that is synchronised to the OCDMA waveform, and with a duration that is comparable to the chip duration of the waveform. In the next section, we start with measurements on waveforms that incorporate just a single phase shift between two chips. With this we will be able to verify the phase encoding capability of fibre Bragg gratings, and check that we can use linear spectrograms to get a high resolution view on the waveforms created by these gratings. In later sections, we examine much more complex chip patterns. These experiments have been performed in close conjunction with the ORC's fibre grating fabrication group.

4.5.3 Single phase shift

One can consider a 50 mm long, uniform grating with a phase shift in the middle as a 2-chip code with a chip duration of 25 ps, related to the 25 mm length (spatially) of the chip. The characterisation setup is only slightly different from the schemes shown in Chapter 2. Here, the grating that generates the OCDMA waveforms is

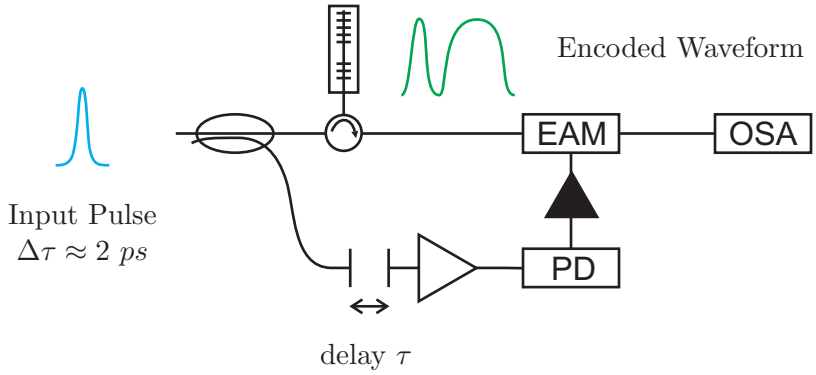

FIGURE 4.18: Linear spectrogram acquisition setup adapted for characterisation of 50 *ps* long, single phase shift SSFBGs

inserted in the optical path, just before the sampling EAM, as shown in Figure 4.18. We ensured that we measured a *complete* spectrogram of the waveform by gating down the initial 10 *GHz*, 2 *ps* ring laser pulses to a repetition rate of 5 *GHz*, so that we are able to scan a 200 *ps* window. However, we were then limited to using electrical amplifiers working at this repetition rate, meaning that the gating duration is about 50 *ps* due to the lower rise and fall times achieved. This in turn elongates somewhat the temporal intensity features in the spectrogram[1]. The 200 *ps* window is still sufficient though, and contains all the relevant information.

We characterised the temporal response of four different phase shifted SSFBGs using this setup. The 50 *mm* uniform gratings have an abrupt phase shift at their centre. The four phase shifts investigated are $\pi/2$, π, $3\pi/2$ and 0, or no phase shift, i.e. just a uniform grating. The 3 *dB* spectral bandwidth of the uniform grating is around 0.3 *nm*, and the peak reflectivity around 50%. The spectral bandwidth of the 2 *ps* pulses that we use as an input to these gratings is around 1 *nm*, which means that the pulse spectrum is reasonably flat over the grating's bandwidth. This ensures that the reflected, shaped optical pulse is close to the impulse reponse of the grating.

Figure 4.19 shows the measured and reconstructed spectrogram of a 2 *ps* pulse reflected from a $\pi/2$ phase shifted grating. Along the spectral axis, we can see *sinc*-like features, which are related to the rectangular temporal pulse shape. There is excellent agreement between the measured and reconstructed spectrograms over a large dynamic range (> 40 *dB*). Note that the intensity features are varying

[1]Recall that the spectrogram is the spectrally resolved cross-correlation between the waveform under test and the gating function. The length of the intensity feature in the spectrogram is thus determined by this cross-correlation.

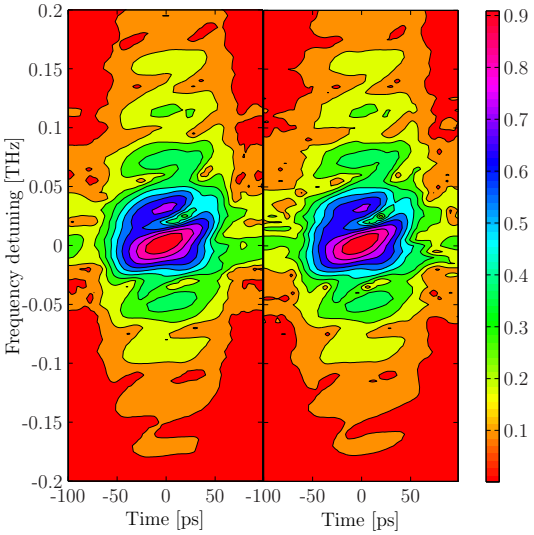

FIGURE 4.19: Measured (left) and reconstructed (right) spectrogram for uniform grating with a $\pi/2$ phase shift in the middle.

quickly along the spectral axis, but slowly along the temporal axis.

Figure 4.20 shows the temporal phase and intensity profiles for the four waveforms. For reference, the calculated, ideal profiles are also displayed. For these simulations, we used the transfer matrix method, which can also take the grating strength into account [9]. The input pulse used for the simulations is a hyperbolic secant shaped pulse, with a duration of 2.2 *ps*. It is remarkable to find such good agreement between the two, especially considering the fact that the 'sampling' window is more than an order of magnitude longer than the quick temporal features found in these waveforms. This relates to the fact that the information is stored along the frequency axis in the spectrogram. The rise and fall times of these features are determined by the duration of the grating's input pulse.
The width of the writing beam to fabricate the fibre Bragg gratings is around 100 μm [10], which relates to a duration of 1 *ps* for the light reflecting from the grating. This means that the phase shift is only completed after about 1 *ps*. Bearing this in mind, the phase difference between two points on each side of the phase shift, 2 *ps* away from the phase shift was calculated, for the three different gratings and the results are shown in table 4.1. There is a slight difference between the nominal spatial phase shift written in the fibre grating and the corresponding temporal phase shift. This is because of the fact that the gratings are strongly reflective ($\approx 3dB$). As is already clear from Figure 4.20, the agreement is very good.

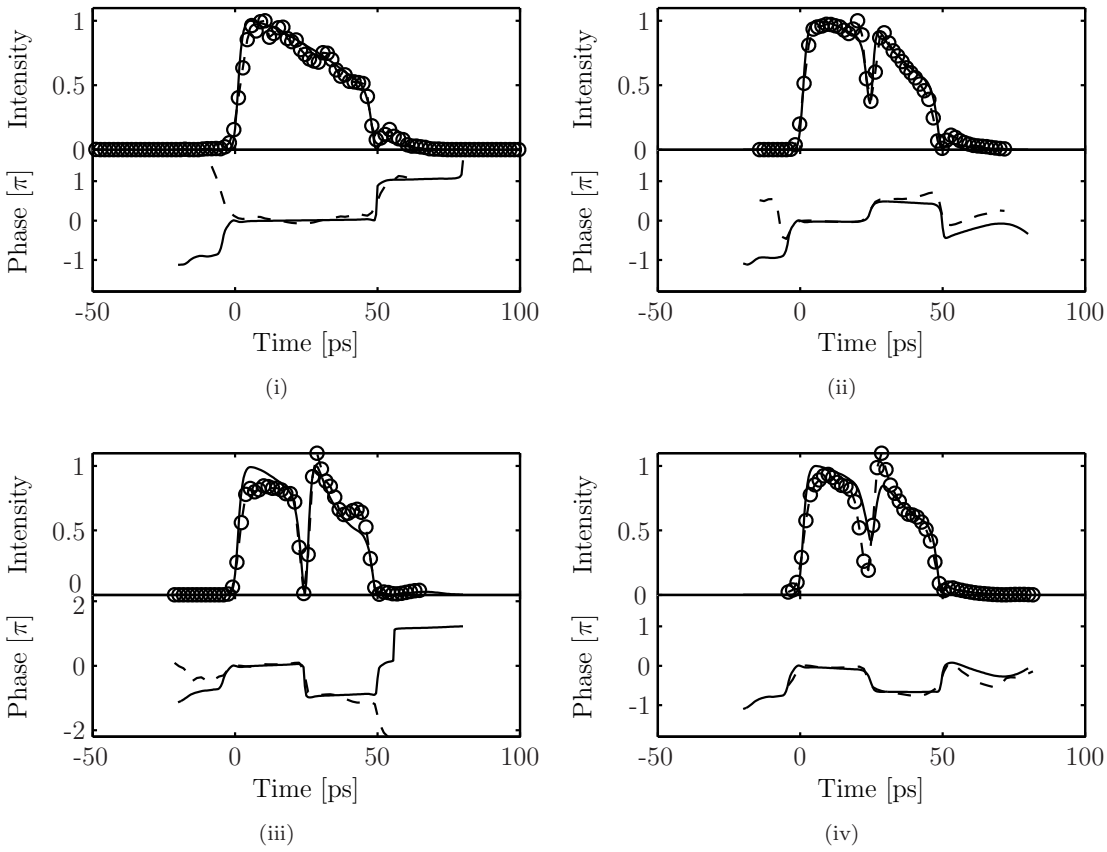

FIGURE 4.20: The intensity and phase profiles of 4 uniform gratings with central phase shifts of respectively 0, $\pi/2$, π and $3\pi/2$ for figures (a)-(d). The full line represents the theoretical prediction from numerical simulations, the dashed line (with circles on the intensity graphs) is the data retrieved from the linear spectrogram method.

Nominal spatial phase shift	Simulated temporal phase shift	Measured temporal phase shift
0.5π	0.48π	0.53π
π	1.02π	1.03π
1.5π	1.45π	1.40π

TABLE 4.1: Nominal, simulated and measured phase shifts in single phase shift gratings.

Figure 4.21 illustrates the influence of the limited – though still broad enough – spectral bandwidth of the input pulse: the designed grating reflection spectrum is shown, together with the corresponding measured reflection spectrum. This was done by measuring the reflection of broadband ASE, generated by an EDFA without optical input, from the grating. The third curve on these graphs shows the retrieved spectral intensity of the 2 *ps* pulses reflected from the respective gratings. This is in fact the product of the grating reflection spectrum and the

spectrum of the input pulse. There is very good overlap with the grating reflection spectrum over the central (1 nm) region, but the limits of the finite bandwidth pulse are clearly visible in the wings. The total bandwidth of the gratings thus easily surpasses the bandwidth of the very short (2 ps) optical pulse.
The greatest difficulty in making these particular measurements has been the spectral instability of the short pulse source. Due to mode hopping of the ring laser during the acquisition (approx. 5 min) of the spectrograms, an accurate mapping of the measured spectrogram onto a Fourier grid is more difficult. Several of the pre-processing techniques mentioned in Section 2.5.2 were used to mitigate the effects of this mode hopping (in particular, the enveloping function was used on each spectral slice, and a suitable 2-D Fourier transform filter, in order to smoothen out any noise artefacts).
Even though these simple gratings with only a single phase shift between two chips have virtually no practical significance, it has been interesting to verify this phase encoding and the characterisation setup. I will present very similar measurements later on in this chapter, which have much more practical significance: the verification of temperature induced phase shifts in fibre Bragg gratings. In the next section, I will continue first with the characterisation of more complex phase encoded fixed gratings.

4.5.4 Complex 16 chip codes

Confident with the results of the single phase shift gratings, we continued with the measurement of more challenging phase encoding. We used 16-chip, 4-level phase encoded waveforms which are well suited for OCDMA experiments. The chip duration is again 25 ps, which means that the duration of the waveform now becomes as long as 400 ps. Assuming the same gating window duration of 50 ps, we expect to have a spectrogram where the intensity is spread out over roughly 500 ps. Therefore, we gated down the repetition rate of the pulses to 1.25 GHz, corresponding to a period of 800 ps.
A 200 ps delay line alone clearly does not suffice to measure the whole spectrogram. We solved this problem by using two pattern generators to drive two modulators, one in each arm (see Figure 4.22). These gate the repetition rate down from 10 GHz to 1.25 GHz, independently, but synchronised, so that we get two short, 1.25 GHz pulses: one for code generation and one for driving the sampling EAM. Initially, the bit pattern in the delay arm is set to (1000000), one bit represents

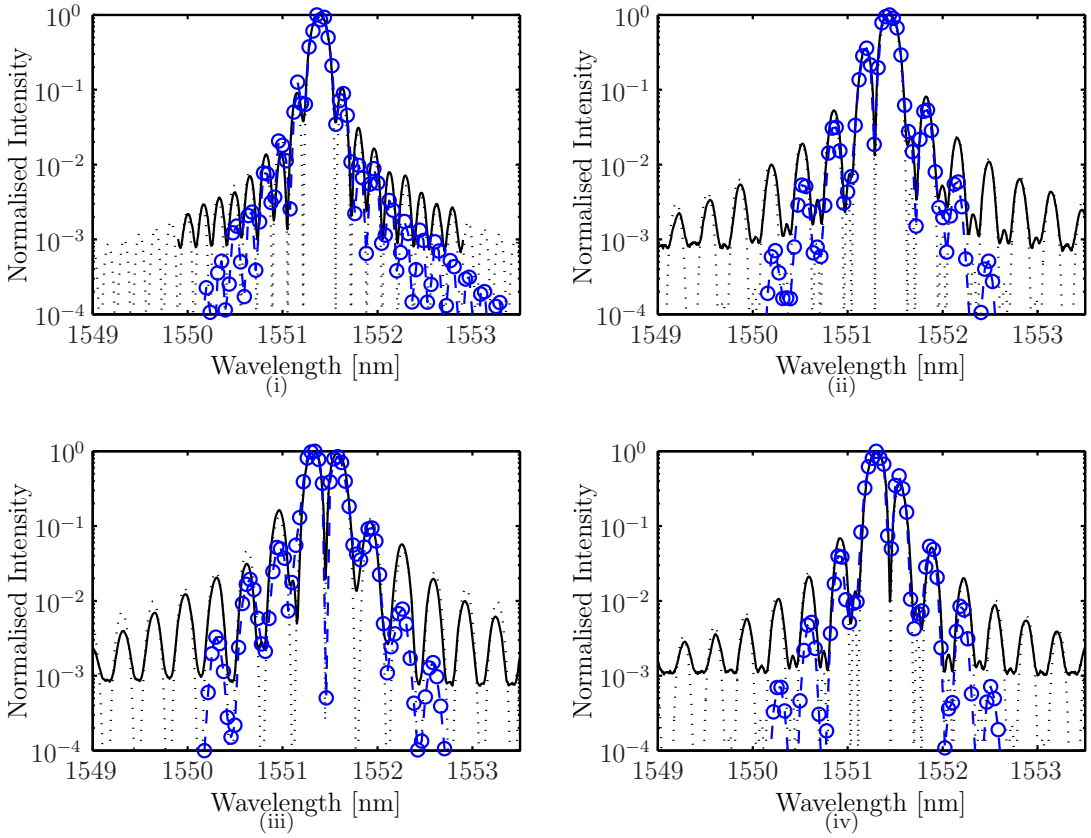

FIGURE 4.21: The reflection spectrum of the grating (full line) measured with an OSA by reflecting broadband ASE from the grating and its theoretical design (dotted line). The retrieved intensity of the pulse response is plotted in blue (dashed line with circles), for 4 uniform gratings with a central phase shift of 0, $\pi/2$, π and $3\pi/2$ for figures (a)-(d) respectively.

100 *ps*. The spectrogram is now acquired for just over 200 *ps*, by scanning the tunable delay. Next, the pattern is changed to (00100000), and another 200 *ps* part of the spectrogram is acquired. This process is repeated until the whole spectrogram is acquired. The 4 individual spectrogram parts are then stitched together to provide a spectrogram spanning the full 800 *ps* delay range. Then we perform the usual mathematical processing that prepares the information to be fed into the deconvolution algorithm (see Section 2.5).

The input pulse used this time is a chirp compensated EAM carved pulse, with a duration of 23 *ps*. This pulse duration is thus barely shorter than the chip duration of the code. Even though the phase changes in the grating are still abrupt, the waveform's phase changes will be smoothed out due to this fairly long pulse duration. This is however a more realistic implementation of an OCDMA encoder

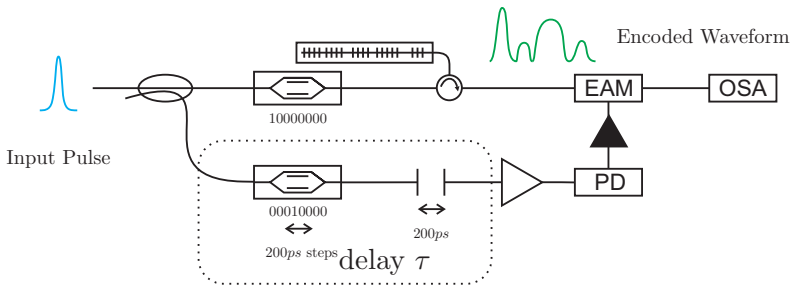

FIGURE 4.22: Extended spectrogram acquisition setup to accommodate for long waveforms. Two synchronised 10 *GHz* pattern generators are used to drive the modulators.

than using a 2 *ps* input pulse from an expensive ring laser, and it is still possible to obtain nice auto- and cross-correlation properties in the decoder. A great advantage here is the stability of this source. As with measuring the original EAM-carved pulses (Section 3.3), no special preprocessing of the spectrograms is needed.

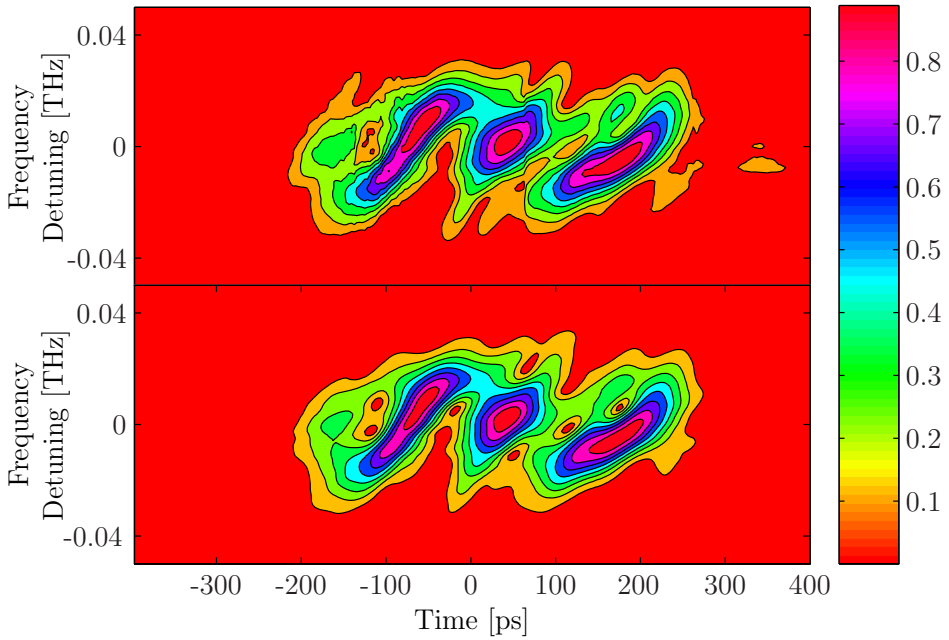

FIGURE 4.23: Measured (top) and reconstructed (bottom) spectrogram of a 16 chip OCDMA grating encoded pulse.

The measured and reconstructed spectrograms are shown in Figure 4.23. Contrary to the broad bandwidth, single phase shift experiments, there is now more information stored along the temporal axis: the waveform has a much narrower bandwidth, determined by the input pulse, and is much longer which is in this case determined by the length of the code (16 chips).

Note that the nominal spectral resolution of the optical spectrum analyser is

1.25 *GHz* (or 0.01 *nm*), which is sufficient to sample the 1.25 *GHz* repetition rate pulse at the Nyquist limit.

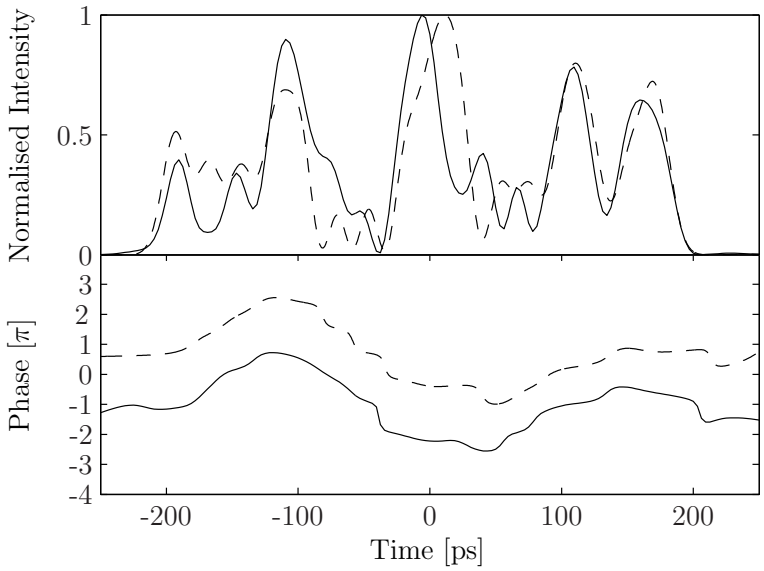

FIGURE 4.24: Measured (full line) and simulated (dashed line) intensity and phase of a 23 *ps* pulse reflected from a 16 chip OCDMA grating.

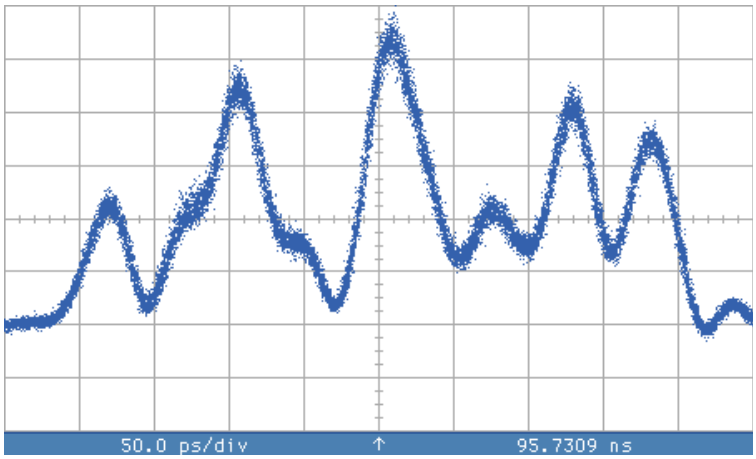

FIGURE 4.25: Intensity of a 23 *ps* pulse reflected from a 16 chip OCDMA grating, measured with a 20 *GHz* photodiode and an electrical sampling oscilloscope.

Still, as in many *undersampled* FROG spectrograms [11], the deconvolution gives accurate results, as is shown in Figure 4.24. For comparison, the simulated pulse intensity and phase calculated by reflecting a 23 *ps* pulse from the idealised grating is also shown (dashed lines), using the transfer matrix method [9]. The theoretical prediction of the phase profile shows excellent agreement with the measured phase. As pointed out earlier, the phase changes smoothly between the different chips in

the waveform, because of the long input pulse. The intensity agrees only to a certain extent. Preliminary simulations show that this could be due to a wavelength offset and minor phase errors in the fabricated grating. Small phase changes can cause considerable intensity differences, making it challenging to exactly simulate the intensity profiles. However, the primary function of the grating is the coding of the phase, which is as shown here and in the next section, very good.
Figure 4.25 shows the intensity of the encoded pulses measured with an electrical sampling oscilloscope and a 20 *GHz* photodiode. Apart from the ringing effects because of the limited bandwidth of the photodiode, the agreement with the intensity retrieved from the spectrogram, shown in Figure 4.24, is very good.
To our knowledge, it is the first time that such complex encoded OCDMA waveforms have been measured in such a direct way. This not only shows the accuracy of the pulse characterisation, but also allows us to confirm directly the accurate phase encoding capability of specifically designed SSFBGs for optical code division multiple access (OCDMA). We have published some of these results [12, 13, 14].

Higher resolution

Even though a very good idea of the phase code is already obtained in the previous section, the rather long input pulse (23 *ps*) disguises some of the phase shifts. A better resolution can be obtained with a shorter input pulse. We have repeated the measurements above with a DCF compressed gain switched laser pulse. The input pulse with a duration of 6 *ps*, is reflected from the same coding grating used previously. We can already see much more detail in the spectrogram (see Figure 4.26). Looking at the retrieved results in Figure 4.27, we can now clearly distinguish between the chip slots, and the phase profile is almost an exact copy of the theoretical code of the grating: [0 3 1 0 1 1 2 0 3 2 2 2 3 1 1 1 0], where one unit means a $\pi/2$ phase difference relative to the previous chip. This code is essentially equivalent to [0 -1 1 0 1 1 -2 0 -1 -2 2 2 -1 1 1 1 0], which is the one displayed as blue line segments in Figure 4.27.

The measurements in the last two sections demonstrate the linear spectrogram technique applied to two extreme optical waveforms in terms of their phase and intensity properties: large bandwidth pulses with very fine temporal features, as well as very long waveforms with a narrower bandwidth. The great accuracy of

the retrieved information in both cases makes this an ideal technique for assessing the coding and decoding performance of such gratings in OCDMA networks.

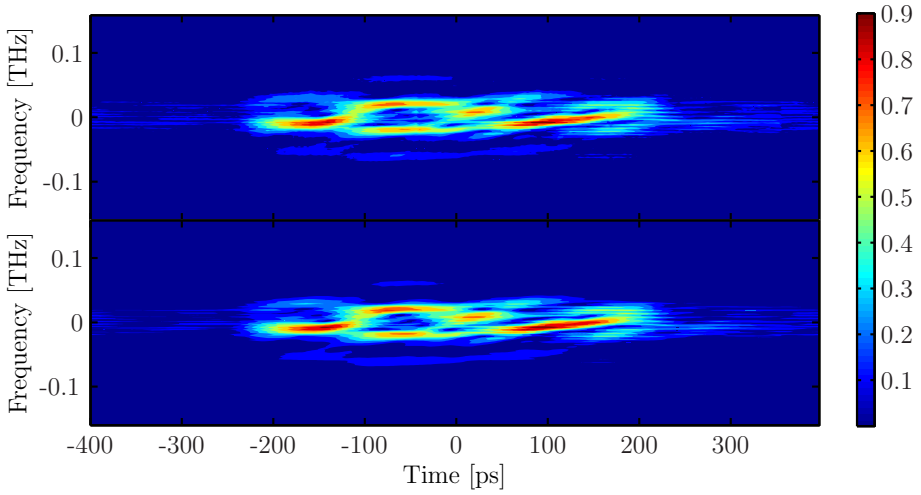

FIGURE 4.26: Measured (top) and reconstructed (bottom) spectrogram of 6 *ps* gain switched pulses reflected from the same 16 chip coding grating as in Figures 4.23, 4.24 and 4.25 (retrieval error 0.01 on a 128×128 point grid).

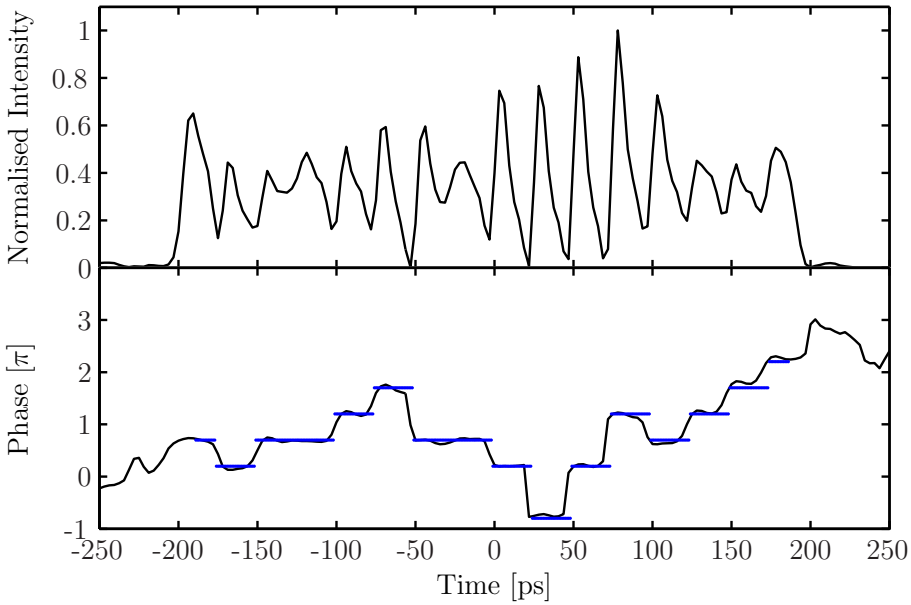

FIGURE 4.27: Intensity and phase retrieved from the spectrogram shown in Figure 4.26. The blue segments represent the theoretical code.

4.5.5 Temperature tunable codes

The gratings mentioned and characterised in this chapter are key elements in OCDMA networks, and have the potential to dramatically improve the granularity of the optical transmission systems. However, unlike in radio communication

systems, where different codes can be generated and used instantaneously, the gratings that encode and decode the OCDMA waveforms are conventionally fixed. Changing the code means that one has to physically switch the gratings, which is not desirable in a reconfigurable network.

Unsurprisingly, there is great interest in techniques that would bring the same flexibility to optical CDMA, so that codes can be changed on demand. One way of implementing tunable phase shifts is to locally change the refractive index of the fibre (that has a uniform grating written into it), by heating the fibre. A principle sketch is shown in Figure 4.28.

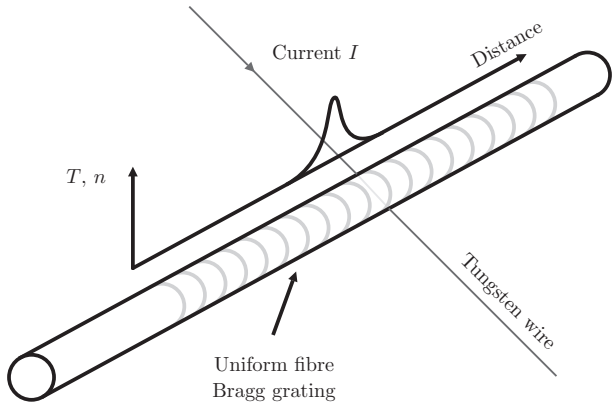

FIGURE 4.28: A fibre Bragg grating with a current-tunable phase shift in the middle. The current through the tungsten wire causes local heating, which changes the refractive index.

Assuming the distribution of the refractive index along the fibre is $\Delta n_{eff}(x)$, the resultant phase shift can be calculated as

$$\phi = \frac{4\pi}{\lambda_B} \int_{x_1}^{x_2} \Delta n_{eff}(x) dx, \tag{4.3}$$

where λ_B is the Bragg wavelength of the grating. The grating fabrication group at the ORC has been working on inducing a distributed phase shift in the grating by putting a fine tungsten wire in contact with the uniform grating. When electric current passes through the wire, the heat produced by this will affect the grating because the temperature increase causes an increase in the local dc refractive index of the fibre. This consequently produces a phase shift in the grating. If the electrical current on the tungsten wire is tuned, different temperature distributions

and thus different current-induced phase shifts can be obtained. The grating fabrication group has recently demonstrated OCDMA encoders and decoders based on this kind of tunable phase shifts [15, 16].

We have been able to contribute to the research in this area by characterising the spatial refractive index profile in fibre Bragg gratings. The spatial refractive index distribution of the grating is related to the temporal phase of its pulse response, and as a result, it can be directly retrieved from the latter.

If a short optical pulse is reflected from the grating under test, the reflected pulse response is a good approximation to its impulse response. If the FBG is weak, the spatial phase of the grating will cause an equivalent temporal phase in its impulse response due to space-time duality. The magnitude of the spatial phase shift of the grating can be approximately obtained from the magnitude of the temporal phase in its impulse response. Differentiating (4.3) with respect to x gives:

$$\Delta n_{eff}(x) = \frac{\lambda_B}{4\pi}\frac{d\phi}{dx}. \tag{4.4}$$

The time-to-space conversion relationship tells us that:

$$\Delta t = \frac{2n_{eff}\Delta x}{c}. \tag{4.5}$$

These two equations lead to the relationship between the dc refractive index distribution of the FBG and the temporal phase distribution of its impulse response:

$$\Delta n_{eff} = \frac{\lambda_B n_{eff}}{2\pi c}\frac{\Delta\phi}{\Delta t}. \tag{4.6}$$

Hence, knowing the temporal phase distribution of its impulse response leads immediately to the spatial refractive index profile of the FBG. The same principle also leads to the characterisation of other spatial properties of FBGs, such as the chirp or discrete phase shifts.

The FBG under test in this case is a 17 *mm* long uniform grating. The tungsten wire was placed in contact with the grating at 8 *mm* from one of its ends. The input pulse is a 23 *ps*, 10 *GHz* chirp-compensated EAM-carved pulse, gated down to 2.5 *GHz* for compatibility with the 170 *ps* long waveform we expect.

The setup of the characterisation scheme is the same as in Figure 4.18. The intensities and phases of the pulses are measured for four different currents through the tungsten wire, and the results are shown in Figure 4.29. The applied currents are

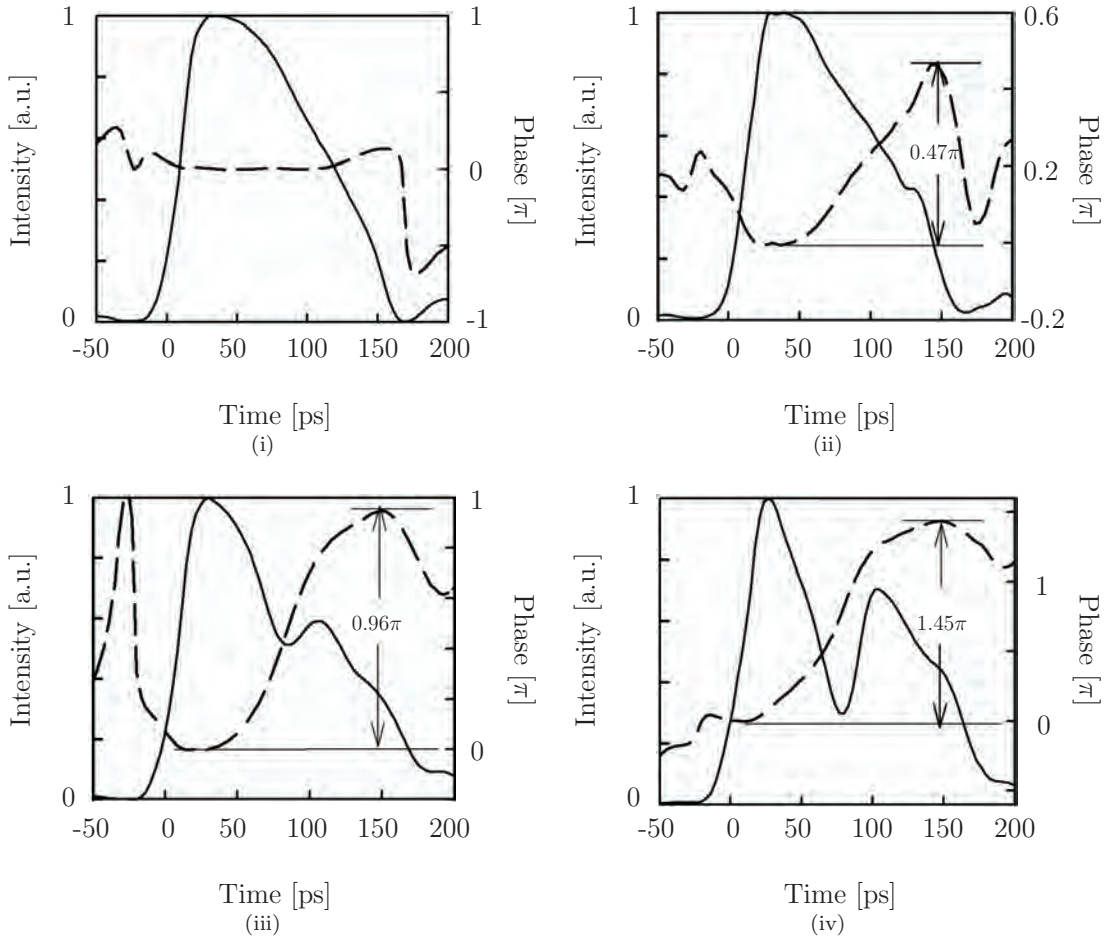

FIGURE 4.29: Measured intensity (solid line) and phase (dashed line) of the pulses reflected from the FBG when the electrical currents along the tungsten wire are 0, 52, 70 and 84 mA for figures (a)-(d) respectively.

0, 52, 70 and 84 mA. The phase shifts obtained with these settings are 0, 0.47π, 0.96π and 1.45π respectively. Using equation 4.6, we obtain the effective refractive index profiles induced by these currents. The small background refractive index profile on the uniform grating is probably due to the non-uniformity of the fibre core.

Note that the spatial resolution of the dc refractive index profile is limited by the input pulse width. With a pulse duration of 23 ps, the spatial resolution is thus approximately 2.3 mm.

The strength of the grating also affects the measurement accuracy. As the strength of the grating increases, the equivalence of the amplitude of spatial and temporal phase shift gradually breaks down. To investigate whether or not the measurement of the spatial refractive index in this way still makes sense, Mr. Zhang, of the

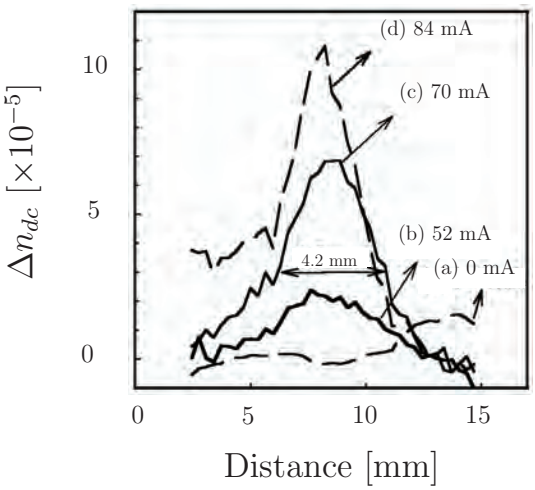

FIGURE 4.30: Spatial refractive index distributions for currents of (a) 0 mA, (b) 52 mA, (c) 70 mA and (d) 84 mA, calculated from the temporal phase of the pulse response of the grating.

fibre gratings group, simulated the different steps involved in this measurement: starting with a 17 mm long uniform grating, with a peak reflectivity of 66% and a certain dc refractive index profile, the reflection from the grating of a 23 ps pulse is calculated. From this response, the spatial dc refractive is calculated again, analogously to the measurement (Figure 4.31).

The recalculation of the phase shift in this way reveals that there is only a small deviation: the retrieved phase shift is slightly less (0.93π) than the initially determined π phase shift. This is due to the relatively high peak reflectivity of the grating. There is also a discrepancy towards the rear end of the grating, which is also due to the high reflectivity. Simply stated: less light is propagating to the rear end of the grating.
Even with such a high reflectivity, there is still very good agreement, and these simulations show that obtaining the refractive index by measuring the pulse response of the grating is a reliable characterisation.

4.6 Conclusions

By characterising some very complex optical waveforms generated by reflecting short pulses from FBGs, we have not only gained valuable information about those waveforms, but we have also tested the linear spectrogram technique in extreme situations, and have found very satisfying and encouraging results.

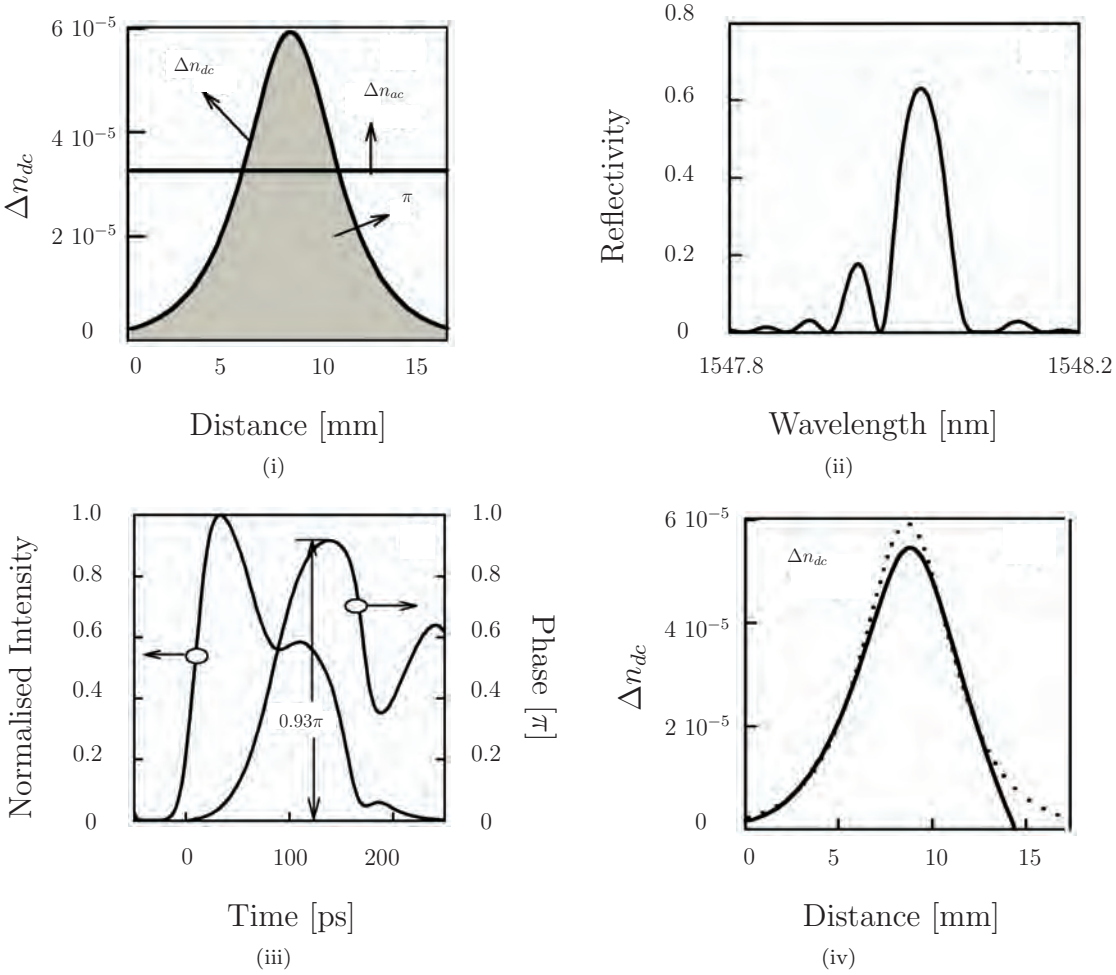

FIGURE 4.31: Consistency check to assess the accuracy of the method used to calculate the spatial refractive index: (a) The predetermined ac and dc refractive index profiles inducing a π phase shift, (b) the obtained spectral reflectivity, (c) the intensity and phase of the pulse response of the grating and (d) the recalculated spatial refractive index from the data in figure (c).

After verifying individual phase shifts in uniform gratings specifically fabricated for this investigation, we were able to extend the measurements to more complex encoded pulses. The phase and intensity information gained from the 16-chip OCDMA optical codes is useful for example for either confirming the correct operation of the gratings and perhaps also for further optimisation of the system in which they will be employed.

The characterisation of the temperature tunable phase shifted gratings in particular has led to a unique look at how good the performance of these very interesting devices can be. We now have a much better idea of the induced temperature distribution along the fibre.

Most grating characterisation methods have thus far focussed on the intensity

reflection and the continuous chirp profile, and use a setup based on an interferometer for example [17]. Only recently, significant advances have been made in the field of complete interferometric characterisations of FBGs without restrictive a priori assumptions [18]. To our knowledge however, this is the first time that a spectrographic technique is used to assess complex gratings with *multiple* phase shifts in a detailed and direct way. Moreover, the linear spectrogram method is easily scalable to even longer and more complex gratings.

I believe that these characterisations are very valuable in order to assess the accuracy of the pulse shaping gratings, and to confirm that the gratings are behaving as expected. Any inconsistencies with the design should be carefully investigated. Because the waveforms are fully characterised, computational simulations based on this information may be useful to find out how to mitigate any imperfections in the grating fabrication.

It should also be possible to gain very accurate information about the best performance possible in experimental setups, with the supplied gratings. These calculations will give information with a much higher validity than can be achieved using the theoretical design alone.

References

[1] A. Othonos, "Fiber Bragg gratings," Review of Scientific Instruments **68**, 4309 – 41 (1997).

[2] G. Agrawal, *Applications of Nonlinear Fiber Optics* (Academic Press, 2001).

[3] P. Petropoulos, M. Ibsen, A. Ellis, and D. Richardson, "Rectangular pulse generation based on pulse reshaping using a superstructured fiber Bragg grating," Journal of Lightwave Technology **19**, 746 – 52 (2001).

[4] F. Parmigiani, P. Petropoulos, M. Ibsen, and D. Richardson, "All-optical pulse reshaping and retiming systems incorporating pulse shaping fiber Bragg grating," Journal of Lightwave Technology **24**, 357 – 64 (2006).

[5] F. Parmigiani, P. Petropoulos, M. Ibsen, and D. Richardson, "Pulse retiming based on XPM using parabolic pulses formed in a fiber Bragg grating," IEEE Photonics Technology Letters **18**, 829 – 31 (2006).

[6] D. Anderson, M. Desaix, M. Karlsson, M. Lisak, and M. Quiroga-Teixeiro, "Wave-breaking-free pulses in nonlinear-optical fibers," Journal of the Optical Society of America B (Optical Physics) **10**, 1185 – 90 (1993).

[7] K. W. DeLong, M. A. Krumbugel, D. N. Fittinghoff, J. N. Sweetser, R. Trebino, G. Taft, A. Rundquist, E. Zeek, M. M. Murnane, and H. C. Kapteyn, "Systematic error and its elimination in the measurement of 10-femtosecond laser pulses," Conference on Lasers and Electro-Optics Europe - Technical Digest **11**, 436 (1997).

[8] L. Ahlin and J. Zander., *Principles of Wireless Communications* (Studentlitteratur, Lund, Sweden, 1998), second edition edn.

[9] T. Erdogan, "Fiber grating spectra," Journal of Lightwave Technology **15**, 1277 – 94 (1997).

[10] F. Ghiringhelli, *Fundamental properties of Bragg gratings and their application to the design of advanced structures*, Ph.D. thesis, University of Southampton (2003).

[11] R. Trebino, "SC155: The Measurement of Ultrashort Laser Pulses," Frontiers in Optics 2005, Tucson, Short course notes (2005).

[12] M. Roelens, C. Tian, Z. Zhang, P. Petropoulos, M. Ibsen, and D. Richardson, "Full characterisation of the temporal response of complex phase shifted Bragg gratings for OCDMA using frequency resolved optical gating," 31st European Conference on Optical Communication **2**, 315 – 16 (2005).

[13] C. Tian, Z. Zhang, M. A. F. Roelens, M. Ibsen, P. Petropoulos, and D. J. Richardson, "Reconfigurable all-optical header recognition for packet switched networks," e-Photon/ONE Summer School, Pisa & Cesenatico, 30 Aug - 2 Sep (2005).

[14] C. Tian, Z. Zhang, M. A. Roelens, P. Petropoulos, M. Ibsen, and D. J. Richardson, "Full characterisation of the temporal response of phase-shifted SSFBGs using electroabsorption modulator based frequency resolved optical gating." BGPP/ACOFT 2005, Sydney, 4-9 Jul (2005).

[15] C. Tian, Z. Zhang, M. Ibsen, M. Mokhtar, P. Petropoulos, and D.J.Richardson, "Reconfigurable all-optical packet switching based on fiber Bragg gratings," Optical Fiber Conference 2006, Anaheim 5-10 Mar (2006).

[16] Z. Zhang, C. Tian, M. Mokhtar, P. Petropoulos, D. Richardson, and M. Ibsen, "Rapidly reconfigurable phase code generation and recognition using fiber Bragg gratings," Optical Fiber Conference 2006, Anaheim 5-10 Mar (2006).

[17] S. Barcelos, M. Zervas, R. Laming, D. Payne, L. Reekie, J. Tucknott, R. Kashyap, P. McKee, F. Sladen, and B. Wojciechowicz, "High accuracy dispersion measurements of chirped fibre gratings," Electronics Letters **31**, 1280 – 2 (1995).

[18] A. Ozcan, M. Digonnet, and G. Kino, "Characterization of fiber Bragg gratings using spectral interferometry based on minimum-phase functions," Journal of Lightwave Technology **24**, 1739 – 57 (2006).

Chapter 5

High capacity systems

5.1 Introduction

In the previous chapters, I have documented the characterisation of several specific pulses and waveforms. The respective experiments already showed the usefulness of the linear spectrogram method for understanding individual components and their functions. This chapter describes the application of the spectrograms to high capacity *systems*.
In the first part, the compatibility of linear spectrograms with synchronous wavelength division multiplexing systems is examined, as the broad optical bandwidth of the gating function of the EAM lends itself naturally to the sampling of many channels simultaneously. In the second part, a novel modulation format in a high speed optical transmission system is accurately characterised. The phase and intensity of these pulses is then measured after transmission over an installed fibre link.

5.2 Wavelength division multiplexing

The huge bandwidth offered by standard, single mode optical fibre can really only be used effectively when different wavelength channels are multiplexed together. Currently, these wavelength division multiplexed (WDM) systems are being made available commercially at individual channel rates of 40 $Gbit/s$, and existing systems with 10 $Gbit/s$ channel rates are being upgraded to higher channel rates.

The advantage of having higher channel bit-rates rather than increased numbers of lower bit rate channels, is that less equipment is needed and the total capacity might be optimised, because the channel filtering can be made more effective. However, nonlinear effects, chromatic and polarisation mode dispersion are increasingly difficult to mitigate at higher bit rates, making the technology to realise 40 $Gbit/s$ systems more challenging.

One very appealing property of all optical networks is their capacity for parallel processing of many channels simultaneously, without the need to demultiplex. The broad gain bandwidth of erbium doped fibre amplifiers for example allows for amplification of the signal power across the whole C-band (1525–1565 nm). The ever increasing distances over which optical signals are sent, and the increasingly flexible nature of optical networks [1], demand more comprehensive performance monitoring of all the channels than provided by the classical bit-error rate testing, or optical spectrum analyser traces.

Bit error rate measurements on each individual channel to monitor the performance of the network would be too expensive, and unnecessarily complicate the system in any event. Usually, signal monitoring is performed with a simple spectrometer, which measures the average optical spectrum of the WDM signal. Both bit error rate measurements and monitoring with a spectrometer provide insufficient information when it comes to finding out what exactly might be going wrong in the network: is there residual dispersion (chromatic or polarisation), or are nonlinearities adversely affecting the signal quality?

In this section, I look to extend the linear spectrogram technique, as presented in a previous chapter, to simultaneously characterise pulses in different WDM channels. The advantage is that the technique makes it possible to exploit the potential of optical systems for parallel processing, in the same way as the spectrometer does, whilst yielding more information about the pulses, i.e. the phase, and with that interesting temporal information. The idea of using broadband spectrograms based on sampling with a single modulator leads to a very simple and inexpensive, but versatile signal monitoring setup. Because of its simple practical implementation, it could also be a valuable field tool. A practical setup involving only a single modulator, a spectrometer, a clock recovery circuit and an electronic or optical delay unit can be made very compact.

As an alternative for a real, installed fibre network, we implemented a recirculating loop, as will be discussed in Section 5.2.4. Recirculating optical fibre loops are frequently used in labs, to perform initial experiments on new technologies.

The spectrogram method is easily adapted to measure the optical signal after a desired number of round trips in the loop we have constructed, and allows us to investigate the optical signal more deeply than was previously possible. With this, we show that the linear spectrogram measurement method is a valuable lab tool.

5.2.1 Experimental setup

The linear spectrogram acquisition setup is easily adapted so that it can handle WDM signals, see Figure 5.1. The mere insertion of a spectral filter before the photo-detector suffices. This filter selects one particular channel, which is again converted to a synchronised electrical signal. Assuming that the different WDM channels are all synchronised, this single electrical signal can sample all the channels together. Each channel will then relate to an individual intensity feature in the spectrogram.

To create the WDM signal which we used to perform the experiments, we mul-

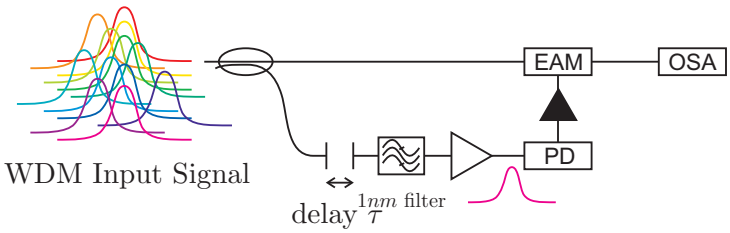

FIGURE 5.1: Linear spectrogram acquisition setup for a WDM signal.

tiplexed an array of continuous wave DFB laser signals together with an arrayed waveguide grating (AWG). Pulses are carved simultaneously using a single modulator: either an overdriven $LiNbO_3$ Mach-Zehnder modulator (see Section 5.3.4), or an electro-absorption modulator. Both options are shown in Figure 5.2.

Both of these sources have their advantages and disadvantages. The Mach-

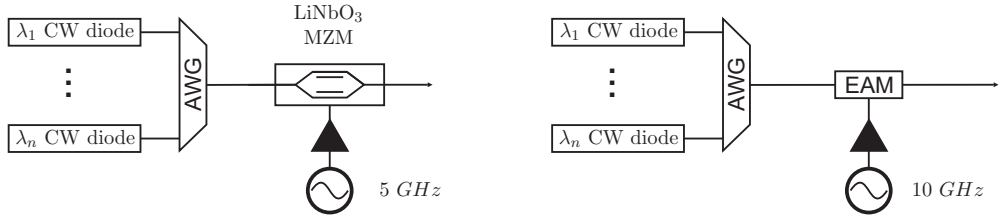

FIGURE 5.2: WDM signal source for synchronous 10 GHz pulse carving of n different wavelengths, left with a Mach Zehnder modulator and right with an electro-absorption modulator.

Zehnder modulator is very much less wavelength sensitive across the C-band in terms of insertion loss. However, it is polarisation sensitive, and the polarisation of all channels has to be carefully aligned before the setup can be used. Also, due to wavelength dispersion in the waveguides of this modulator, it becomes impossible to optimise the bias voltage on one of the MZM arms for a wide band ($> 10\ nm$) of wavelengths simultaneously. With a bias optimised for the central channels, minor 5 *GHz* components can be noticed on the optical signal, when using the setup shown in Figure 5.2, left.
The electro-absorption modulator on the other hand is much less polarisation sensitive ($< 1dB$), and produces pulses with an exact repetition rate of 10 *GHz*. However, it has a wavelength dependent insertion loss. The latter problem is overcome though by pre-equalising the powers of the individual CW lasers so that after pulse carving, the channels are all aligned power-wise.

5.2.2 WDM spectrograms

Initially, we chose the Mach-Zehnder modulator to do the synchronous pulse carving. Eight CW lasers are selected with an interspacing of 200 *GHz* (1.6 *nm*), and individual wavelengths between 1550 and 1560 *nm*. The 1560 *nm* channel is then filtered out with a 1 *nm* optical filter, to provide the electrical driving signal for the sampling EAM in the spectrogram acquisition setup.
Figures 5.3a and b show the measured spectrograms of this WDM signal before and after propagation over 350 *m* of standard single mode fibre. The effect of the fibre dispersion is immediately observed by comparing the relative positions of the individual channel intensity features. The skew of each of the individual features is also indicative of the chirp on the pulses, however, the balanced MZM creates chirp free pulses, and here, the skew is dominated by the chirp imposed by the EAM sampling itself.

The spectrogram is reconstructed as a whole here (interpolated on a 512×512 point grid), delivering a single gating function and a combined spectral field of all the channels together. The individual channels are obtained by mathematically filtering them out from this WDM signal field in the spectral domain. A Fourier transform of these individual fields then gives us the temporal intensity and phase

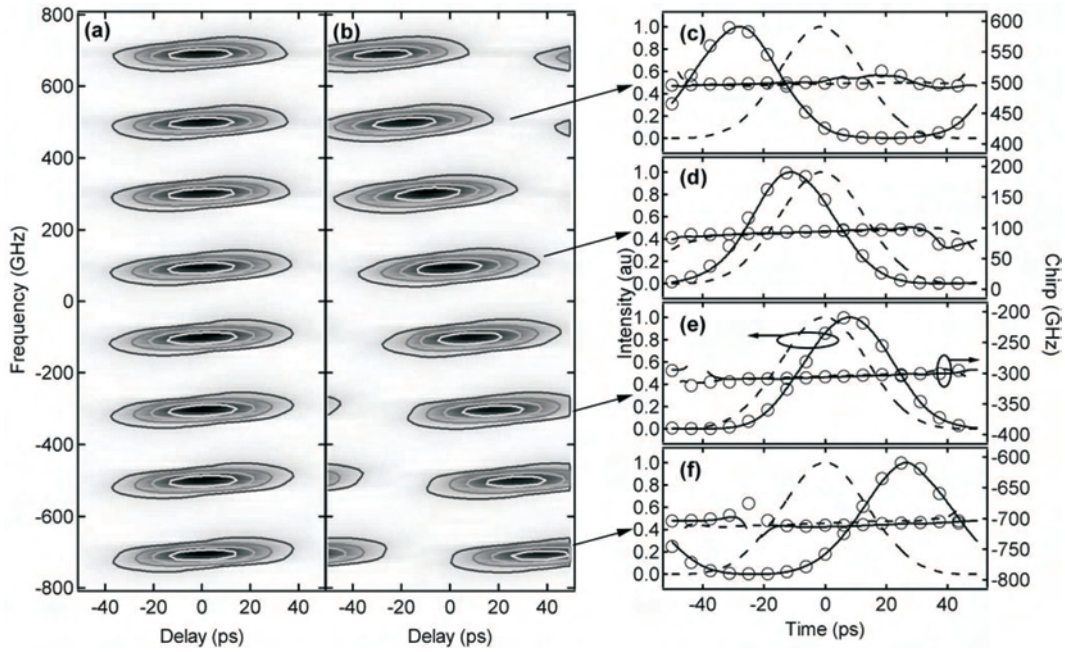

FIGURE 5.3: Experimentally measured spectrograms of an eight wavelength channel (200 *GHz* spacing), 10 *Gbit/s* pulse stream before (a) and after (b) propagation through 350 m of SMF28 (The square root of the spectrogram intensity is plotted here to highlight the 40 *dB* dynamic range of the measurement). (c-f) Shows the intensity and chirp before (dashed line) and after (solid line) propagation, retrieved from the measured spectrograms (only four channels are shown for clarity). The intensity and chirp (circles) from a simulated propagation of the fields before the fibre shows excellent agreement with the directly measured results.

for each channel.

The spectrogram retrieval error is around 0.005 for both measurements and the retrieved spectra agree well with the independently measured spectra. Another consistency check reveals some of the power of this characterisation scheme: Figure 5.3c-f show the intensity and chirp of the 4 individual channels before and after propagation over the short amount of fibre. The circles represent the intensity and chirp of the pulses obtained from a simulated propagation, using the NLSE split-step method [2], of the retrieved fields before transmission. There is almost perfect overlap with the measurement data.

The information obtained from these spectrograms is thus very valuable. Not only do we get the individual pulse characteristics, we also get the relative timing between the various channels. The information can be used to perform propagation simulations, or to fine-tune various parameters in the system, such as amplifier or equaliser levels and tunable dispersion compensator settings.

As will be shown further in this chapter (Section 5.3.3), it is also possible to

perform the measurement on PRBS (pseudo random bit sequence) modulated signals, where the average phase and intensity of the pulses will be characterised.

5.2.3 Limiting factors

There are a number drawbacks to this characterisation system though. First of all, the channels have to be synchronised, otherwise the intensity feature of the unsynchronised channel will be smeared out across the full period of the spectrogram. At the end of the 1990's, there has been great interest in synchronously modulated WDM systems. The cost of regeneration of all the signals is considerably reduced when the all the channels can be processed simultaneously [3, 4, 5, 6]. In a review of WDM technology and applications, Keiser mentioned in 1999 that an issue that still needed to be resolved is the monitoring, to assure that the pulses (solitons in this case) are propagating properly [7]. The WDM characterisation technique presented here is fully compatible with these WDM soliton systems, and would yield the most complete information regarding the WDM signal and the regeneration performance.

Secondly, not only is the insertion loss of the sampling EAM wavelength dependent, the gating duration also changes with wavelength, as is shown in Figure 5.4. The wavelength dependent insertion loss is readily accounted for by renormalising the spectrogram using the independently measured insertion loss. The wavelength dependent duration of the gating function means essentially that the spectrogram needs to be split up before mathematical reconstruction when the gating function becomes too different for the lowest and highest wavelength channel. The difference in deconvolution results is shown Figure 5.5. Here, the dashed red curve is

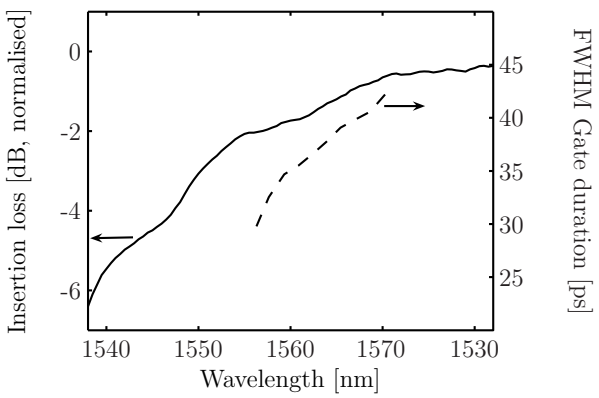

FIGURE 5.4: Corning EAM-P n.MV2276A12.20 insertion loss (full line, $V_{pp} = V_{bias} = 0\ V$) and gate duration (dashed, $V_{pp} = 5\ V$, $V_{bias} = 2.8\ V$, at 10 GHz) measured as a function of the wavelength.

the intensity of a pulse filtered out from the total deconvolved WDM field (with a span of around 10 *nm*), whilst the black curve is the intensity profile retrieved from the mathematically reduced spectrogram. Thus, when the spectrogram is *not* broken up into individual spectrograms for each channel, the intensity for the retrieved pulse field is distorted by the single gating function retrieved for the whole spectrogram.

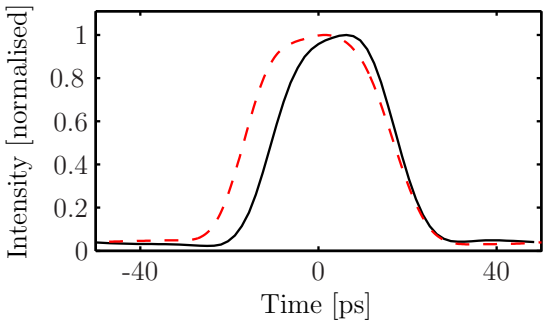

FIGURE 5.5: Temporal intensity for a single pulse, retrieved from mathematically filtering the total field retrieved from the complete spectrogram (dashed red), compared with the intensity retrieved from the individual spectrogram slice for the respective channel (black).

This is certainly not a disadvantage though, as in fact, there are less calculations needed to reconstruct several individual spectrograms (32×32 points) compared to a single big one (512×512 points). The relative timing information between the channels can still be obtained from the spectrogram immediately, as illustrated in the next section.

Last, but not least, there should not be any spectral overlap between the channels after they have been sampled with the EAM. If there is a spectral overlap, the reconstruction algorithm will link the phase of the individual channels, assuming that they are coherent. This will result in incorrect intensity and phase information, much in the same way as the sidemodes in the gain switched laser measurements, see Section 3.2. Note that even when the original WDM signal field has spectrally separated channels, they can still become spectrally overlapping when they have been modulated by the sampling EAM.

5.2.4 Recirculating loop

During the course of my Ph.D., I have helped to construct another useful building block for performing transmission experiments. With a limited amount of fibre in

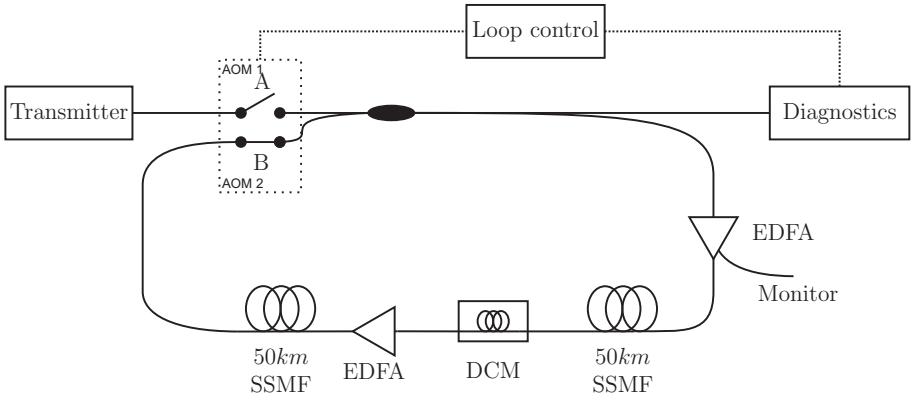

FIGURE 5.6: Scheme of the recirculating loop, controlled with acousto-optic modulators (AOM) and consisting of two 50 km spools of standard single mode fibre (SSMF), and a dispersion compensating fibre module (DCM).

a laboratory, it is possible to mimic long-haul optical transmission links by recirculating the optical signal in a loop configuration. The schematic of the loop I have built is shown in Figure 5.6. The idea is that with correct timing settings on the acousto-optic modulators, the light inside the fibre can be circulated around the loop a predetermined number of times. The exact timing is dependent on the speed of the light in the fibre, the total length of the loop and the desired number of round trips of the optical signal.

The loop configuration for the experiments below consists of two spools of 50 km of SSMF, compensated in the middle by a fibre dispersion compensating module. This module is designed to compensate both second and third order dispersion for 100 km of standard single mode fibre (SSMF). The optical signal is amplified before being launched into both 50 km spools of fibre.

In Figures 5.7 and 5.8, I show that the multi-wavelength sampling technique is applicable to recirculating loop experiments, and that the technique reveals the residual third order dispersion properties of a fibre link. The figures show respectively the spectrograms for 10 synchronously EAM-carved WDM channels after zero, one and two circulations in the loop. These spectrograms were then broken into individual 64×64 point spectrograms for each channel before they were mathematically reconstructed. The retrieved pulse intensities and phases are shown in the middle and right graphs of Figures 5.7 and 5.8 respectively. The optical power per channel going into the sampling EAM for these measurements was around -7 dBm (total optical signal power of 3 dBm). This was chosen to maximise the signal to noise ratio on the spectrum analyser, whilst not exceeding the maximum nominal input power to the EAM ($5dBm$). With a more sensitive spectrometer, the required power level of the optical signal can be reduced.

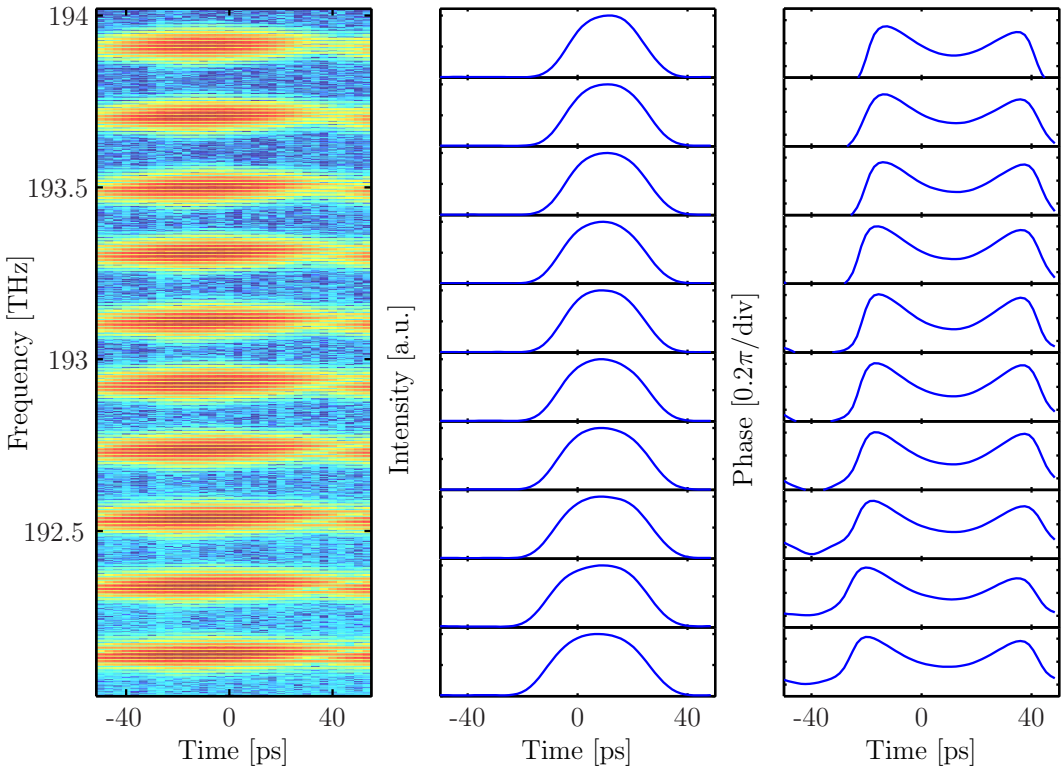

FIGURE 5.7: (left): Measured spectrogram of 10 EAM-carved WDM channels. (middle and right): retrieved temporal intensity and phase for each wavelength channel.

What becomes clear as the number of circulations increases, is the distinct curvature of the arrival time as a function of the central wavelength of the individual pulses. This is due to the residual third order dispersion of the fibre span. This residual dispersion has also been measured independently with a group delay measurement setup [8]. The result is shown as the blue curve on the spectrogram after a single loop, and is simply multiplied by two to obtain the group velocity dispersion after two circulations. Both match the arrival time of the individual pulses as seen on the spectrogram.

The retrieved intensity information after transmission shows some modulation, and the generation of low level ghost pulses (as indicated by the arrows), where the intensity was zero before transmission. These artefacts are attributed to four wave mixing interactions between the different channels during propagation in the fibre, a known deleterious effect in WDM systems with equidistant channel spacings. This is evidenced by the creation of ghost channels at wavelengths 200 *GHz* below and above the range of the 10 WDM channels, as indicated in Figure 5.9.

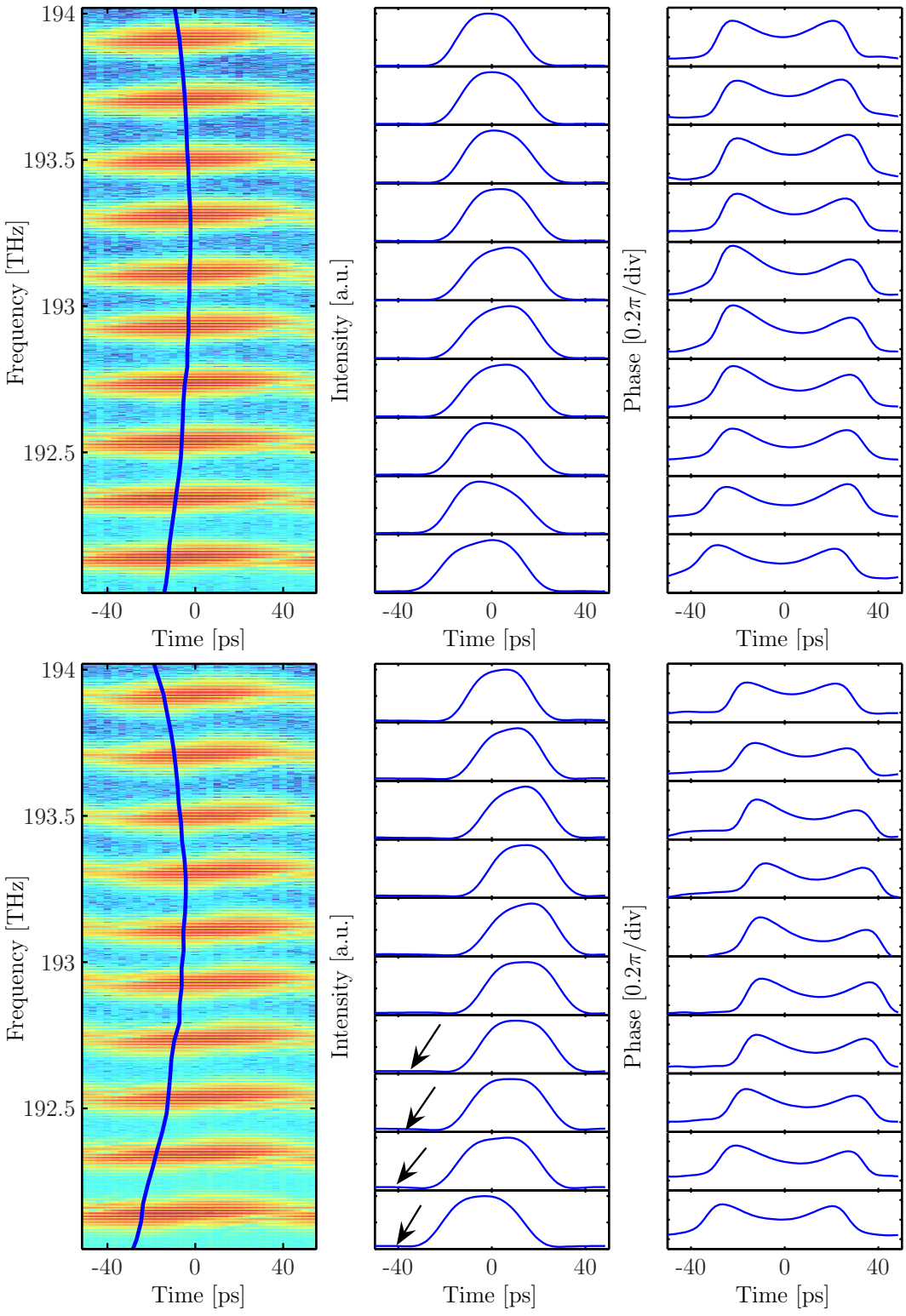

FIGURE 5.8: (left): Measured spectrogram of 10 EAM-carved WDM channels after one and two circulations in the loop (top and bottom). The blue line represents the independently measured group velocity dispersion of the loop (multiplied by two for the lower figure). (middle and right): retrieved temporal intensity and phase for each wavelength channel respectively. The arrows in the intensity plots indicate the evidence for ghost pulses.

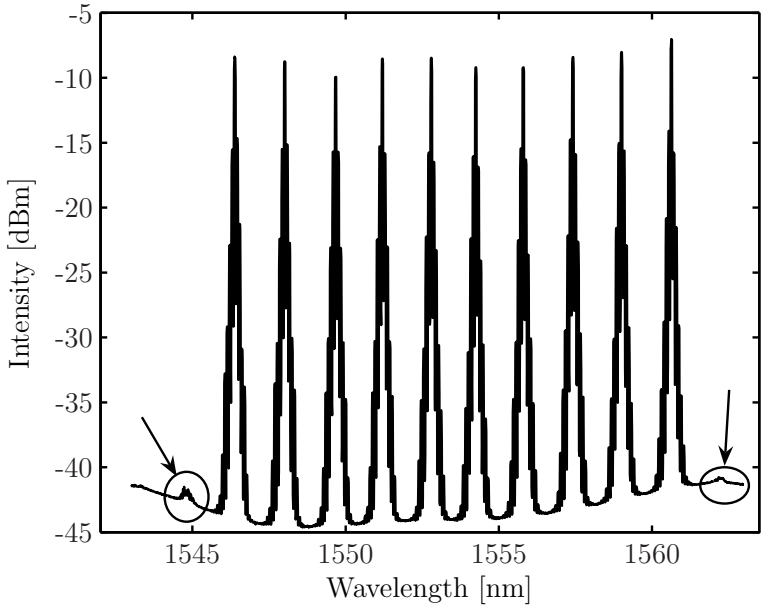

FIGURE 5.9: The spectrum of 10 synchronously EAM-modulated signals, after two round trips in the recirculating loop, shown in Figure 5.6. The circles indicate the emergence of signals generated through four wave mixing.

With this, I have first of all demonstrated the possibility of using linear spectrograms to characterise an array of synchronised WDM signals. The optical bandwidth over which these measurements can be made is dependent on the sampling modulator properties, especially the wavelength dependent insertion loss in the case that this is an electro-absorption modulator.

Secondly, I have successfully demonstrated the applicability of the characterisation method to characterise pulses in a recirculating loop setup. The 'gated measurement input' option of the *Advantest Q8384* optical spectrum analyser provides the capability to measure the spectrum of an optical signal, only for a specified time interval. I used this function to synchronise the measurement of the spectral slices in the spectrograms to the timing setup of the recirculating loop. Note that the time to acquire a full spectrogram after a recirculating loop is proportional to the total number of round trips in the loop. However, this does not impose a limit immediately in terms of timing stability, as the characterisation setup is self-referenced. More detrimental would be the effect of changing the dispersion properties of the loop during the acquisition time, for example due to a change in temperature. With measurement times of less than 10 minutes for the spectrograms shown here, we have not noticed such effects.

5.3 Novel modulation formats for high bit-rate transmission

Currently installed transmission links can efficiently be upgraded in terms of capacity by increasing the bit rate of the individual WDM channels. However, nonlinear effects such as intra-channel cross phase modulation and intra-channel four wave mixing can have significant detrimental effects on pulses at repetition rates of 40 $Gbit/s$ and beyond. With novel modulation formats, one tries to mitigate the effects of these nonlinearities. In this section, I will focus on some of these formats, and investigate the precise phase and intensity profiles of various pulses that are good candidates to overcome nonlinear distortion.

Because lithium niobate ($LiNbO_3$) modulators are well understood, and mathematically well behaved and versatile devices [9, 10], they have become indispensable optical tools in high speed optical transmission. In this section I will start by introducing phase modulators, and how they can be used to implement an interesting pulse modulation format, named alternating phase return to zero (APRZ). The pulses generated with this implementation are then characterised with the linear spectrogram technique.
A more compact way of generating APRZ pulses is then introduced. A single, dual-drive Mach-Zehnder modulator is used to generate various APRZ waveforms. We have used the linear spectrogram method again to characterise these pulses, and tested the performance of the technique after transmission of these 40 $Gbit/s$ pulses over an installed fibre network.
All the experimental data in this section has been acquired during two periods of joint experiments, where I took the pulse characterisation setup to the Optical Systems and Networks Laboratory at Acreo in Kista, Sweden. One of the main research topics at this well-equipped lab is to investigate how existing networks can be upgraded to higher capacities, by using novel modulation formats for example. The European Network of Excellence, e-Photon/ONe, has made this collaboration possible.

5.3.1 $LiNbO_3$ phase modulators

Due to its relatively low optical loss and high electro-optic effect, $LiNbO_3$ is an ideal material for implementing phase modulators. The refractive index of the

material changes when an electrical field is applied. This in turn changes the phase of the optical signal travelling through the lithium niobate. The electrical voltage needed to achieve a certain phase shift at a given electrical frequency can for example be characterised in the following way. The phase of a continuous wave optical signal is modulated sinusoidally:

$$e_{out} = A\cos(\omega t - \delta \sin \omega_m t), \tag{5.1}$$

where A is the amplitude of the optical carrier at frequency ω, and ω_m is the frequency of the phase modulation. δ is the modulation index. Using the following Bessel function identities:

$$\cos(\delta \sin \omega_m t) = J_0(\delta) + 2J_2(\delta)\cos 2\omega_m t + 2J_4(\delta)\cos 4\omega_m t + \ldots \tag{5.2}$$

$$\sin(\delta \sin \omega_m t) = 2J_1(\delta)\sin \omega_m t + 2J_3(\delta)\sin 3\omega_m t + \ldots \tag{5.3}$$

we can rewrite equation 5.1 as:

$$\begin{aligned} e_{out} = A[&J_0(\delta)\cos \omega t + \\ &J_1(\delta)\cos(\omega + \omega_m)t - J_1(\delta)\cos(\omega - \omega_m)t + \\ &J_2(\delta)\cos(\omega + 2\omega_m)t - J_2(\delta)\cos(\omega - 2\omega_m)t + \ldots] \end{aligned} \tag{5.4}$$

We can easily measure the ratio $J_1(V)/J_0(V)$ (the power ratio between the carrier spectral line and either one of the neighbouring spectral lines at a frequency offset of ω_m) as a function of the driving voltage. With this, we can determine the modulation index δ as a function of the driving voltage by fitting $J_1(\delta)/J_0(\delta)$ to the measured data. The electrical voltage needed to induce a π phase shift in current $LiNbO_3$ phase modulators is around 6 V.
In the next section, we use a phase modulator to implement a supplementary phase modulation onto return-to-zero pulses in a flexible way. After an introduction of the pulse format, I will use the linear spectrogram method to fully characterise this interesting format, and also to characterise the phase modulator in a direct way.

5.3.2 Alternating phase, return to zero

The alternating phase, return to zero format consists of RZ pulses for which the phase ideally alternates between two given values. The phase difference between

two consecutive RZ pulses, $\Delta\phi$, is a variable parameter of the format.

In a more general, and flexible way, APRZ pulses are in fact normal RZ pulses whose relative phase has been modulated with a phase modulator. Usually however, the pulses can only be phase modulated with a sinusoid at high repetition rates, because of the limiting bandwidth of electronics. This means that the pulses automatically become chirped, in an approximately linear way (assuming fairly short duty cycles): the sinusoid can be approximated locally as a parabolic curve, which leads to a linear chirp.

Figure 5.10 shows the experimental implementation we used to generate APRZ pulses initially, and Figure 5.11 summarises the possibilities of APRZ pulses generated with this setup.

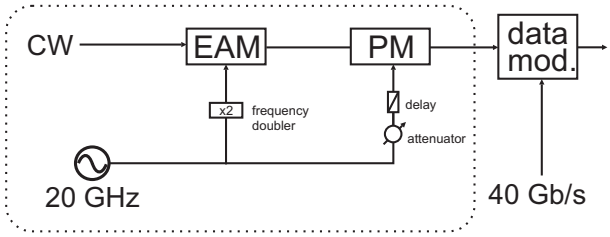

FIGURE 5.10: The APRZ transmitter including 40 $Gbit/s$ data modulation. 40 $Gbit/s$ pulses are carved from a CW laser signal with an EAM, and then phase modulated (PM) separately.

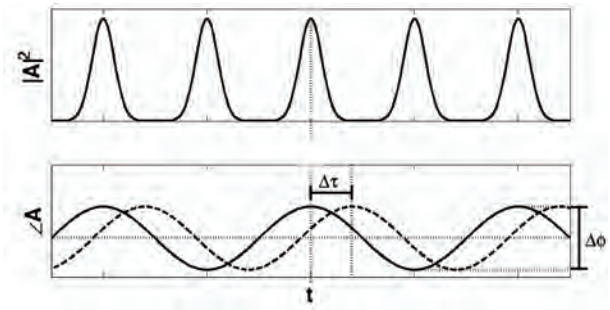

FIGURE 5.11: The APRZ modulation format using a separate phase modulator (as shown in Figure 5.10): intensity profile (top), and phase profile (bottom).

Another parameter that can be adjusted in this case is the time delay $\Delta\tau$ between the phase modulator and the maximum intensities of the pulses.

Our partners in the e-Photon/ONe project at Acreo have been thoroughly investigating the benefits of the alternating phase, return to zero format, and it has been very interesting to apply the linear spectrogram technique to this modulation format. Their research has revealed that the format possesses particular properties that make it robust against nonlinearities – in particular intrachannel four wave mixing – and dispersion [11, 12]. They have shown that it is the exact amplitude

of the phase modulation that makes all the difference. However, until now, there has been no direct way of assessing this phase difference, making an accurate interpretation of experimental results quite difficult.
I have shown one possible way of characterising a phase modulator, by calculating the phase modulation from a series of spectral measurements in a previous section, however it is a cumbersome method, and not really practical as this has to be done in a stand-alone experiment. Also, this method is not applicable anymore when the pulses are generated with a MZM (see Section 5.3.4), which automatically induces the phase modulation.

5.3.3 Experiments and results

5.3.3.1 Experimental setup

I started by adapting the linear spectrogram technique to suit this advanced modulation format. The actual physical period of APRZ pulses spans over two consecutive pulses. In the case of optical pulses with a repetition rate of 40 GHz, this corresponds to 2×25 ps. Consequently, we have to scan over 50 ps to get a full spectrogram. In order to keep the spectrogram simple enough to allow for a straightforward deconvolution, the gating function should be a single pulse with a repetition rate of 20 GHz. Double pulses are notoriously difficult to correctly deconvolve from an SHG-FROG spectrogram, and similar difficulties would affect a deconvolution of a cross-correlation spectrogram between two double pulse sequences. Moreover, the option of using an electrical clock recovery unit which generated a sinusoidal 20 GHz electrical signal from a 40 $Gbit/s$ data modulated sequence proved to be very convenient in the characterisation setup, which is shown in Figure 5.12.

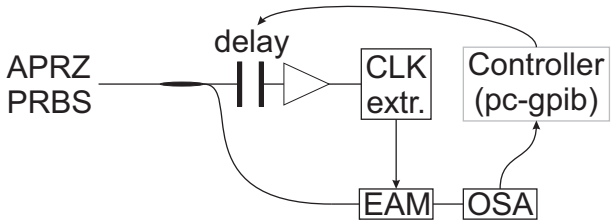

FIGURE 5.12: Self referenced linear spectrogram acquisition setup, suitable for 40 $Gbit/s$ APRZ pulses. The clock recovery unit (CLK) generates a 20 GHz sinusoidal signal synchronised to a data modulated 40 $Gbit/s$ pulse stream.

At the same time though, this means that we *have* to modulate the pulses with 40 $Gbit/s$ data, as otherwise, the clock recovery unit cannot synchronise its electrical output with the input signal. By doing this, we were able to show that the spectrogram technique still works very well even when the pulses were data modulated with a pseudo random bit sequence (PRBS). Because the method is multi-shot and involves spectrally resolving the gated optical signal, only the average waveform of the pulses can be characterised. This means indeed that pattern dependent aberrations will not show up in the retrieved information. The spectrogram technique thus also acquires the long-time averaged optical signal, in the same way as an optical spectrum analyser measurement, but gives the added information of the average phase of the pulses. This means that we can translate the information immediately to the time domain, and deduce interesting temporal information for the pulses.

5.3.3.2 Results

Using the transmitter and characterisation setups shown in Figures 5.10 and 5.12 respectively, we started by measuring the EAM carved pulses first without any phase modulation, and later for a series of different phase modulation amplitudes. The measured and reconstructed spectrograms are shown in Figure 5.13 for $\Delta\tau = 0ps$ and an electrical driving voltage of 5.4 V_{pp} on the phase modulator. Both the chirp of the gating function and the chirp of the measured pulses contribute to the shape of the intensity features in the spectrogram. The intrinsic chirp of the gating EAM will then either enhance or serve to reduce the chirp on the pulses, because of their respective opposite chirp slopes.

The intensity and phase retrieved from these spectrograms are shown as the crosses in Figure 5.14. For comparison, the independently measured intensity trace (for which we briefly switched the data modulation off) measured with a commercial optical sampling oscilloscope is overlapped with the retrieved intensity information. The agreement is excellent. It has been the first time that we were able to compare the results *temporally* with an independent measurement – electrical sampling oscilloscope traces do not suffice: they do not provide enough bandwidth. To find such good agreement by merely normalising both traces and overlapping them, is very pleasing. Also spectrally, there is very good agreement with the

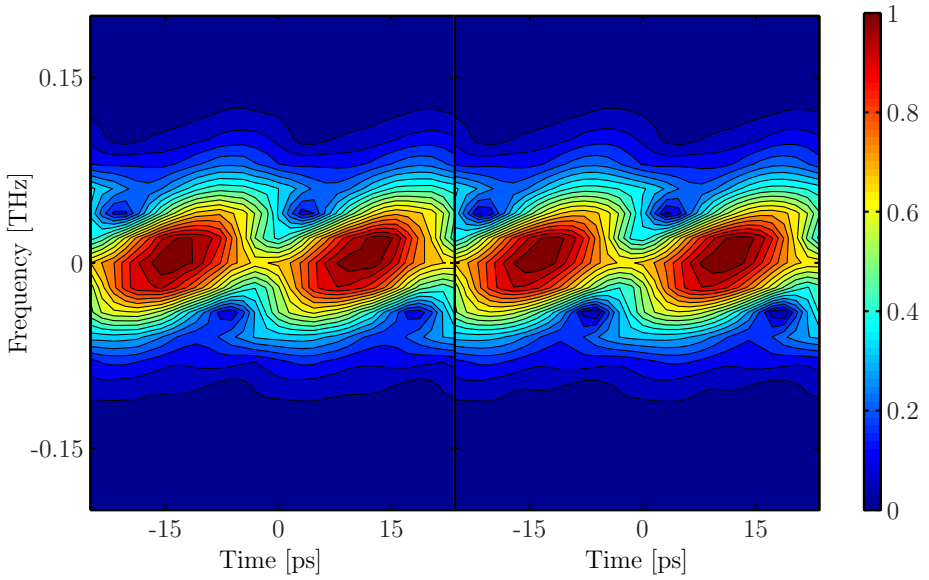

FIGURE 5.13: Measured and reconstructed spectrograms for EAM-carved pulses without APRZ phase modulation.

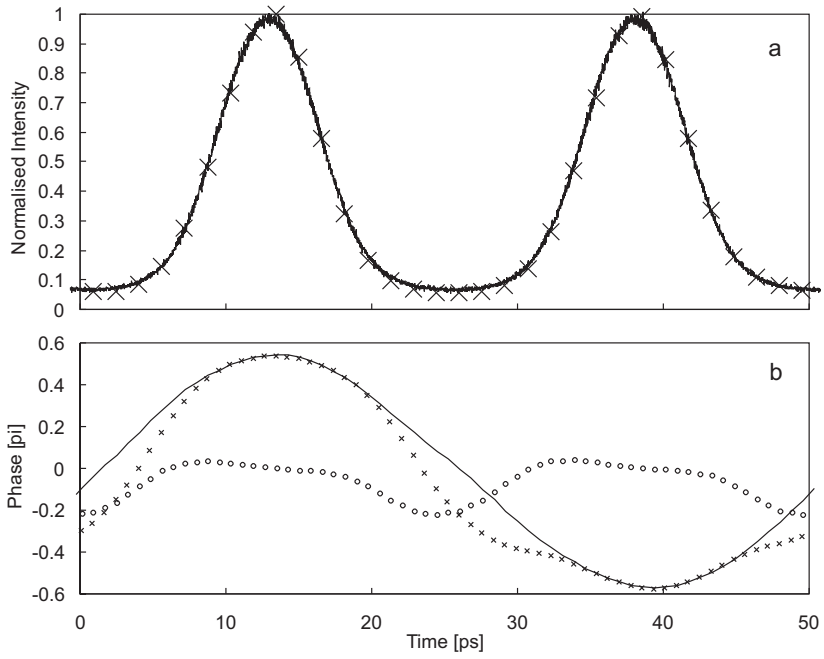

FIGURE 5.14: EAM-carved pulses, intensity and phase profiles. The phase plot also shows the phase of APRZ modulated pulses, and the phase modulator function, obtained by subtracting the phase of unmodulated pulses from modulated pulses.

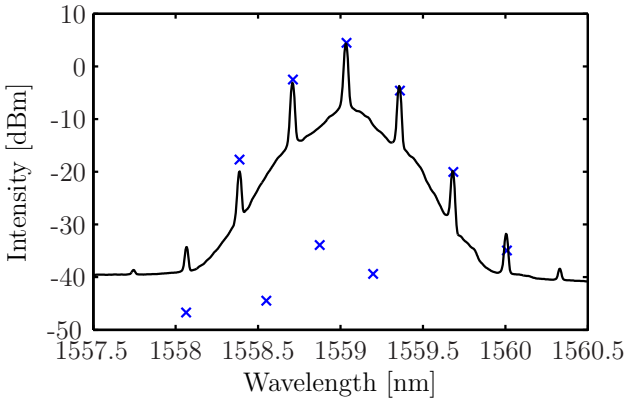

FIGURE 5.15: Independently measured spectrum (full line) of data-modulated EAM-carved pulses (without APRZ modulation), compared with the spectrum retrieved from the spectrogram (×) (shown in Figure 5.13). The retrieved data clearly show a signal with a 40 GHz repetition rate, hence the low level of the data points at $(2n+1) \times 20GHz$ from the carrier.

spectrum measured on a spectrum analyser, as shown in Figure 5.15 for EAM-carved pulses without alternating phase modulation, a consistency check which has already been shown in earlier chapters.

We can clearly see a distinct temporal phase profile which is not exactly sinusoidal. This is due to the chirp on the EAM-carved pulses because of the change in the refractive index when the absorption spectrum changes (see Section 3.3). The phase profile of these non-phase modulated pulses is shown as the circles in the same figure. It is only a simple calculation to subtract the phase profile of the original pulses from the phase profile of the APRZ pulses. The result is the near perfect sinusoidal line in the figure. With this, we have in fact directly characterised the phase modulating properties of the $LiNbO_3$ phase modulator.

Even though the collaboration time span was limited to a very short 9 days, we were able to acquire a whole series of interesting spectrograms. This made it possible to combine the information gained from these measurements into a summarising plot for the phase modulator, which is shown in Figure 5.16. With this, we determined the exact phase modulation amplitude as a function of the driving voltage, which is as expected linear.

Phase modulation offset When $\Delta\tau$ (as in Figure 5.11) is close to half the bit slot duration, so that the intensity peak of each pulse experiences a linear phase change, the pulses are alternately shifted in frequency: positively where $d\phi/dt > 0$ and negatively where $d\phi/dt < 0$. This can already be clearly observed in the

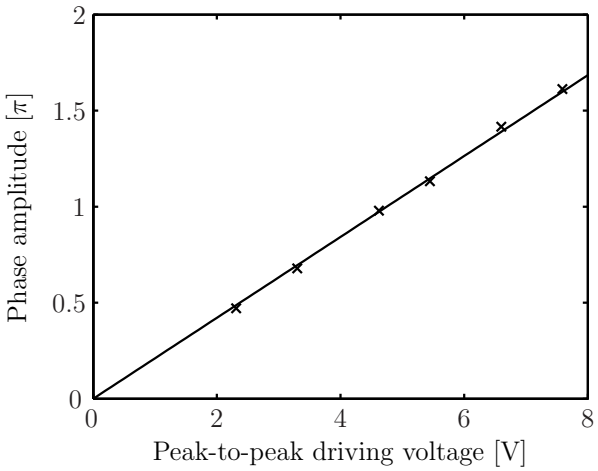

FIGURE 5.16: The phase amplitude as a function of the electrical peak-to-peak driving voltage.

spectrogram, as shown for $\Delta\tau = 15ps$ in Figure 5.17. The intensity features show a different central wavelength for two neighbouring pulses. The retrieved intensity and phase information is shown in Figure 5.18.

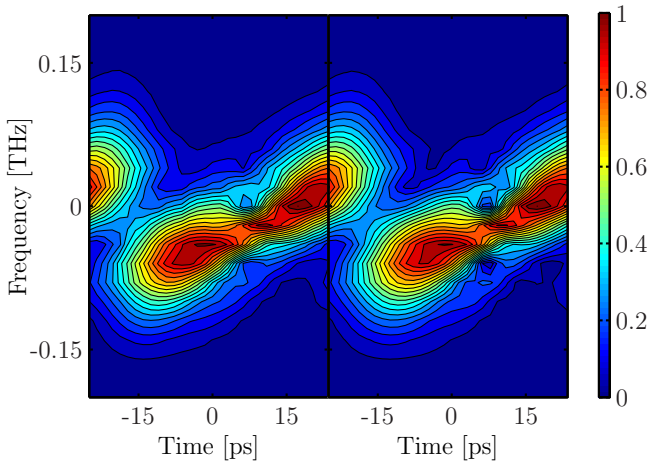

FIGURE 5.17: Measured (left) and reconstructed (right) spectrograms of phase modulated EAM-carved pulses where $\Delta\tau = 15ps$ (see Figure 5.11).

5.3.3.3 Short pulses

We then further extended our data set, and acquired spectrograms of ultrashort pulses generated with a harmonically, actively mode locked ring laser (Calmar-Optcom PSL-40), both with and without APRZ modulation. This 40 *GHz* short pulse source is tunable in wavelength; we chose to work at 1560 *nm*, because that is where the sampling EAM is working optimally (lowest insertion loss and good

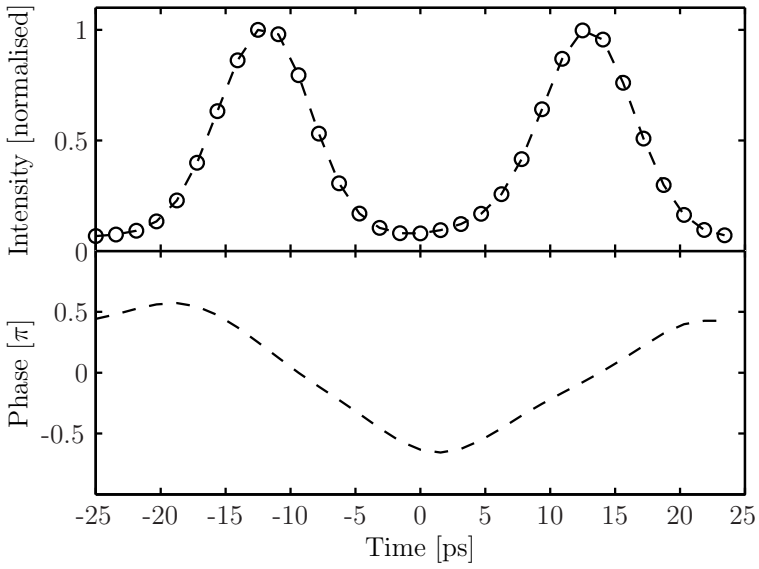

FIGURE 5.18: Intensity and phase retrieved from the spectrogram shown in Figure 5.17. The pulses have alternating linear phase slopes, corresponding to separated central wavelengths.

extinction ratio). This source also has three different working regimes which deliver slightly different pulse durations: 1.3, 2.2 and 3 *ps*.

In order to accommodate the increased bandwidth of these pulses, the spectrograms are now interpolated onto 128×128 point grids. This immediately corresponds to an increased temporal resolution, which is necessary to correctly retrieve the waveform information: less temporal resolution would mean that the Nyquist limit is no longer satisfied.

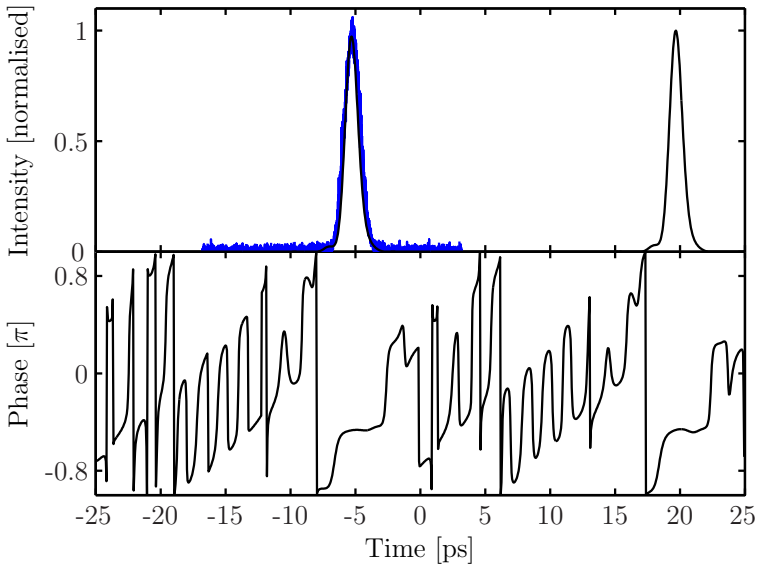

FIGURE 5.19: Retrieved intensity and phase information for 1.3 *ps* Calmar-PSL40 ring laser pulses without external phase modulation. The optical sampling oscilloscope trace is the blue line.

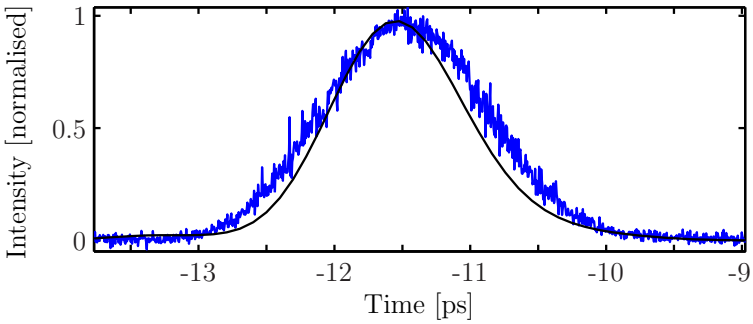

FIGURE 5.20: Detail of the intensity profile of the 1.3 *ps* pulses shown in Figure 5.19.

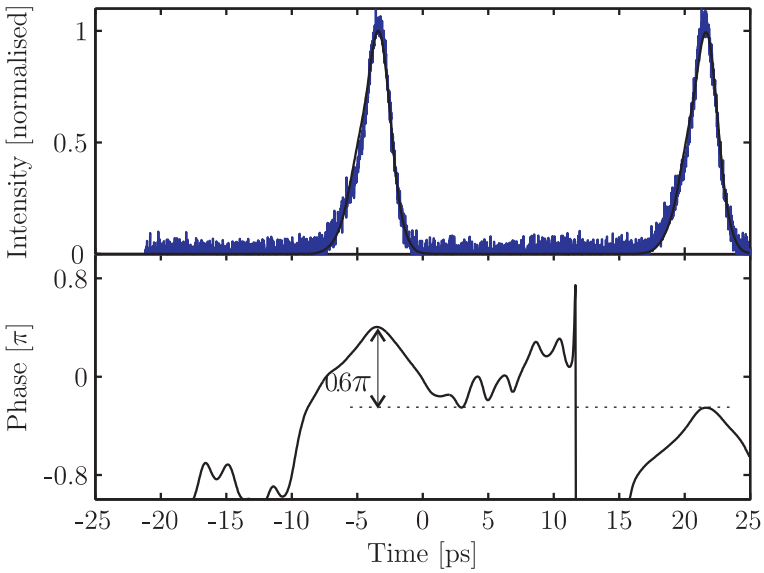

FIGURE 5.21: Retrieved intensity and phase information for 2 *ps* Calmar-PSL40 ring laser pulses, with 0.6π APRZ modulation. The optical sampling oscilloscope trace is the blue line.

The retrieved intensity and phase for the 1.3 *ps* pulses (without phase modulation), measured over a span of 50 *ps* is shown in Figure 5.19. There is very good agreement again with the optical sampling oscilloscope trace. However, looking more closely at the intensity retrieved from the spectrogram, compared to the intensity measured with an optical sampling oscilloscope, in Figure 5.20, we see that there is a discrepancy: the optical sampling oscilloscope, with a resolution of about 1 *ps*, is unable to accurately resolve an optical pulse of the order of 1 *ps*, contrary to the spectrographic technique.

The phase of the waveform is undefined where there is no pulse intensity, and varies randomly between π and $-\pi$. This makes it impossible to derive the same sinusoidal phase modulator profile from the retrieved pulse information in these cases. Figures 5.21 and 5.22 show the retrieved temporal information for the ring

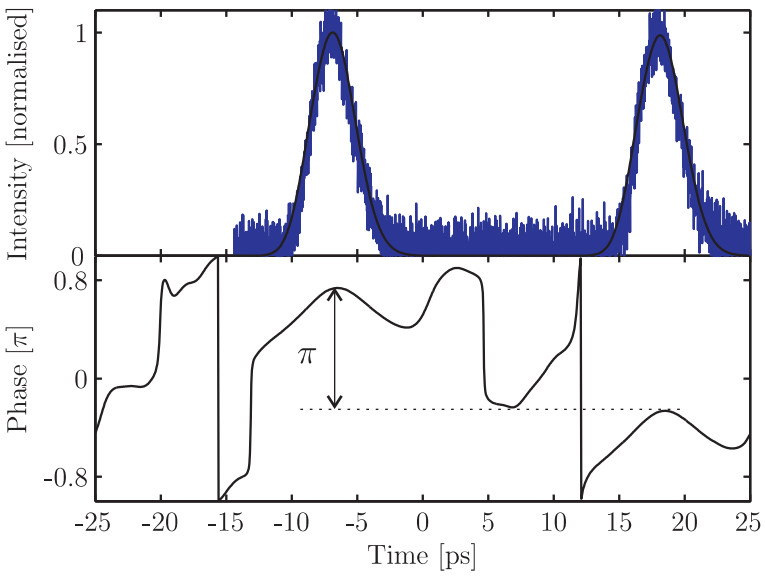

FIGURE 5.22: Retrieved intensity and phase information for 3 *ps* Calmar-PSL40 ring laser pulses, with π APRZ modulation. The optical sampling oscilloscope trace is the blue line.

laser running at settings to create 2.2 *ps* and 3 *ps* pulses respectively, this time with alternating phase modulation (0.6π and π respectively).

Optical filtering Wei *et al.* showed with the same spectrogram technique that nearly chirp free, alternating phase pulses can be obtained through spectral filtering of the sinusoidally phase modulated pulses with an optical filter [13]. Just before these results were presented at the Optical Fiber Conference in Anaheim, 2005, we were performing very similar measurements.
For real transmission systems at data rates of 40 $Gbit/s$, the ultrashort pulses shown in Figures 5.19–5.22 take up too much bandwidth. Consequently, we filtered the 2.2 *ps* pulses (similar to those shown in Figure 5.21, but with a larger $\Delta\phi$) using an arrayed waveguide grating with a channel bandwidth of 75 GHz. The results are shown in Figure 5.23.

The APRZ pulses have now got very steep phase shifts between them, corresponding to the findings of Wei *et al.* The pulses are slightly chirped still, but in the same way for every pulse. This is due to SPM affecting these ultrashort pulses in the short amount of fibre between the amplification and the optical filtering. The alternating chirp induced by the phase modulator has been taken away by the filtering.

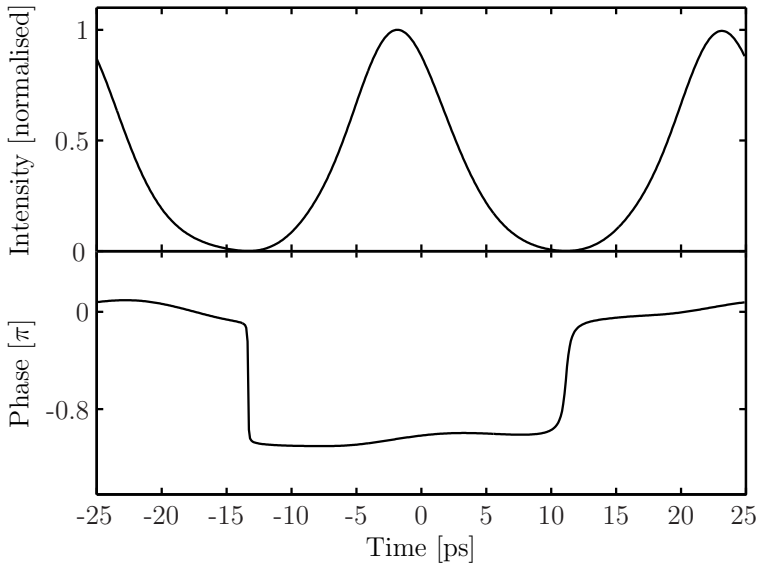

FIGURE 5.23: The phase of slowly phase modulated short pulses becomes abrupt when filtered optically. Here, 2.2 *ps* ring, phase modulated ring laser pulses are filtered with a 75 *GHz* wide arrayed waveguide grating.

5.3.4 $LiNbO_3$ Mach Zehnder Modulator Carved Pulses

Because the first period of joint experiments had got us a wealth of interesting data, we decided to follow up on these experiments, and further extend the data set. During my second visit to the Optical Systems and Networks lab at Acreo, we used the transmitter implementation shown in Figure 5.26. This removes the need to do separate pulse generation or carving, and produces narrower bandwidth pulses.

In principle, the two arms in the MZM work in the same way as the phase modulator in the section above. On recombination of the outputs of the two arms, the optical signals interfere constructively or destructively, depending on their relative phase difference. A simplified schematic of a dual-drive MZM is shown in Figure 5.24.

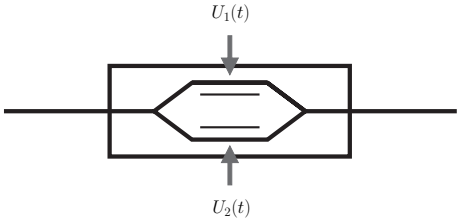

FIGURE 5.24: Schematic diagram of a Mach-Zehnder modulator.

Recently, the dual-drive modulators have been gaining a lot of attention because of the fact that they can generate both chirped and chirp free pulses [14]. Assuming

the input optical field to the modulator is a CW signal E_0, the optical field at the output of the modulator is given by:

$$E(t) = \frac{E_0}{2}\left\{\exp\left[i\pi\frac{U_1(t)}{V_\pi}\right] + \exp\left[i\pi\frac{U_2(t)}{V_\pi}\right]\right\} \tag{5.5a}$$

$$= E_0 \exp\left[i\pi\frac{U_1(t)+U_2(t)}{2V_\pi}\right]\cos\left[\pi\frac{U_1(t)-U_2(t)}{2V_\pi}+\phi\right], \tag{5.5b}$$

in case of perfect extinction (corresponding with perfect splitting and combining of the optical signals in the interferometer). ϕ is the relative optical phase between the contributions of both arms in absence of RF driving signal ($U_1(t) = U_2(t) = 0$). Equation 5.5b tells us that the phase modulation induced by a dual-drive MZM is determined by the sum $U_1(t)+U_2(t)$ of the two driving signals, whilst the intensity modulation is dependent on the difference $U_1(t)-U_2(t)$ of the driving signals. For example, by choosing the driving signals so that $U_1(t) = -U_2(t)$, chirp free pulses will be created. Single-drive modulators usually build on this principle by placing the active electrode in between the two arms, so that both arms are automatically modulated anti-symmetrically [15].

With a maximum voltage difference between the two sinusoidal driving signals equalling $2V_\pi$, it is possible to create pulses with a repetition rate of twice the frequency of the driving signals. In this case, one can choose between either 33% or 67% duty cycle pulses. These operation regimes of the modulator can be understood intuitively by studying the transfer characteristic, shown in Figure 5.25. The V_{pp} driving voltage and bias are marked by line segments and their respective centre markers for three different modulation regimes: 50% RZ, 33% RZ and 67% carrier suppressed return to zero (CSRZ). Note that for the latter two, *two* pulses are generated in every period of the driving signal.

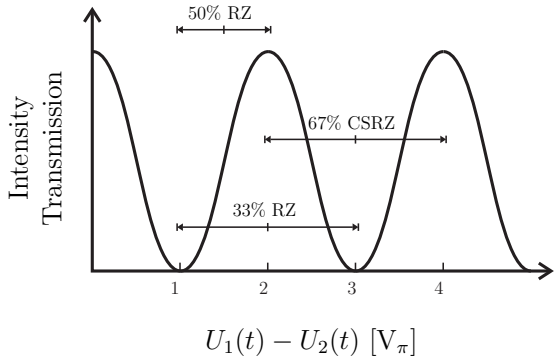

FIGURE 5.25: Intensity transfer characteristic of a MZM.

The MZM is thus particularly interesting because of the fact that it provides possibilities to create waveforms with interesting phase and intensity properties, and also because it can generate higher (2×) repetition rate pulses than the driving electronics would otherwise permit.

In the rest of this section, we use the pulse generation setup shown in Figure 5.26 to generate a range of different APRZ pulses, including CSRZ: carrier suppressed return to zero, where the phase modulation amplitude $\Delta\phi$ is π.

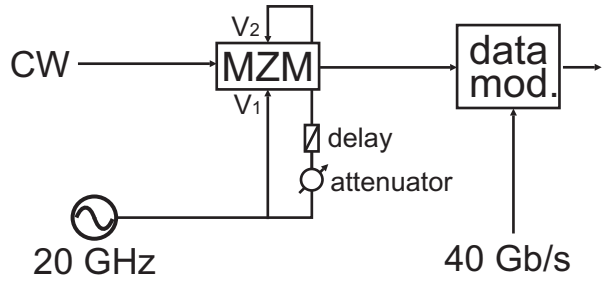

FIGURE 5.26: Dual-drive MZM configuration for alternating phase return to zero pulse generation.

5.3.4.1 Without data modulation

I was given the opportunity to measure some pulses that were not data modulated, whilst the setup for the data transmission experiment described in Section 5.3.4.3 was still being built. This meant that the characterisation setup needed to be changed again, as the clock recovery unit does not work without data modulation on the pulses. Consequently, I did not use the motorised and programmed optical delay stage, but an RF delay, which was manually tuned for every step of the delay.

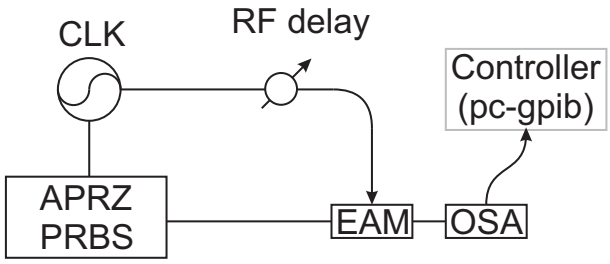

FIGURE 5.27: Manual spectrogram acquisition setup using an RF phase shifter instead of an optical delay line.

Even though it is impossible to reach the same temporal accuracy as with the motorised delay stage, the spectrograms acquired in this rather slow manner still

turned out to be very useful. The adapted setup is shown in Figure 5.27. Note that it is only possible to use this implementation directly after the pulse generation, when the pulses are still nicely synchronised to the RF synthesiser. The retrieved pulse information for 0.6π APRZ pulses (i.e. there is a phase difference of 0.6π between the centres of two consecutive pulses) is shown in Figure 5.28. It comes as no surprise that the agreement with independently measured intensity traces is again very good in this case. The spectrograms shown further in this section are again taken with the setup shown in Figure 5.12, and with PRBS data modulated pulses.

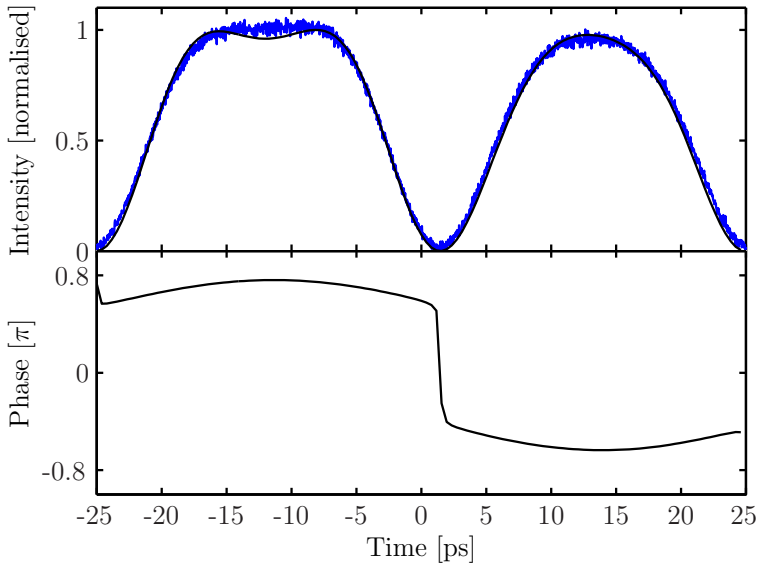

FIGURE 5.28: Intensity and phase of APRZ modulated pulses without data modulation pulses, acquired with the manual setup shown in Figure 5.27.

5.3.4.2 Gating function width

Initially this time, I scanned a few spectrograms of CSRZ pulses, and adjusted the bias voltage on the sampling EAM. The duration of the sampling window becomes longer when the bias voltage is set to lower values. Figure 5.30 shows the duration of the sampling window (FWHM) as a function of the bias voltage, and Figure 5.31 shows how the gating window evolves depending on the bias.
For all these settings, there were no problems to reconstruct the spectrograms. However, the best bias setting was found to be around $-3.4\ V$, because of the better extinction ratio obtained. This results in a better contrast in the spectrogram, which in turn means a faster convergence to the correct solution in the pulse

retrieval as there is less room for ambiguities. The retrieved intensity and phase profiles for this series of spectrograms are shown in Figure 5.29.

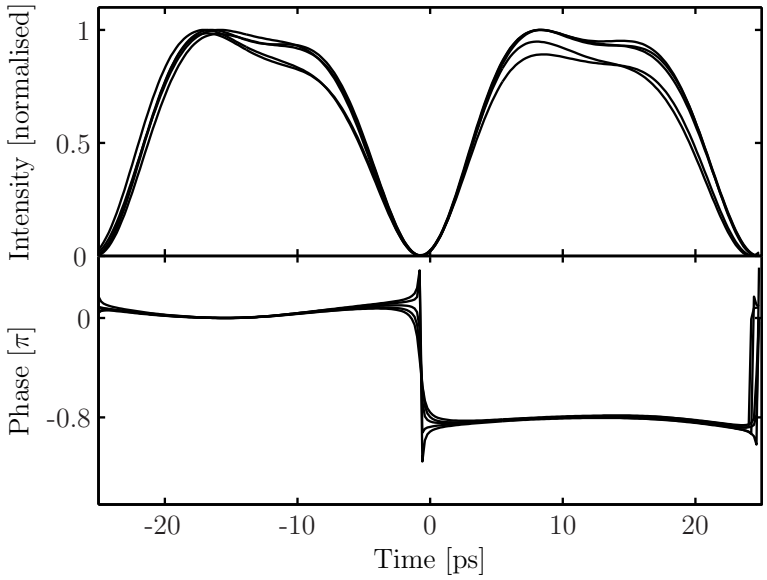

FIGURE 5.29: Intensity and phase profiles retrieved from spectrograms with bias voltages of 2.5, 3, 3.4, 4 and 4.5 V, and a 5.4 V_{pp} RF driving signal.

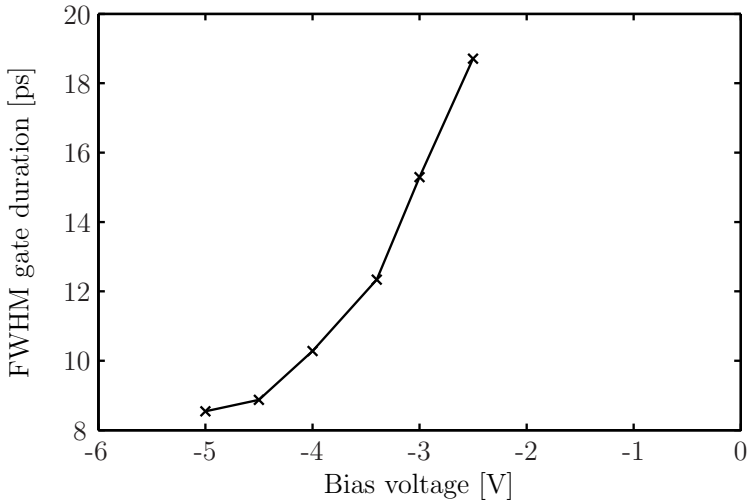

FIGURE 5.30: EAM gate duration as a function of the reverse bias voltage. The RF electrical signal is a 5.4 V_{pp} sinusoid.

The phase profiles are almost exactly the same for the four different settings, however, the retrieved intensities are slightly different. In a similar way as the boot strap method [16] gives an idea about the error margin of FROG retrievals, the curves shown here also give a good idea about the error margin, due to noise on the spectrogram. This is in fact still an overestimation of the error on the retrieved pulse information, as in this case, the gating function is changed slightly every

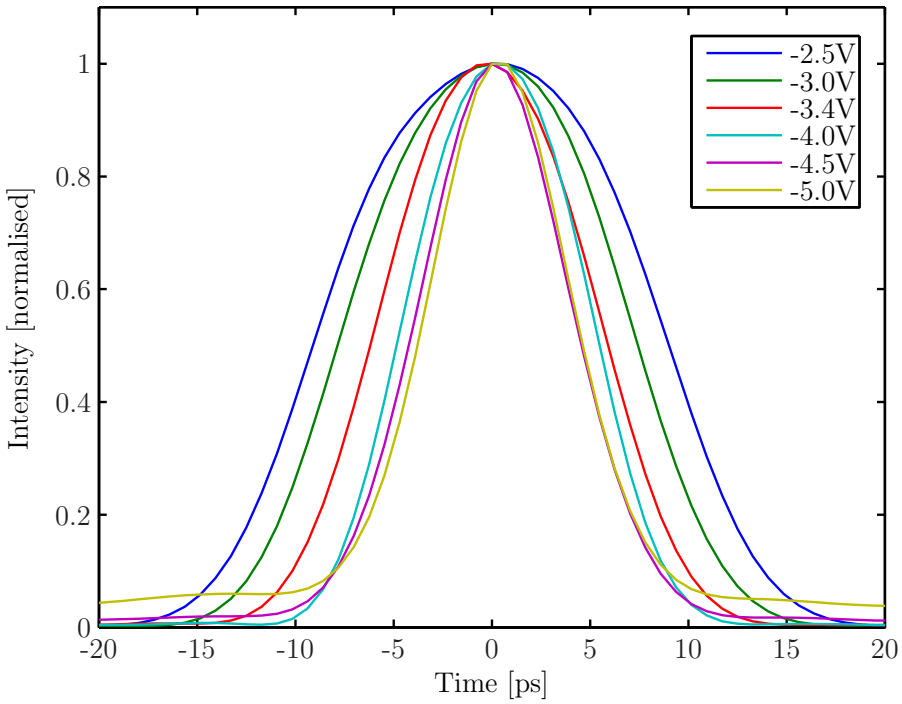

FIGURE 5.31: Retrieved EAM gate profiles for different bias settings.

time, which affects the spectrogram.

5.3.4.3 Transmission over a short fibre link

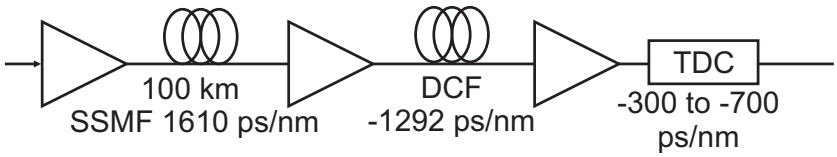

FIGURE 5.32: Short fibre link including a dispersion compensating fibre and a tunable fibre Bragg grating dispersion compensator.

To investigate the potential of this pulse characterisation method to be used more generally as a new way of pulse monitoring, we first transmitted the pulses over a short fibre link in the laboratory. The schematic of the fibre link is shown in Figure 5.32. The dispersion of the 100 km of standard single mode fibre (1700 ps/nm) is compensated by both a length of dispersion compensating fibre (-1200 ps/nm) and a tunable dispersion compensating fibre Bragg grating (Teraxion, tunable from -300 to -700 ps/nm).

The retrieved pulse information before and after transmission, with different settings of the TDC, is shown in Figure 5.33. There is a clear evolution from undercompensation (-310 ps/nm): the phase is curved upwards, corresponding to downchirp; to almost perfect compensation (-315 ps/nm): the phase is virtually exactly the same as the phase of the input pulses; and finally overcompensation (-328 ps/nm), where the phase for the individual pulses is curved downwards, corresponding to upchirp.

According to Forzati *et al.*, there is a negative power penalty in CSRZ systems when there is either a residual dispersion, or overcompensation of the signal of about ± 15 ps/nm [17]. This effect is clear when one considers the shape of the intensity profile of the pulses. Perfectly compensated pulses have a flat top, they look more rectangular. When the pulses acquire about 15 ps/nm dispersion, they develop into shorter pulses. With the same average power in the signal, the pulses now have a higher peak intensity, allowing for an easier discrimination between ones and zeroes at the receiver side of the system.
On the other side, the CSRZ format is not as robust against intrachannel four wave mixing effects, compared to the $\pi/2$ APRZ format. With a such a versatile pulse source as the one shown in Figure 5.26, which can be adjusted easily to generate pulses with an arbitrary phase shift, it is a great advantage to know what the exact phase difference is. A real-time implementation of the pulse characterisation technique would make it possible to dynamically fine tune the settings of the tunable dispersion compensator and the parameters of the transmitter. A feedback system could then automatically minimise the error rate without actually having to perform expensive bit error rate measurements.

Transmission over 540 *km* of installed fibre Even though the performance of the linear spectrogram method to monitor optical signals after a short link already indicates its potential, the real test is to check whether it still performs well after transmission in an actual system. The Swedish National Testbed, managed by Acreo, gave us the possibility to undertake these tests. The schematic of the installed fibre link over which we transmitted and then characterised the pulses is shown in Figure 5.34. It is a double pair of optical standard single mode fibre, in places amplified and compensated with dispersion compensating fibre. The available link is in fact even longer than shown here, however, we decided to loop back in Gävle because it was still convenient to go and change the connections, whilst

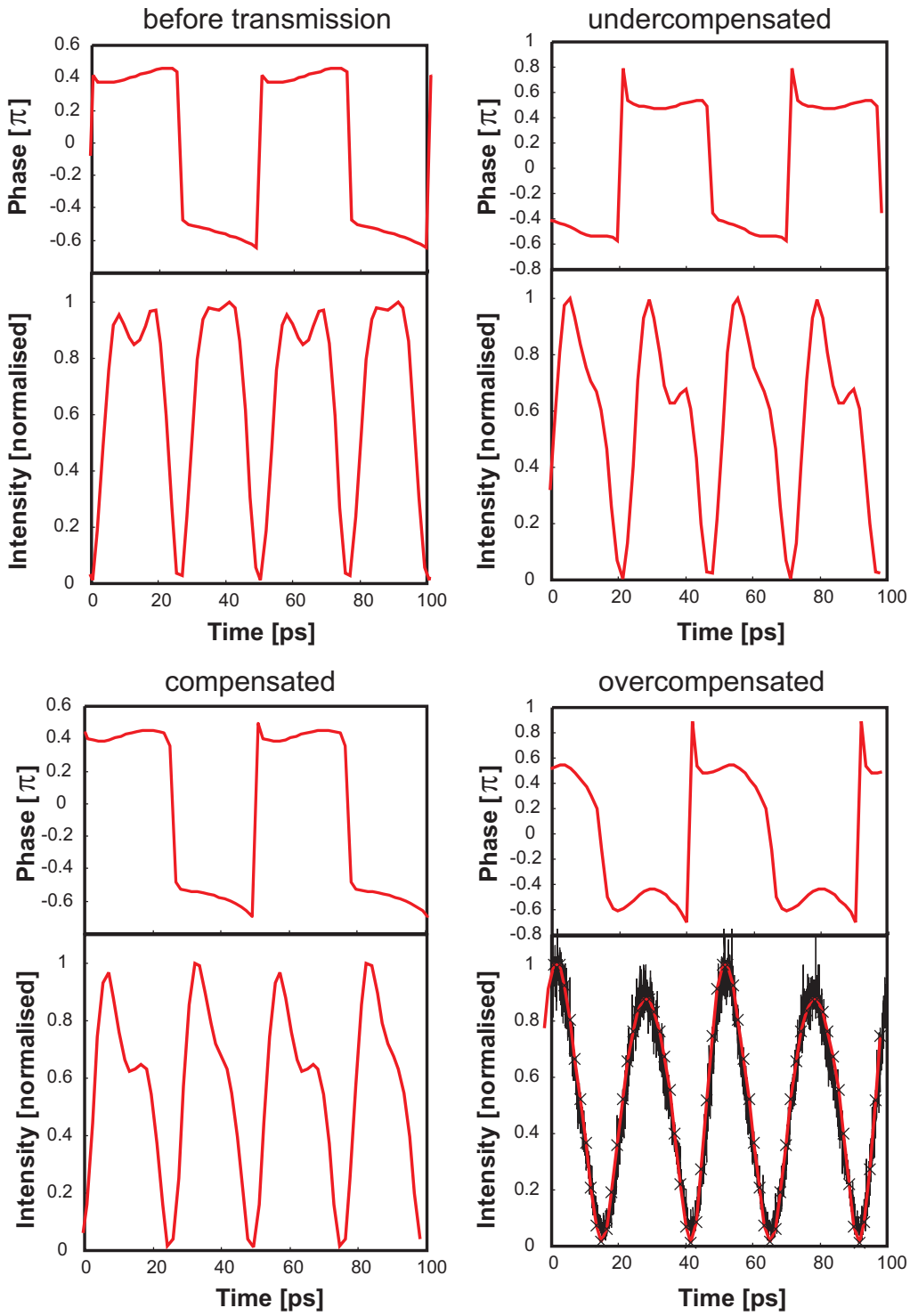

FIGURE 5.33: Different settings of the tunable dispersion compensator are monitored.

ensuring that the total of 540 km of SSMF would give a sufficient test for a 40 $Gbit/s$ system.

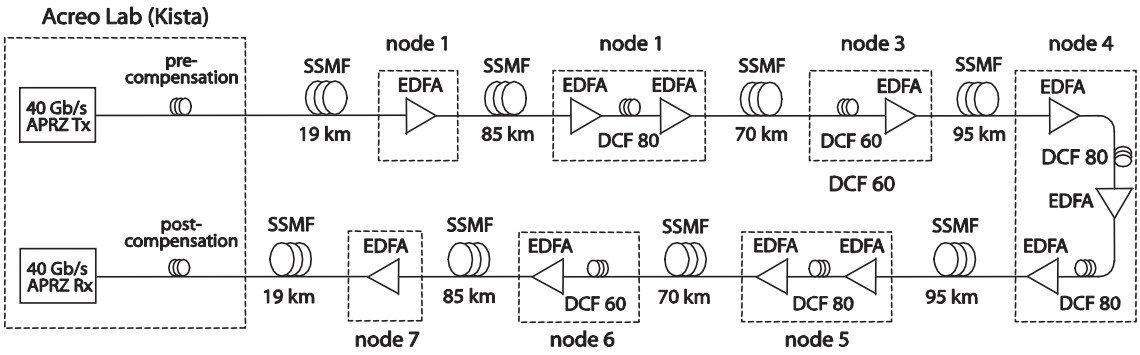

FIGURE 5.34: The installed fibre link, comprising 540 km of standard single mode fibre, compensated in places by dispersion compensating fibre and a post-compensating tunable dispersion compensator.

The eye diagram measured with the optical sampling oscilloscope was severely closed after the transmission of the pulses over this link, and we failed to reach error-free operation: the bit error rate after transmission was about 10^{-6} for the CSRZ pulses and 10^{-4} for the APRZ pulses. Also, the spectrograms acquired were much noisier. Still, after minimal mathematical processing, the spectrograms were accurately reconstructed (spectrogram error of 0.01 or less). The retrieved intensity and phase profiles are shown in Figure 5.35 for CSRZ pulses, and in Figure 5.36 for $\pi/2$ APRZ. In each case we tried different settings on the dispersion compensator, which is again reflected in the phase profiles.

There is still reasonable agreement between the average pulse intensity retrieved from the spectrogram and the eye diagrams, although we cannot 'normalise' the eye diagram, so a best fitting scaling is used here. In the case of the APRZ pulses (Figure 5.36), we were performing the measurements rather far away from the zero residual dispersion point (achieved with a tunable dispersion setting of around -450 ps/nm), because we were able to obtain a slightly better bit error rate performance there. Mathematical simulations have shown that the phase of APRZ pulses indeed returns to an upward curve (deceivingly indicating undercompensated dispersion) when they are in fact strongly overcompensated.

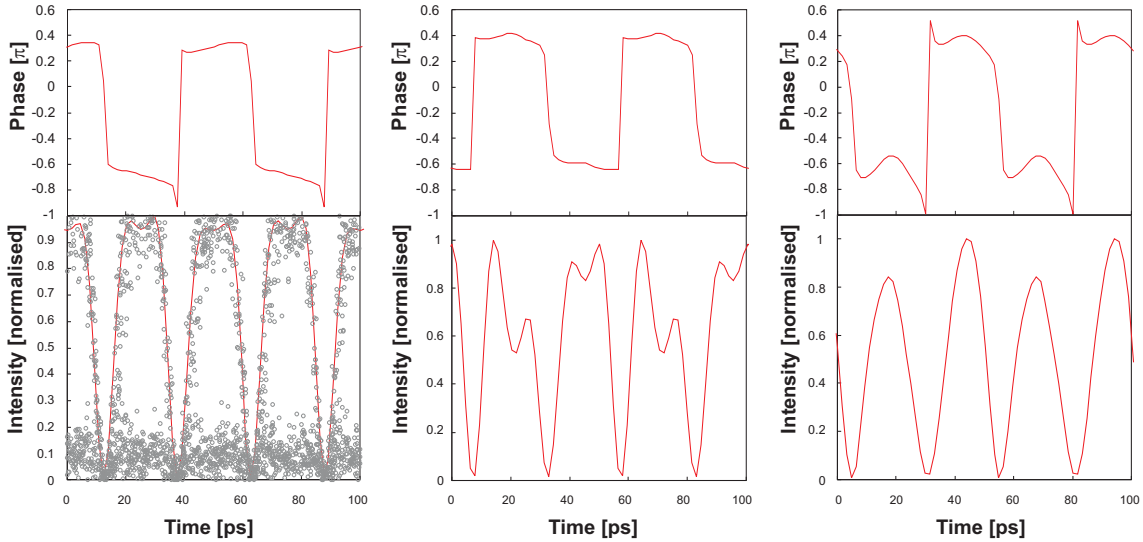

FIGURE 5.35: Measured phase and intensity profiles of CSRZ pulses before (left) and after transmission over the installed fibre link with different TDC parameters: -455 ps/nm (middle) and -465 ps/nm (right). The small circles are the eye diagram measured with an optical sampling oscilloscope.

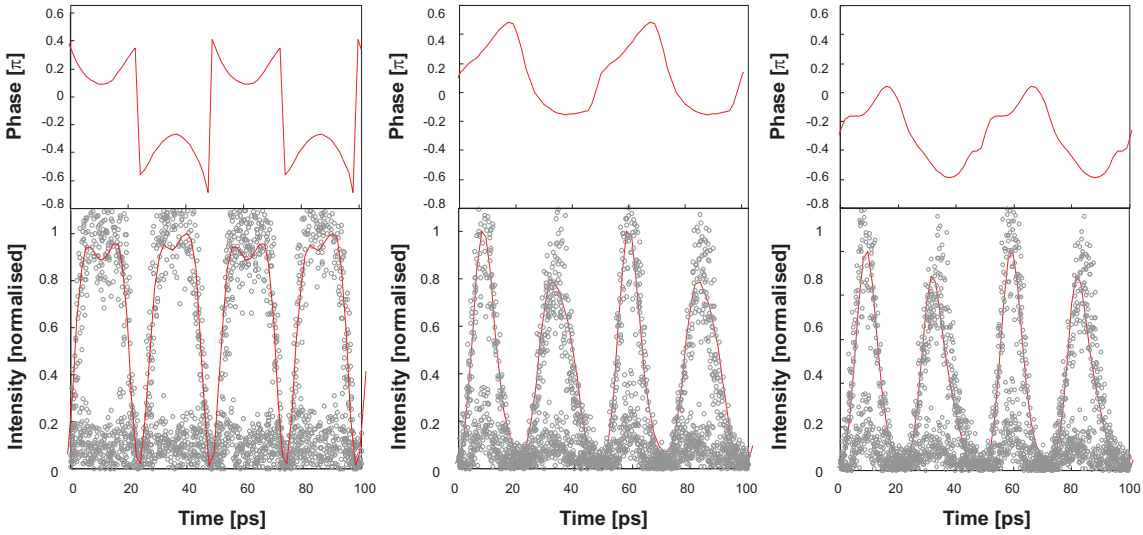

FIGURE 5.36: Measured phase and intensity profiles of $\pi/3$ APRZ pulses before (left) and after transmission over the installed fibre link with different TDC parameters: -495 ps/nm (middle) and -505 ps/nm (right). The small circles are the eye diagrams measured with an optical sampling oscilloscope.

5.4 Conclusions

In this chapter, I have demonstrated that the linear spectrograms can immediately be applied to high capacity systems. First of all, a wavelength division multiplexing setup was created to generate an array of channels with synchronised pulses. Measuring the spectrogram before and after propagation over a short length of optical fibre produced results that agree very well with numerical simulations. The relative timing information between the pulses in the various channels gained by these measurements is relevant for example to the regeneration schemes developed for synchronous WDM systems.
When the total range of the measured spectrogram is further increased however, problems related to the bandwidth of the gating modulator start to emerge. It turns out that when the spectrogram is deconvolved as a whole, the retrieved pulse information is incorrect, because the gating function of the modulator is assumed constant for all wavelengths, which is not the case. It is necessary to split up the spectrogram into its individual channels. This will at the same time reduce the computational time needed to reconstruct the fields of the individual pulses.
By propagating the WDM signal over a recirculating loop, two more interesting effects were noted. The residual third order dispersion was clearly observed as the temporal walk-off between the channels after one and two circulations in the loop. This was confirmed by the independently measured total dispersion of the fibre span. Also, four wave mixing affected the pulse shape during the propagation in the recirculating loop, observed as a slight modulation on the pulses, and the creation of low level ghost pulses. This was evidenced by the spectrum after propagation, where there are clear signs of signal components created at new wavelengths.
It is anticipated that with adequate development of modulator technology, it should be possible to use this scheme as a pulse monitoring tool that can scan the whole C-band for example, at a very low cost.

In the second part of this chapter, extensive measurements on a system with a bit rate of 40 $Gbit/s$ show the merits of this cost effective pulse measurement setup. The new APRZ pulse modulation format, which has promising robustness against nonlinear and dispersive effects in the fibre, was accurately characterised. The intensity profiles agree extremely well with state-of-the-art optical sampling oscilloscope measurements, and the phase modulation function, calculated from the retrieved pulse information shows the expected sinusoidal shape. It is shown

that even with PRBS data modulation on the pulses, the technique performs well. Also very short pulses are accurately characterised. The resolution even surpasses the resolution of the optical sampling oscilloscope that we used, as becomes noticeable for the shortest fibre ring laser pulses.
Finally, the measurements performed on the dual-drive modulator, implementing the APRZ format in a compact yet flexible manner, were again very satisfying. The evolution of the phase profile of the pulses shows a clear development depending on the exact settings of the tunable dispersion compensator. We demonstrated this after a short link in the lab, as well as after transmission over an installed fibre link.

Combining the results of both sections in this chapter, we can conclude that the linear spectrogram *characterisation* method is a good candidate to become a versatile *monitoring tool*. Spectrograms deliver much more information than simple spectrum analyser traces, whilst adding only a minimal amount of equipment to the monitoring setup.

References

[1] E. Desurvire, "Optical communications in 2025," 31st European Conference on Optical Communication **1**, 5 – 6 (2005).

[2] G. Agrawal, *Nonlinear Fiber Optics* (Academic Press, 2001).

[3] E. Desurvire, O. Leclerc, and O. Audouin, "Synchronous in-line regeneration of wavelength-division multiplexed solitons signals in optical fibers," Optics Letters **21**, 1026 – 1028 (1996).

[4] O. Leclerc, E. Desurvire, and O. Audouin, "Synchronous WDM soliton regeneration: toward 80-160 Gbit/s transoceanic systems," Optical Fiber Technology: Materials, Devices and Systems **3**, 97 – 116 (1997).

[5] O. Leclerc, E. Desurvire, and O. Audouin, "Robustness of 80 Gbit/s (4×20 Gbit/s) regenerated WDM soliton transoceanic transmission to practical system implementation," Optical Fiber Technology: Materials, Devices and Systems **3**, 117 – 19 (1997).

[6] O. Leclerc, E. Desurvire, P. Brindel, and E. Maunand, "Synchronously modulated soliton systems: a simple analysis of timing-jitter statistics and bit

error rate," OFC '98. Optical Fiber Communication Conference and Exhibit. Technical Digest **2**, 290 – 1 (1998).

[7] G. Keiser, "A review of WDM technology and applications," Optical Fiber Technology: Materials, Devices and Systems **5**, 3 – 9 (1999).

[8] P. Hernday, "Measuring the group delay characteristics of narrow-band devices by the modulation phase shift method," Agilent Technologies Applications Engineering White Paper (2002).

[9] J. Veselka and S. Korotky, "Pulse generation for soliton systems using lithium niobate modulators," IEEE Journal of Selected Topics in Quantum Electronics **2**, 300 – 10 (1996).

[10] P. Winzer and C. Chandrasekhar, "SC4 - Modulation Formats and Receiver Concepts for Optical Transmission Systems," 31st European Conference on Optical Communication. ECOC 2005 **Short course notes** (2005).

[11] M. Forzati, A. Berntson, and J. Martensson, "IFWM suppression using APRZ with optimized phase-modulation parameters," IEEE Photonics Technology Letters **16**, 2368 – 70 (2004).

[12] M. Forzati, A. Berntson, J. Martensson, A. Djupsjobacka, J. Li, S. Melin, and H. Carlden, "40-Gb/s field transmission through 540 km SSMF using the APRZ modulation format," 2005 Optical Fiber Communications Conference Technical Digest **6** (2005).

[13] X. Wei, J. Leuthold, C. Dorrer, D. Gill, and X. Liu, "Chirp reduction of $\pi/2$ alternate-phase pulses by optical filtering," 2005 Optical Fiber Communications Conference Technical Digest **3** (2005).

[14] P. Winzer, C. Dorrer, R.-J. Essiambre, and I. Kang, "Chirped return-to-zero modulation by imbalanced pulse carver driving signals," IEEE Photonics Technology Letters **16**, 1379 – 81 (2004).

[15] E. Wooten, K. Kissa, A. Yi-Yan, E. Murphy, D. Lafaw, P. Hallemeier, D. Maack, D. Attanasio, D. Fritz, G. McBrien, and D. Bossi, "A review of lithium niobate modulators for fiber-optic communications systems," IEEE Journal of Selected Topics in Quantum Electronics **6**, 69 – 82 (2000).

[16] E. Zeek, Z. Wang, and R. Trebino, "Error bars in frequency-resolved-optical-gating measurements of ultrashort laser pulses," 15th Annual Meeting of the IEEE Lasers and Electro-Optics Society **2**, 590 – 1 (2002).

[17] M. Forzati, A. Berntson, J. Martensson, and R. Davies, "Performance analysis of single-MZM APRZ transmitter," 31st European Conference on Optical Communications, ECOC'05, Glasgow p. We4.P.081 (2005).

Chapter 6

Conclusions and thoughts for future directions

Throughout this thesis, the linear spectrogram method has been successfully applied to characterise a wide variety of optical waveforms. It was found that this method outperforms the commercial SHG-FROG apparatus in our lab, as shown in particular in Section 2.6. Even though more advanced FROG devices are already available, the linear spectrogram method offers a few unique advantages.
The fact that the method is not based on nonlinear effects makes it a much more sensitive technique, and has been proven to be very suitable to characterise for example the very long waveforms used in OCDMA experiments (Section 4.5). The easy practical implementation using readily available electro-absorption modulators also requires no sensitive alignment of free space optics. Furthermore, the flexibility of the self-referenced setup, using an optical delay stage followed by a photo-diode, is tremendous. Even though a much faster implementation is possible with an RF-phase shifter instead, it would not be suitable for example to characterise the 400 ps long OCDMA codes – assuming a 10 GHz, 360° RF phase shifter.
However, a faster implementation of this system, now limited by the speed of the translation stage and the data transfer rate from the OSA to the computer, would definitely be desirable. If one can acquire the spectrograms faster, the requirement on the stability of the waveform under test is reduced. This would certainly be a benefit in the case of the Pritel fibre ring laser, which often shows discrete phase instabilities every few seconds of operation. A real-time implementation would

furthermore be handy when tuning pulse shaping fibre Bragg gratings to the central wavelength of the input pulse, or optimising a pulse source such as the APRZ transmitter shown in Section 5.3.4.

Gain switching

The complete characterisation of the pulses generated by gain switching a semiconductor laser diode has led to a better understanding of the seeding process needed to reduce the timing jitter on the pulses. A fibre Bragg grating was designed to compensate the chirp of these pulses, and when accompanied with adequate spectral intensity filtering, it should be possible to make a compact, robust and stable pulse source. Measuring the final result obtained by these gratings would be exciting both from a gratings fabrication viewpoint, as well as a pulse characterisation viewpoint.

An investigation into self-seeding the 1060 nm laser diode with a narrow grating is already under way. This should lead to a reduction of the spectral intensity ripple previously noticed on the self-seeded pulses, as the behaviour of an external CW laser source as a seed is mimicked.

Modulators for gating

Even though electro-absorption modulators perform very well for the characterisation of the majority of the pulses examined in this thesis, their wavelength dependent characteristics limit their applicability, as shown in Sections 4.4.3 and 5.2.3. The collaboration with Alcatel-Thales, in which we were able to test some state-of-the-art EAMs has already delivered an EAM with a higher optical bandwidth. The trade-off between a wavelength dependency of the transfer characteristic and the steepness of it can be further exploited to achieve even higher bandwidth devices. Results in this thesis, showing that pulses as short as 1.3 ps are accurately characterised with a gating window of > 30 ps mean that it is not necessary to have a very steep transfer characteristic to measure ultrashort pulses.
Furthermore, close interaction between the fabrication and characterisation of the devices could lead to a great improvement in the chirp characteristics of the EAMs.

Fibre Bragg gratings

I believe this characterisation method can strongly impact the design and fabrication of fibre Bragg gratings for various purposes. First of all, the complete information gained from the measurements provides the ideal starting point to design gratings that will filter out particular pulse shapes. The accuracy of the fabricated grating can then also easily be tested by measuring the resulting pulse shaping.
The natural continuation of the work related to the OCDMA gratings, presented in Section 4.5 is to further extend the code length, to for example 64 chips. At least in the case where the chip duration is reduced accordingly (to 6.5 ps), the resolution of the OSA should be sufficient to deliver correctly sampled spectrograms. However, with a higher resolution spectrum analyser, such as the one used in the APEX complex spectrum analyser, the linear spectrogram method is easily scaled to suit waveform durations of the order of nanoseconds.
Work leading to a 16-chip temperature tunable OCDMA codes is already in an advanced stage. It will be very interesting to see how well the multiple phase shifts are defined in these gratings.

Higher capacity systems

As WDM systems with individual channel rates of 40 $Gbit/s$ are being brought to market, it will no doubt be interesting to see if the multi-channel line monitoring tool, investigated in Section 5.2, could be made commercially viable. Spectrographic measurements become easier as the repetition rate increases, because of the decreased demand on spectral resolution. The rapid rate at which advanced pulse modulation formats are gaining attention to further increase the capacity of transmission systems opens further interesting opportunities. Modulation formats such as DPSK, VSB and AMI can all to a certain extent be examined with this linear spectrogram method, for example with a fixed, repetitive 8-bit sequence. Numerical simulations where the merits of these respective modulation formats are under investigation, can now be backed up by experiments.

Appendix A

Bit error rates and Q-values

To determine the quality of performance of a certain optical link, it is common practice to measure the bit error rate (BER) as a function of the received optical power. Plotting these curves for example before and after insertion of a certain optical component, will give a figure for the *power penalty* of the respective component. Simply increasing the received power by this power penalty should then mitigate the effect of inserting the optical component concerned.
The power penalty, as calculated in this way, however, does not hold all the information about how the optical link is affected. It is easy to imagine for example a receiver setup that automatically compensates for a difference in optical received power through an optical amplifier. A power penalty has no relevance in this case. Moreover, with current high performance optical and electrical systems that operate virtually error-free, i.e. a BER of 10^{-12}, it takes a very long time to accumulate sufficient statistics to accurately estimate the operating margin. The Q-factor, on the other hand, is related to the best achievable BER, and gives a figure of merit for the quality of the optical transmission system:

$$BER = \frac{1}{2}\,\mathrm{erfc}\left(\frac{Q}{\sqrt{2}}\right) \tag{A.1}$$

The Q factor is defined as follows:

$$Q = \frac{|\mu_1 - \mu_0|}{\sigma_1 + \sigma_0} \tag{A.2}$$

where $\mu_{1,0}$ is the mean value of the marks/spaces rail of the eye diagram, and $\sigma_{1,0}$ is the standard deviation. A method to accurately estimate the Q-factor was first

introduced by Bergano *et al.* [1], and only recently standardised by the ITU-T (July 2003) [2]. What follows is an explanation of this Q-factor method, and how we implemented it practically.

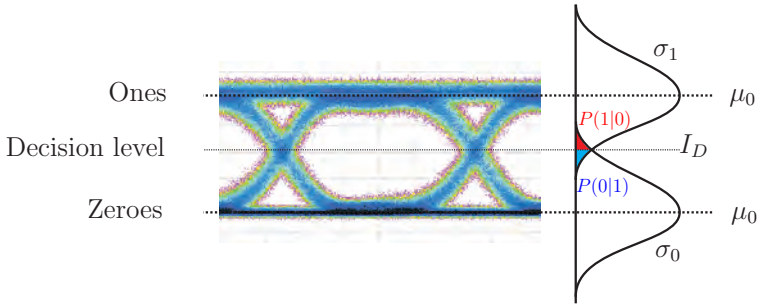

FIGURE A.1: The optimal decision threshold is determined by the crossover between the distribution of the ones and the zeroes.

An error occurs at the receiver side of the system when a sampled value of a "1" is less than the decision threshold I_D, or the sampled value of a "0" is more than the decision threshold. With a probability $P(0|1)$ of an incorrect decision when a "1" is received and $P(1|0)$ the probability of an incorrect decision when a "0" is received, the BER can be written as:

$$BER = p(1)P(0|1) + p(0)P(1|0). \tag{A.3}$$

Here, $p(0)$ and p(1) are the probabilities of receiving a "0" or a "1" respectively. When the occurrence of ones and zeroes is equally probable, we have $p(0) = 1/2 = p(1)$. Figure A.1 shows with the help of an eye diagram how the different parameters relate to each other. The best decision threshold level I_D is determined to be where the distribution of received ones crosses the distribution of received zeroes.

When these distributions are assumed to have Gaussian profiles, the BER is given by:

$$BER = \frac{1}{4}\left[\operatorname{erfc}\left(\frac{\mu_1 - I_D}{\sqrt{2}\sigma_1}\right) + \operatorname{erfc}\left(\frac{\mu_0 - I_D}{\sqrt{2}\sigma_0}\right)\right]. \tag{A.4}$$

When the decision level I_D is set close to the mean level of the ones, this equation reduces to

$$BER = \frac{1}{4}\operatorname{erfc}\left[\frac{\mu_1 - I_D}{\sqrt{2}\sigma_1}\right], \tag{A.5}$$

and analoguously for I_D for the decision level set close to the zeroes:

$$BER = \frac{1}{4}\operatorname{erfc}\left[\frac{\mu_0 - I_D}{\sqrt{2}\sigma_0}\right]. \tag{A.6}$$

We can measure the BER as a function of the decision threshold at a given received power, and then split the data up where the decision threshold delivers the minimum error rate. Each of these data sets can then be fitted to an ideal curve assuming Gaussian noise statistics [1]. We can then retrieve values for $\mu_{0,1}$ and $\sigma_{0,1}$ and determine the Q-factor, through equation A.2 .

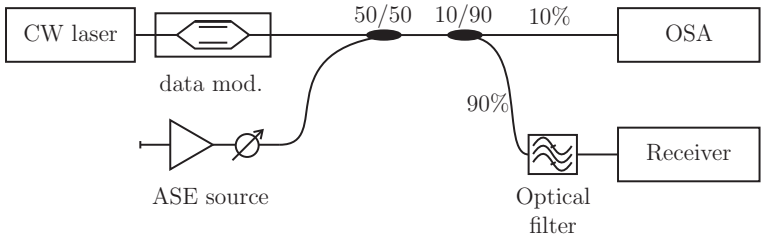

FIGURE A.2: Setup for comparing the Q-factor calculated from BER measurements and calculated from OSNR measurements. The ASE source consists of an EDFA followed by a variable attenuator.

Together with Mr. Taichi Kogure, I have implemented this method experimentally, by controlling the BER analyser through Labview and Matlab to scan the decision threshold level. To confirm that the Q-factors calculated by these measurements are accurate, the data was compared with Q-factors calculated from the optical signal to noise ratios (measured spectrally) and the extinction ratios (ER) between the ones and the zeroes (measured on a digital sampling oscilloscope).
The experimental setup is shown in Figure A.2. In order to be able to experimentally vary the signal to noise ratio, we coupled an ASE source followed by a variable optical attenuator together with the data signal. Here, the mean levels of the ones and the zeroes are obtained from:

$$\mu_0 = R.P_{in}.\frac{2ER}{1+ER} \tag{A.7}$$

$$\mu_1 = R.P_{in}.\frac{2}{1+ER} \tag{A.8}$$

where $R = \frac{\eta q}{h\nu} = \frac{\eta q \lambda}{hc}$ is the responsivity of the photodiode, with λ the wavelength of the light, c the speed of light, q the electronic charge constant, η the quantum efficiency of the photodiode and h Planck's constant.
The sigmas are calculated from the adapted noise current formulas from [3]:

$$\sigma^2 = \sigma_s^2 + \sigma_{sig-sp}^2 + \sigma_{sp-sp}^2 \tag{A.9}$$

The thermal noise is neglected, all noise terms are assumed uncorrelated, and the sum of a Poissonian distribution (shot noise) with two Gaussian distributions

is approximated here by a Gaussian distribution. σ_s^2 is the shot noise term and $\sigma_{sig-sp}^2 + \sigma_{sp-sp}^2$ the signal-spontaneous and spontaneous-spontaneous beat noise terms respectively. They are calculated as follows:

$$\sigma_s^2 = 2qRP_{in}\Delta f \tag{A.10}$$

$$\sigma_{1sig-sp}^2 = 4\frac{\mu_1 N_1}{\Delta\nu_{opt}}\Delta f \tag{A.11}$$

$$\sigma_{0sig-sp}^2 = 4\frac{\mu_0 N_0}{\Delta\nu_{opt}}\Delta f \tag{A.12}$$

$$\sigma_{1sp-sp}^2 = 4\frac{N_1 N_1}{\Delta\nu_{opt}}\Delta f \tag{A.13}$$

$$\sigma_{0sp-sp}^2 = 4\frac{N_0 N_0}{\Delta\nu_{opt}}\Delta f \tag{A.14}$$

$$\sigma_{ISI}^2 = \left(\frac{\mu_1-\mu_0}{Q_{max}}\right)^2 \tag{A.15}$$

with

$$N_1 = N_0 = S_{sp}.\Delta\nu_{opt}.R/2 \tag{A.16}$$

and

$$S_{sp} = \frac{10^{(P_{in}[dBm]-OSNR[dB])/10}}{\Delta\nu_{sp}}, \tag{A.17}$$

and where Q_{max} is the best Q factor measured in this system.

Table A.1 summarises the meaning of some of the symbols used, and their values. Figure A.3 shows very good agreement between the two different ways of calculating the Q-factor. Note that the Q-factor calculated from the OSNR is basically *fitted* to the data measured by varying the decision threshold. Here Q_{max}, used to determine the standard deviation of the noise due to the intersymbol interference σ_{ISI}, is chosen to be the best Q measured with the varying decision threshold method.

The method presented here for the qualitative assessment of components and transmission systems is very comprehensive. The practical implementation of the Q-factor measurement system delivers straightforward and unambiguous information, and has been validated experimentally by comparing it to the Q-factors calculated from OSNRs. Since the development of this measurement system, the work in my Ph.D. however has focussed more on complete waveform characterisation, and less on transmission system performance. Consequently, this Q-factor

Parameter	Symbol	Value	Unit
Bit rate		10	$Gbit/s$
Optical bandwidth for OSNR measurement	$\Delta\nu_{sp}$	0.1	nm
Optical bandwidth	$\Delta\nu_{opt}$	0.2	nm
Electrical bandwidth	Δf	8.5	GHz
Wavelength	λ	1550	nm
Extinction ratio	ER	12	dB
Rx input power	P_{in}	-10	dBm
Responsivity	R	1.25	A/W

TABLE A.1: Parameters for Q factor verification.

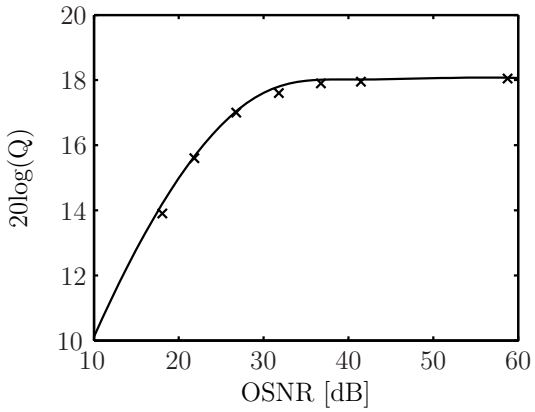

FIGURE A.3: Verification of the agreement between the Q-factor calculated from the OSNR level (line) and the measured Q-factors (×) in a 10 $Gbit/s$ NRZ system as a function of the measured OSNR.

measurement system has not been used extensively in this thesis, but it remains a powerful tool in the lab that can be used by future students and researchers.

References

[1] N. S. Bergano, F. Kerfoot, and C. Davidson, "Margin measurements in optical amplifier systems," IEEE Photonics Technology Letters **5**, 304 – 306 (1993).

[2] ITU-T, "Fibre optic communication subsystem test procedures - Digital systems - Part 2-8: Determination of low BER using Q-factor measurements," O.201 IEC 61280-2-8 (2003).

[3] G. Agrawal, *Fiber-Optic Communication Systems* (Wiley and Sons, 2002).

Appendix B

Preprocessing and deconvolution Matlab code

This appendix contains the relevant bits of code for the spectrogram deconvolution software that I have written in Matlab. The full code creates a graphical user interface, and it is clear that it contains many more lines of code. Only particularly interesting parts of the code associated with data manipulation and processing are shown below for clarity. A fully integrated and user friendly version of this software has been left in the laboratory for subsequent students and researchers.

B.1 Preprocessing

B.1.1 Noise subtraction

```
%%% Noise subtraction

% Load spectrogram data
    h=handles.axes1;
    F=get(h,'userdata');
% Read threshold value
    threshold=eval(get(handles.edit6,'String'));
% Subtract threshold level
    FROG_Thr=F.FROG_Expt-threshold;
% Reset negative values to 0
    FROG_Thr(find(FROG_Thr<0))=zeros(size(find(FROG_Thr<0)));
% Renormalise spectrogram
    FROG_Thr=FROG_Thr./max(max(FROG_Thr));
% Save and plot result in Matlab figure
```

```
    axes(handles.axes2);
    pcolor(TT,F.WW_Expt,log10(FROG)), shading flat;
    set(handles.axes2,'Tag','axes2');
    set(handles.axes2,'userdata',struct('TT_Expt',F.TT_Expt,...
        'WW_Expt',F.WW_Expt,'FROG_Thr',FROG_Thr));
% Go to next step
    bSpectralAverage_Callback(hObject, eventdata, handles);
```

B.1.2 Spectral filtering or envelope detection

```
%%% Spectral filtering or envelope detection

% Load spectrogram data
    h=handles.axes2;
    F=get(h,'userdata');
% Choose between envelope detection (cbWindow is checked),
% or spectral averaging (cbWindow is not checked).
    if get(handles.cbWindow,'Value')==1,
      Nw_Expt=size(F.FROG_Thr);
      Nw_Expt=Nw_Expt(1);
      % read number of pixels to search for the maximum measured value:
      peakwindowsize=eval(get(handles.edit7,'String'));
      % perform envelope detection
      for k=peakwindowsize+1:Nw_Expt
        FrogSum(k,:) = max(F.FROG_Thr(k-peakwindowsize:k,:));
      end
    else
      FrogSum=zeros(size(F.FROG_Thr));
      % read number of pixels to average (x2):
      averages=abs(eval(get(handles.edit7,'String')))
      % perform averaging
      for counter=-averages:averages
        FrogSum=FrogSum+circshift(F.FROG_Thr,counter);
      end;

    end
    F.FROG_Thr=FrogSum;
    F.FROG_Thr=F.FROG_Thr./max(max(F.FROG_Thr));

% Plot and save
    axes(handles.axes3);
    pcolor(F.TT_Expt,F.WW_Expt,F.FROG_Thr), shading flat;
    set(handles.axes3,'Tag','axes3');
    set(handles.axes3,'userdata',struct('TT_Expt',F.TT_Expt,...
        'WW_Expt',F.WW_Expt,'FROG_Thr',F.FROG_Thr));
% Go to next step
    bFrequency_Callback(hObject, eventdata, handles);
```

B.1.3 Resampling on spectral lines

```
%%% Resampling on spectral lines
```

```
% Load spectrogram data
    h=handles.axes3;
    F=get(h,'userdata');
% Read central frequency
    CF=eval(get(handles.eCentralFrequency,'String'));
% Read repetition rate
    RepetitionRate=eval(get(handles.eRepetitionRate,'String'));
% Read number of spectral lines to consider (each side of the central freq)
    ncomp=eval(get(handles.encomp,'String'));
% Construct new grid
    FrequencyGrid=(CF-(ncomp-1)*RepetitionRate:RepetitionRate:...
        CF+(ncomp)*RepetitionRate);
    Nw_Expt=length(FrequencyGrid);

% Resample information on the new frequency grid
    Ax=interp2(F.TT_Expt,F.WW_Expt',F.FROG_Thr,F.TT_Expt,FrequencyGrid',...
    Ax(find(Ax<0))=zeros(size(find(Ax<0)));
    Ax(find(isnan(Ax)))=zeros(size(find(isnan(Ax))));
    Ax=Ax./max(max(Ax));
% Save and plot results
    axes(handles.axes4);
    pcolor(F.TT_Expt,FrequencyGrid,log10(Ax)), shading flat;
    set(handles.axes4,'Tag','axes4');
    set(handles.axes4,'userdata',struct('TT_Expt',F.TT_Expt,...
        'WW_Expt',FrequencyGrid,'FROG',Ax));
% Go to next step
    bFourierGrid_Callback(hObject, eventdata, handles);
```

B.1.4 Interpolation onto Fourier grid

```
%%% Interpolation onto Fourier grid

% Load spectrogram data
    h=handles.axes4;
    F=get(h,'userdata');
% Read repetition rate and central frequency
    RepetitionRate=eval(get(handles.eRepetitionRate,'String'));
    CF=eval(get(handles.eCentralFrequency,'String'));
    dF=RepetitionRate;
% Determine temporal span of the spectrogram
    Tspan=1/RepetitionRate;
% Determine grid size
    Fspan=eval(get(handles.eFwidth,'String'));
    N=2*(2^ceil(log(Fspan/dF)/log(2)));
    Nt=N;
% Determine temporal resolution
    dT=Tspan/Nt;
    Nf=N;
% Construct axes
    TT = [-Nt/2:(Nt/2)-1]*dT;              % ps
    FF = [-Nf/2:(Nf/2)-1]*dF;              % THz
```

```
% Interpolate onto the new grid
    FROG_Int=interp2(F.TT_Expt,F.WW_Expt'-CF,F.FROG,TT,FF','linear');
    FROG_Int(find(isnan(FROG_Int)))=zeros(size(find(isnan(FROG_Int))));
    FROG_Int(find((FROG_Int<0)))=zeros(size(find((FROG_Int<0))));

% Plot and save results
    axes(handles.axes5);
    pcolor(TT,FF,log10(FROG_Int)), shading flat;
    caxis manual;
    cax=caxis
    set(handles.axes5,'Tag','axes5');
    set(handles.axes5,'userdata',struct('TT',TT,'FF',FF,'FROG',FROG_Int));
```

B.1.5 2D filtering in Fourier domain

```
%%% 2D filtering in Fourier domain

% Supergaussian filter order:
    order=3;
% Read filter width values
    eXXs=eval(get(handles.eXX,'String'));
    eYYs=eval(get(handles.eYY,'String'));
    dX=eXXs*(Nt)/2/(2*log(2).^(1/(2*order)));
    dY=eYYs*(Nf)/2/(2*log(2).^(1/(2*order)));
% Calculate 2D (super)Gaussian function
    [XX YY]=meshgrid([-Nt/2:Nt/2-1],[-Nf/2:Nf/2-1]);
    % either 2D-Gaussian, or a more square function
    if get(handles.cbSquareFilter,'Value')==1,
         Filter=exp(-((((XX-0.5)./dX).^2).^order+((YY./dY).^2).^order));
    else Filter=exp(-(((XX-0.5)./dX).^2+(YY./dY).^2).^order);
    end
% Calculate Fourier transform of spectrogram
    FROG_FF=fftshift(fft2(fftshift(FROG_Int)));
% Plot Fourier transform of spectrogram and 3dB line of filter function
    axes(handles.axes6);
    pcolor(log10(abs(FROG_FF))),shading flat;
    set(handles.axes6,'Tag','axes6');
    hold on
    FROG_FF=FROG_FF.*Filter;
    FROG_Int=abs(fftshift(ifft2(fftshift(FROG_FF))));
    contour(Filter,[0.5,0.5],'w');
    set(handles.axes6,'Tag','axes6');
    set(handles.axes6,'userdata',struct('TT',TT,'FF',FF,'FROG',FROG_Int));
    hold off

% Threshold spectrogram again to remove any new filtering artifacts
    threshold=eval(get(handles.edit6,'String'));
    FROG_Int=FROG_Int-threshold/4;
    FROG_Int(find(FROG_Int<0))=zeros(size(find(FROG_Int<0)));
% Renormalise data
    FROG_Int=FROG_Int./max(max(FROG_Int));
```

```
% Plot and save
    axes(handles.axes7);
    pcolor(TT,FF,log10(FROG_Int)), shading flat;
    caxis manual;
    caxis(cax);
    set(handles.axes7,'Tag','axes7');
    set(handles.axes7,'userdata',struct('TT',TT,'FF',FF,'FROG',FROG_Int));
```

B.2 Principle components generalised projections algorithm

```
%%% PCGP algorithm

% ...

% Define relationship between O.P. matrix and T.D matrix
    RI=reshape([1:Nt^2],Nt,Nt);
    for row=1:Nt,
        % Rearrange rows into columns of constant delay
        RIrr(row,[1:Nt-(row-1)])=RI(row,[row:Nt]);
        RIrr(row,[Nt-(row-2):Nt])=RI(row,[1:row-1]);
    end
    % Rearrange columns into order of increasing delay
    RIcr(:,[1:Nt/2])=RIrr(:,[Nt/2:-1:1]);
    RIcr(:,[Nt/2+1:Nt])=RIrr(:,[Nt:-1:Nt/2+1]);

% Initial gate (either load a saved gate, or calculate a gaussian profile
    if get(handles.cbLoadGate,'Value')==1,
         load(get(handles.eLoadGt,'String'),'GtRe','-mat');
    G=GtRe;
    else
         TfwhmG=eval(get(handles.eStartGate,'String'));
         Cg=eval(get(handles.eStartGateChirp,'String'));
         Tog=TfwhmG/(2*log(2).^0.5);
         G=exp(-(1+i*Cg)/2 .*(F.TT./Tog).^2);
    end
    Gt=G;

% Initial Pulse (Gaussian profile, with given duration and chirp)
    TfwhmE=eval(get(handles.eStartPulse,'String'));
    Ce=eval(get(handles.eStartPulseChirp,'String'));
    Toe=TfwhmE/(2*log(2).^0.5);
    E=exp(-(1+i*Ce)/2 .*(F.TT./Toe).^2);
    Et=E;

% Initialisation of variables
    n=0;
    Ni=eval(get(handles.eMaxIterations,'String'));
    alpha1=eval(get(handles.eAlpha,'String')); % (overcorrection alpha)
```

```
tec=0;
minerror=inf;
SHG=get(handles.cbSHGFROG,'Value'); % SHG FROG spectrogram or not?
warning off;
while get(handles.bStop,'Value')==0 & n<Ni,
    n=n+1;
    % Construct outer product
    if SHG==1,   % for SHG, use symmetric algorithm
        OP1=Et.'*Gt;
        OP2=Gt.'*Et;
        OP=OP1+OP2;
    else OP=Et.'*Gt;
    end;
    % Row rotate to order matrix into columns of constant delay
    rrOP(RI)=OP(RIcr);
    % Reshape to obtain E(t,tau)
    Ft=reshape(rrOP,Nt,Nt);
    % Fourier transform E(t,tau) to obtain E(omega,tau)
    Ff=ifftshift(fft(fftshift(Ft)));
    % Apply intensity constraint (with overcorrection alpha1)
    FfCon=Ff.*abs(sqrt(F.FROG)./Ff).^alpha1; %sqrt na abs
    FfCon(find(isnan(FfCon)))=sqrt(F.FROG(find(isnan(FfCon))));
    % Inverse Fourier transform E(w,tau) to obtain E(t,tau)
    FtCon=fftshift(ifft(fftshift(FfCon)));
    % Row rotate to order matrix into columns of constant delay
    crOP(RIcr)=FtCon(RI);
    OP=reshape(crOP,Nt,Nt);
    % Calculate new guess for Et
    Et=OP'*Et';
    Et=(OP*Et).';
    % Apply spectral constraint to Et (from independent spectral measurement)
    if get(handles.cbUseFspecConstraint,'Value')==1,
        if n < eval(get(handles.eFspec,'String')),
            Ef=fftshift(fft(fftshift(Et)));
            Ef=sqrt(Fund_Spectrum).*(Ef./abs(Ef));
            Ef(find(isnan(Ef)))=sqrt(Fund_Spectrum(find(isnan(Ef))));
            Et=fftshift(ifft(fftshift(Ef)));
        end
    end
    Et=Et/max(abs(Et));

    % Calculate new guess for Gt, after an initial number of iterations
    % where the gate was fixed.
    if n>eval(get(handles.eHoldGate,'String')),
        Gt=OP*Gt';
        Gt=(OP'*Gt)';
        Gt=Gt/max(abs(Gt));
    end

    % Calculate spectrogram error
    [errorx alphaerror]=fminsearch('errorfunction',1,[],F.FROG,abs(Ff).^2,Nt);
    error(n)=alphaerror;
    % possibly adjust the overcorrection factor slightly with every
    % iteration
    alpha1=alpha1;
```

```
    % Save best deconvolution result
    if error(n) < minerror,
        minerror=error(n);
        EtRe=Et;
        GtRe=Gt;
        FfRe=Ff;
    end

    % Spectrally filter the gate repetitively (to prevent local minima)
    if get(handles.cbGfilter,'Value')==1,
        if mod(n,eval(get(handles.eGfilter,'String')))==0,
            order=eval(get(handles.eOrder,'String'));
            Gf=ifftshift(fft(fftshift(Et)));
            XXg=[round(-length(Gf)/2):1:round(length(Gf)/2)-1];
            dXg=0.5*eval(get(handles.eWidth,'String'))*...
                Nt/2/(2*log(2).^(1/(2*order)));
            Filtergate=exp(-((XXg./dXg).^2).^2);
            Gf=Gf.*Filtergate;
            Et=fftshift(ifft(ifftshift(Gf)));
            order=eval(get(handles.eOrder,'String'));
            Gf=ifftshift(fft(fftshift(Gt)));
            XXg=[round(-length(Gf)/2):1:round(length(Gf)/2)-1];
            dXg=eval(get(handles.eWidth,'String'))*Nt/2/(2*log(2).^(1/(2*order)));
            Filtergate=exp(-((XXg./dXg).^2).^2);
            Gf=Gf.*Filtergate;
            Gt=fftshift(ifft(ifftshift(Gf)));
        end
    end

    % Renew plots results every 'eUpdate' iterations
    if mod(n,eval(get(handles.eUpdate,'String')))==0
        ...
        ...
        ...
    % Stop algorithm when a very good match has been found
    if get(handles.bStop,'Value')==1 | minerror < 1e-12
        stop = 1;

    end
end
```

Appendix C

Time Division Multiplexing

The shorter the pulses, the higher the bit rates that can be achieved using these pulses. Electronic systems are currently limited to around 85 $Gbit/s$ (largely by the transit times of the carriers in the semiconductor junctions that make up the transistors etc.) When working at very high frequencies, optical methods have to be investigated to get to higher bit rates, for transmission as well as for reception of the signals.

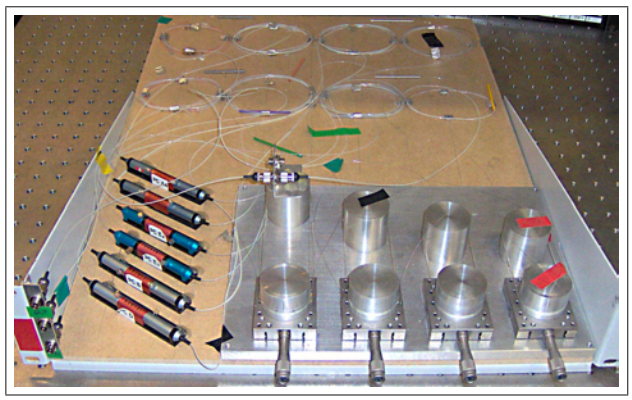

FIGURE C.1: Photo of the 4 stage interleaver, implemented with standard single mode fibre and polarisation controllers in each arm.

Here, passive multiplexing is used to produce higher bit rates. The pulse stream can be split into two replicas using a 50/50 coupler. One of these can be delayed by half a bit period (or a an uneven multiple of this) with respect to the other replica, before it is combined again in a second coupler with the other replica. Hence the repetition rate of the pulse stream is doubled. This process can be repeated as many times as the pulse length permits, bearing in mind that the bit period and the pulse energy halve each time [1]. Starting for example with a pulse

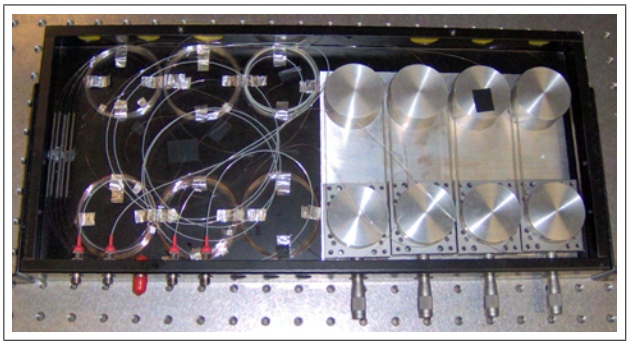

FIGURE C.2: Photo of the 4 stage interleaver, implemented with polarisation maintaining fibres and couplers.

that has a FWHM duration of 5 ps at 10 $Gbit/s$, the pulses can be multiplexed up to 80 $Gbit/s$, where the bit period is 12.5 ps.

I have constructed two time division multiplexers, using the same principle, see Figures C.1 and C.2. To set the delay to be exactly an uneven multiple of the half the bit period, the fibres are stretched mechanically. To make sure the pulses are uncorrelated, the length of fibre in one arm, and hence the propagation time, must be significantly longer than one pulse period.

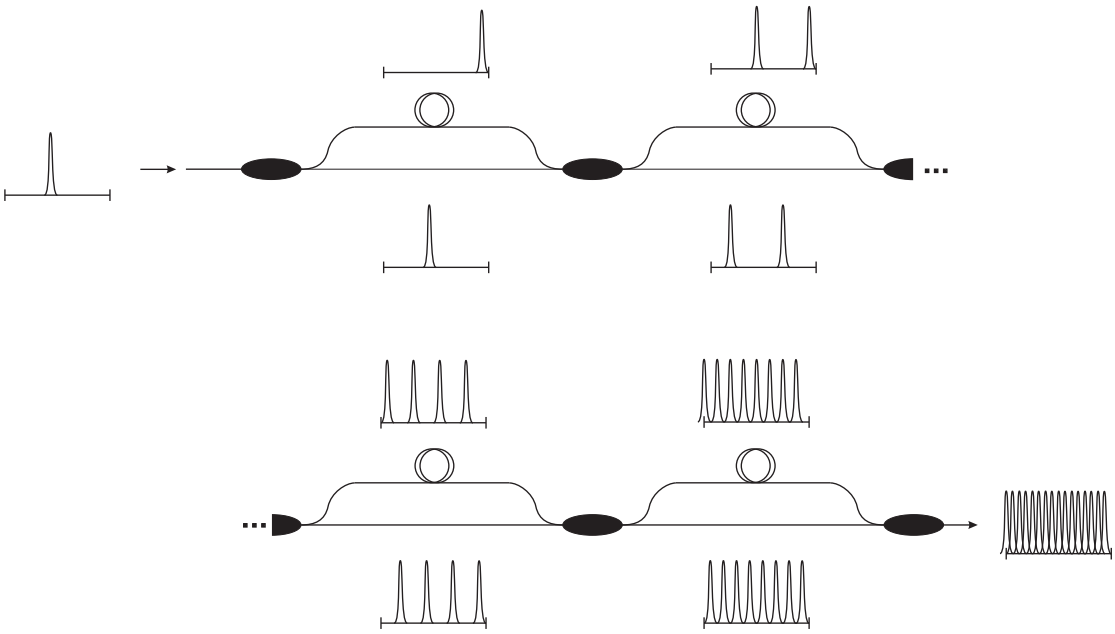

FIGURE C.3: Scheme of the optical time division multiplexer.

Sometimes it is necessary to ensure that all the pulses are in the same polarisation state after they are recombined at each coupler stage. This is achieved by including polarisation controllers in each arm.

The polarisation can also be used to an advantage, when a polariser is placed just after the multiplexer. Adjusting the polarisations in the arms makes it possible to balance the powers of the different pulse streams when they are multiplexed. In practice however, this proves to be very difficult, as the system has twelve degrees of freedom for a multiplexer with just three stages.

To avoid this, another multiplexer was then constructed, using just polarisation maintaining (PM) fibre and couplers. The power levels of the arms were balanced during the construction of the multiplexer. The polarisation maintaining fibre ensures that all the multiplexed pulses remain on the same polarisation. This multiplexer has been upgraded with another stage and is now used to multiplex 2 ps long pulses at a repetition rate of 10 GHz up to 160 $Gbit/s$ signals, while the other interleaver is used for experiments at lower bit rates.

References

[1] A. Takada and M. Saruwatari, "100 Gbit/s optical signal generation by time-division multiplication of modulated and compressed pulses from gain-switched distributed feedback (DFB) laser diode," Electronics Letters **24**, 1406 – 8 (1988).

List of Publications

- B.C. Thomsen, Y. Jeong, C. Codemard, M.A.F. Roelens, P. Dupriez, J.K. Sahu, J. Nilsson and D.J. Richardson, "60W 10GHz 4.5ps pulse source at 1.5 microns", CLEO/IQEC 2004, San Francisco 16-21 May 2004, paper CMAA.

- M.A.F. Roelens, B.C. Thomsen and D.J. Richardson, "High quality 5ps pulse generation at 10 Gbit/s using a fibre Bragg grating compensated gain-switched laser diode", OECC 2004, Yokohama 12-16 Jul 2004, Paper 16D1-4.

- M.A.F. Roelens, B.C. Thomsen and D.J. Richardson, "Multi-wavelength EAM based optical sampling for performance monitoring in high bit-rate systems", ECOC 2004, Stockholm 5-9 Sep 2004, paper We4.P116.

- J. Prawiharjo, K. Gallo, B.C. Thomsen, M.A.F. Roelens, P.J. Almeida, N.G.R. Broderick and D.J. Richardson, "Blind-FROG in a quasi-phase-matched LiNbO3 waveguide", OFC 2005, Anaheim 6-11 Mar 2005.

- J. Prawiharjo, K. Gallo, B.C. Thomsen, M.A.F. Roelens, P.J. Almeida and N.G.R. Broderick, "Frequency resolved optical gating in a quasi-phase-matched LiNbO3 waveguide", IEEE Photonics Technology Letters **17**, pp.849-51 (2005).

- J.H.V. Price, A. Malinowski, A. Piper, F. He, W. Belardi, T.M. Monro, M. Ibsen, B.C. Thomsen, Y. Jeong, C. Codemard, M.A.F. Roelens, P. Dupriez, J.K. Sahu, J. Nilsson and D.J. Richardson, "Advances in high power short pulse fiber laser systems and technology", Photonics West 2005, San Jose 22-27 Jan 2005 5709-30 (Invited).

- C. Tian, Z. Zhang, M.A.F. Roelens, P. Petropoulos, M. Ibsen and D.J. Richardson, "Full characterisation of the temporal response of phase-shifted SSFBGs using electroabsorption modulator based frequency resolved optical gating", BGPP/ACOFT 2005, Sydney 4-9 Jul 2005.

- M.A.F. Roelens, C. Tian, Z. Zhang, P. Petropoulos, M. Ibsen and D.J. Richardson, "Full characterisation of the temporal response of complex phase shifted Bragg gratings for OCDMA using frequency resolved optical gating", ECOC 2005, Glasgow 25-29 Sep 2005.

- M.A.F. Roelens, M. Forzati, A. Djupsjöbacka, P. Petropoulos, A. Berntson and D.J. Richardson, "High quality pulse and device characterisation using EAM-based frequency resolved optical gating", ECOC 2005, Glasgow 25-29 Sep 2005.

- Z. Zhang, C. Tian, M.A.F. Roelens, M.R. Mokhtar, P. Petropoulos, D.J. Richardson and M. Ibsen, "Direct accurate determination of the spatial refractive index profile in Bragg gratings", BGPP/ACOFT 2005, Sydney 4-8 Jul 2005.

- P. Petropoulos, C. Tian, Z. Zhang, M. Ibsen, M.A.F. Roelens, P.C. Teh and D.J. Richardson, "Applications of superstructured fibre Bragg gratings in OCDMA systems", NOC 2005, London 5-7 Jul 2005 (Invited).

- F. Parmigiani, P. Petropoulos, M. Ibsen, M.A.F. Roelens and D.J. Richardson, "A novel XPM based pulse retiming system incorporating a fibre grating based parabolic pulse shaper", ECOC 2005, Glasgow 25-29 Sep 2005.

- D.J. Richardson, P.C. Teh, M.A.F. Roelens, B.C. Thomsen, C. Tian, Z. Zhang, P. Petropoulos and M. Ibsen, "Direct sequence OCDMA systems based on fibre grating technology", ECOC 2005, Glasgow 25-29 Sep 2005 (Invited).

- C. Tian, M.A.F. Roelens, M. Ibsen, P. Petropoulos and D.J. Richardson, "Reconfigurable al-optical header recognition for packet switched networks", e-Photon/One Summer School, Pisa and Cesenatico, Aug/Sep 2005.

- B.C. Thomsen, M.A.F. Roelens, R.T. Watts and D.J. Richardson, "Comparison between nonlinear and linear spectrographic techniques for the complete characterization of high bit-rate pulses in optical communications", IEEE Photonics Technology Letters **17**, pp. 1914-16 (2005).

- M.A.F. Roelens, M. Forzati, A. Djupsjöbacka, P. Petropoulos, A. Berntson and D.J. Richardson, "Linear Frequency Resolved Optical Gating as a Line Monitoring Tool", OFC 2006, Anaheim 5-10 Mar 2006.

- M.A.F. Roelens, M. Forzati, P. Petropoulos, A. Berntson, A. Djupsjöbacka and D.J. Richardson, "Phase and intensity characterisation of transmitted pulses", Northern Optics 2006, Bergen (Norway), 14-16 June 2006.

- F. Parmigiani, C. Finot, K. Mukasa, M. Ibsen, M.A.F. Roelens, P. Petropoulos and D.J. Richardson, "Ultra-flat SPM-Broadened Spectra in a Highly Nonlinear Fiber Using a Fiber Bragg Grating Based Parabolic Pulse Shaper", ECOC 2006, Cannes (accepted).